Insight into the Local Solvent Environment of Biologically Relevant Iron-nitroysl Systems through Two-Dimensional Infrared Spectroscopy

Jennifer Faith Brookes

A dissertation

submitted in partial fulfillment of the

requirements for the degree of

Doctor of Philosophy

University of Washington

2015

Reading Committee:

Munira Khalil, Chair

Matthew F. Bush

Philip J. Reid

Program Authorized to Offer Degree:

Chemistry

University of Washington

Abstract

Understanding the Local Solvent Environment of Biologically Relevant Iron-Nitrosyl Systems through Two-Dimensional Infrared Spectroscopy

Jennifer Faith Brookes

Chair of the Supervisory Committee:
Associate Professor Munira Khalil
Department of Chemistry

Iron-nitrosyl systems, particularly in the form of heme proteins, with their iron metal active sites play an important role in biological systems. Heme proteins act as storage, transporters, and receptors for nitric oxide (NO), a signaling molecule that is important in immune, nervous, and cardiovascular systems of mammals. By better understanding the local environment of the active site of NO binding heme proteins we can gain insight into disease in which the NO pathways have been implicated. This is an important step to being able to develop pharmaceuticals targeting NO pathways in humans.

Sodium nitroprusside ((SNP, $Na_2[Fe(CN)_5NO]\cdot 2H_2O$) is investigated as a model system for the active site of nitric oxide binding heme proteins. Using two-dimensional infrared spectroscopy (2D IR) to obtain dephasing dynamics of the nitrosyl stretch (ν_{NO}) in a series of solvents we are able to better understand the local environment of the more complicated

metalloproteins. Rigorous line shape analysis is performed by using nonlinear response theory to simulate 2D IR spectra which are then fit to experimental data in an iterative process to extract frequency-frequency correlation functions (FFCFs). The time scales obtained are then correlated to empirical solvent polarity parameters. The analysis of the 2D IR lineshapes reveal that the spectral diffusion timescale of the ν_{NO} in SNP varies from 0.8 – 4 ps and is negatively correlated with the empirical solvent polarity scales.

We continue to investigate NO binding of metalloproteins through 2D IR experiments on nitrophorin 4 (NP4). NP4 is a pH-sensitive NO transporter protein present in the salivary gland of the blood sucking insect *Rhodius prolixus* which undergoes a pH sensitive structural change between a closed and open conformation allowing for the storage and delivery of NO. The two structures are observed spectroscopically as two distinct pH-dependent ν_{NO} frequencies at ~1904 and ~1917 cm^{-1}. We obtain FFCFs by globally fitting experimental 2D IR spectra to signals calculated using a third-order nonlinear response formalism. The open conformation has frequency-frequency correlation timescales of ~1 ps and ~100 ps under both acidic and basic conditions. The closed conformer has pH dependence with fast time scales of 3.0 ps (pH 5.1) and 1.4 ps (pH 7.9) with a static component present under both conditions. The dephasing dynamics of NP4 can be correlated to the local solvent environment within the distal pocket providing quantitative confirmation to the presence and absence of water molecules in two conformers under both pH conditions.

Table of Contents

List of Figures

List of Tables

ACKNOWLEDGEMENTS

This dissertation marks the end of 23 years of formal education during which I have had the opportunity to work with wonderful teachers, coaches, mentors, colleagues, and collaborators. The work presented within is the result of the last 6 years of that journey. I am so very thankful to all of those who have helped shape the path leading to this Ph.D. and those who have supported me along the journey.

My colleagues at the University of Washington have helped me though the graduate school experience and to grow both as a scientist and a person throughout my time here. They all deserve the most heartfelt of thanks. Sam Marionni, a faithful coffee companion, I am especially thankful to him for always providing much needed insight into life and science. Sam Connelly who spent many evenings with me entirely devoid of science, I am so thankful for her kind support and empathy throughout the last six years. Tom Porter, who was my first friend at UW, has been a constant reminder that laughter really is the best medicine. He has made my time here a much richer experience. Glennis Rayermann and Joseph May were the very best study partners I could have asked for, they made me feel at home in a city where I did not know anyone and have provided unwavering encouragement. My labmates Karla Slenkamp and Anthony Reynolds have become as close to siblings as I have found outside my immediate family. We have shared so many struggles and successes, as well as tears and bursts of laughter over the last 6 years that there are no words grand enough to fully express my gratitude. The conversations both serious and lighthearted late into the night with Madhu Balasubramanian helped to make the last couple years at UW bearable. I was so fortunate to be able to work with her. Madhu's strength and sincerity is an inspiration to us all. Thank you to my advisor Munira, who let me wander very far

outside the world of science this year when I needed it the most. To the rest of my lab, thank you for the laughter, the food, and the science over these past six years.

I would be remiss if I did not also thank the University of Portland Department of Chemistry faculty, staff, and students who have continued to provide perspective and encouragement to me long after leaving the third floor of Swindells. The education I received there helped me to know whole heartedly that my struggles and successes are never my own. They are those of the classmates outside the door full of high-fives and hugs after a particularly brutal exam. They are those of my professors who provided so much more than just knowledge of science. The mentorship I have received and continue to receive from my professors at UP has been vital to finishing this degree.

I would like to thank my father Kevin as well as my brothers Chris and Matt. Matt convinced me to major in chemistry so I am quite serious when I say that this Ph.D. is entirely his fault. I am from a very large extended family full of very strong women who have been a source of great inspiration to me. Especially as I have grown older, I am constantly amazed by their strength and love. I have been fortunate enough to have had three wonderful grandmothers: Patsy Highland, Mary Gilbert, and Peggy Klein. While not all of them have made it to see this day it is their encouragement and support which got me here and they deserve recognition. My Aunt Lauri also deserves a huge thank you. I was lucky enough to always have her in my life as a second mother and without her perspective and faith in me I certainly would not be where I am today. Adam Rimshaw, who has been the light at the end of a very long tunnel, deserves so much more than just a thank you. I am so grateful to have had him on my team the last several years.

My work here and everywhere, is and will always be dedicated to my mother, Peggy. She raised me to believe that I could do anything I dreamed up. She fought for my education every

step of the way so that belief could be a reality. Her grace, strength, and impressive ability to cook will continue to be the standard I strive to. She gave me the freedom to try anything and make my own decisions even when my decisions were not what she had in mind for me. My mother taught me to be the strong women I am today and I am so thankful for every moment I had her in my life. She is no longer here to read this acknowledgement, but everyone should know that none of the work I accomplished at the University of Washington or anywhere else would have been possible without her. I really did have the most wonderful mother.

DEDICATION

In memory of my mom, Peggy

CHAPTER 1

INTRODUCTION

1.1 Introduction

The chemistry of life is inherently solution phase chemistry and the solvent is water. The presence, properties, and arrangement of water molecules in both the intra- and extracellular matrix of living organisms play an important role in cellular reactions. In addition to water other molecules within the system can interact with enzymes affecting the overall function of a protein, often times this is the mode of action for pharmaceuticals. By understanding how the local environment affects protein function we can improve our understanding of what goes right and wrong in biological pathways resulting in disease.

At the heart of the work presented in this dissertation is the basic question: what can we learn about the environment of molecules by how they interact with light? The characteristics of electromagnetic radiation absorbed, scattered, and emitted from molecules allows us study basic properties of matter. Spectroscopy is one of the most powerful tools we have to study complex molecules as it is both sensitive and specific. We use time-dependent infrared spectroscopies that probe the interaction of light with the molecular vibrations of molecules in order to understand the solvent environment of biologically relevant iron-nitrosyl systems.

1.2 Nitric Oxide and Iron Systems

Nitric oxide (NO) plays an essential role in biological systems as a signaling molecule which has been implicated in a wide range of pathways in the immune, nervous, and cardiovascular systems. Iron-nitrosyl proteins play the central role in storage, transportation, and

sensing of NO within living systems.[1] The protein soluble guanylyl cyclase (sGC) is the major intracellular target of NO in eukaryotes, playing an important physiological role regulating many processes including vasodilation and neurotransmission. The binding of NO to the heme in sGC begins the signaling cascade which synthesizes of the second messenger cyclic GMP (cGMP) from quanosine-5'-triphosphate (GTP). The significance of the NO-cGMP signaling pathway in diseases such as hypertension, congestive heart failure, and chronic renal disease make it an important and active area of research in the health sciences.[1] The sGC protein is part of the larger H-NOX (heme nitric oxide/oxygen binding) protein family. H-NOX proteins include important heme sensing proteins that have been isolated from both prokaryotes and eukaryotes.

In order to build the toolset we need to fully utilize the correlation of ultrafast dynamics to the local environment in complex heme protein systems such as sGC we begin with a model iron-nitrosyl system: sodium nitroprusside (SNP). The molecular structure of SNP is shown in

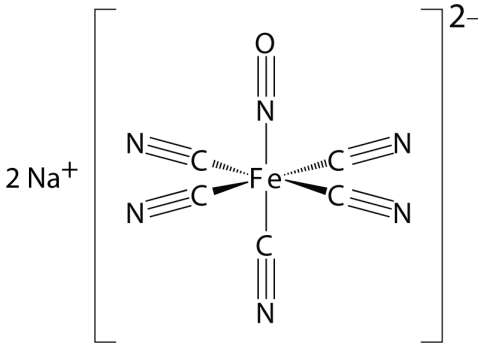

Figure 1.1 Molecular structure of sodium nitroprusside

Figure 1.1. SNP is an excellent model system for the study of iron-nitrosyl systems because it contains only one NO ligand and has a six coordinate structure. Both our group and others have extensively studied SNP.[2-5] Further work presented in this thesis has looked in depth into the protein nitrophorin 4 (NP4), which is used as a NO storage and transport protein in the salivary gland of the blood sucking insect *Rhodnius prolixus***.** NP4 is a pH-sensitive heme protein which

undergoes a large conformational change from the insect saliva pH of ~5 to the human blood pH of ~7. As a result the protein tightly binds the highly reactive NO molecule when in the salivary gland, where it would it could cause oxidative damage, but while sucking the prey's blood, the increase in pH induces a structural rearrangement of the protein that allows NO release. The release of NO causes vasodilation allowing the insect to have a more readily available meal.

The advantage of an infrared technique in studying the active site of proteins comes from the specificity of the experiment and the measurable timescales. Ultrafast experiments in the mid-IR are able to measure structural changes in molecules happening on the picosecond to femtosecond timescales. Infrared probes are also sensitive to the local environment and can be selected and probed independently of other molecular processes. In the case of Fe-NO systems, you can directly measure the NO stretching mode which allows for monitoring of the system without the addition of chromophores. In Fe-NO systems we can specifically excite the NO stretching frequency and then watch the evolution of the vibration over the time scale of solvent reorganization and larger structural reorganization. Heme proteins have been extensively studied by probing the Fe-NO motif in proteins including myoglobin[6], horseradish peroxidase[7], soluble guanylyl cyclase, as well as nitrophorins[8-10] demonstrating that the ν_{NO} vibration is a sensitive probe within the protein active site.

1.3 Outline of Thesis

The experiments and analysis described in this work walks through the background of lineshape analysis in two-dimensional infrared (2D IR) experiments and then applies rigorous lineshape analysis to increasingly complex systems. A detailed explanation of the 2D IR lineshape analysis which I have applied to iron-nitroysl systems is provided in Chapter 2. A

thorough look at the vibrational dephasing dynamics of SNP, which we have correlated to the local solvent polarity, is covered in Chapter 3. By extending the polarity and dephasing relationship of the nitrosyl stretching mode of SNP to the dephasing dynamics of the same mode in NP4 we can better understand the local environment of the distal pocket of the NP4 protein at two pH conditions. 2D IR studies of nitrophorin 4 are covered in Chapter 4.

REFERENCES

1. Bredt, D. S.; Snyder, S. H., Nitric Oxide: A Physiologic Messenger Molecule. *Annual review of biochemistry* **1994,** *63*, 175-95.

2. Lynch, M. S.; Cheng, M.; Van Kuiken, B. E.; Khalil, M., Probing the Photoinduced Metal-Nitrosyl Linkage Isomerism of Sodium Nitroprusside in Solution Using Transient Infrared Spectroscopy. *Journal of the American Chemical Society* **2011,** *133* (14), 5255-5262.

3. Tayama, J.; Ohta, K.; Tominaga, K., Vibrational Transition Frequency Fluctuation of the No Stretching Mode of Sodium Nitroprusside in Aqueous Solutions. *Chem. Lett.* **2012,** *41* (Copyright (C) 2012 American Chemical Society (ACS). All Rights Reserved.), 366-368.

4. Carducci, M. D.; Pressprich, M. R.; Coppens, P., Diffraction Studies of Photoexcited Crystals: Metastable Nitrosyl-Linkage Isomers of Sodium Nitroprusside. *J. Am. Chem. Soc. FIELD Full Journal Title:Journal of the American Chemical Society* **1997,** *119* (11), 2669-2678.

5. Manoharan, P. T.; Hamilton, W. C., The Crystal Structure of Sodium Nitroprusside. *Inorganic Chemistry*.

6. Adamczyk, K.; Candelaresi, M.; Kania, R.; Robb, K.; Bellota-Anton, C.; Greetham, G. M.; Pollard, M. R.; Towrie, M.; Parker, A. W.; Hoskisson, P. A.; Tucker, N. P.; Hunt, N. T., The Effect of Point Mutation on the Equilibrium Structural Fluctuations of Ferric Myoglobin. *Phys. Chem. Chem. Phys.* **2012,** *14* (Copyright (C) 2012 American Chemical Society (ACS). All Rights Reserved.), 7411-7419.

7. Simpson, N.; Adamczyk, K.; Hithell, G.; Shaw, D. J.; Greetham, G. M.; Towrie, M.; Parker, A. W.; Hunt, N. T., The Effect on Structural and Solvent Water Molecules of Substrate Binding to Ferric Horseradish Peroxidase. *Faraday Discuss* **2015,** *177*, 163-79.

8. Spiro, T. G.; Soldatova, A. V.; Balakrishnan, G., Co, No and O2 as Vibrational Probes of Heme Protein Interactions. *Coordination Chemistry Reviews* **2013,** *257* (2), 511-527.

9. Soldatova, A. V.; Ibrahim, M.; Olson, J. S.; Czernuszewicz, R. S.; Spiro, T. G., New Light on No Bonding in Fe(Iii) Heme Proteins from Resonance Raman Spectroscopy and Dft Modeling. *Journal of the American Chemical Society* **2010,** *132* (13), 4614-4625.

10. Nienhaus, K.; Maes, E. M.; Weichsel, A.; Montfort, W. R.; Nienhaus, G. U., Structural Dynamics Controls Nitric Oxide Affinity in Nitrophorin 4. *The Journal of biological chemistry* **2004,** *279* (38), 39401-7.

CHAPTER 2

RIGOROUS LINE SHAPE ANALYSIS THROUGH GLOBAL FITTING OF TWO DIMENSIONAL INFRARED SPECTRA

2.1 Conceptual Description of a Two-Dimensional Infrared Experiment

It is helpful to have a conceptual picture of 2D IR while discussing the specifics of the anyalysis of 2D IR experiments. The work presented in this dissertation looks at how the NO stretching mode (ν_{NO}) changes as a function of the local environment. What are the physical changes and how can we observe those experimentally? How can we use the experimental observables to make meaningful predictions? It is of course the goal of the studies presented in this dissertation to be able to apply that knowledge to understand complex systems, but we will begin simply with a single interaction with infrared light.

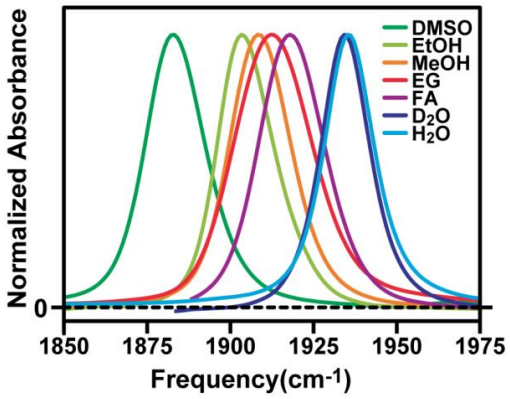

Figure 2.1 FTIR of ν_{NO} stretching mode of sodium nitroprusside in a series of seven solvents.[1]

The first experimental observation that we make in infrared spectroscopy is to measure the average frequency of the vibration in question. We can also measure how that the frequency changes as a function of solvent, which is known as the solvochomatic shift. Consider the

Fourier transform infrared (FTIR) spectrum of the ν_{NO} strech of sodium nitroprusside (SNP) in a series of solvents shown in Figure 2.1 where ν_{NO} shifts drastically with solvent. As the solvent changes, the nature of the intermolecular forces between SNP and the solvent change. This change is observed as a shift in the center frequency of the ν_{NO} vibrational mode. A shift in frequency results from a change in strength of the N-O bond. When describing a molecular vibration using Hooke's Law the the spring constant, k, is proportinal to the bond strength as well as the frequency of oscillation as shown in Equation 2.1 where μ is the reduced mass.

$$\nu = \frac{1}{2\pi}\sqrt{\frac{k}{\mu}} \qquad 2.1$$

The next experimental observation is the linewidths of the peaks, which tell us something about the distribution of frequencies. The distribution is a result of the underlying dynamics of the system but the measurement is not easily resolved into molecular level changes. In an FTIR we see an ensemble average so we see all the possible frequencies of ν_{NO} averaged together. We can gain a deeper understanding of how ν_{NO} is changing by measuring the frequency changes over time. The cartoon in Figure 2.2 shows how the stretching frequency changes as a function of time as the chemical bonds within the molecule vary. The change in frequency from υ to υ' can

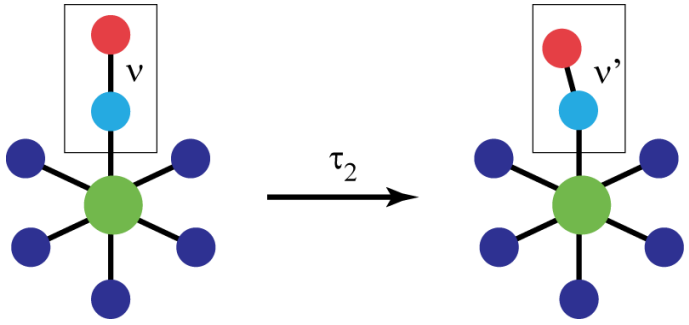

Figure 2.2 Cartoon of metal complex with a vibration υ which changes with time τ_2.

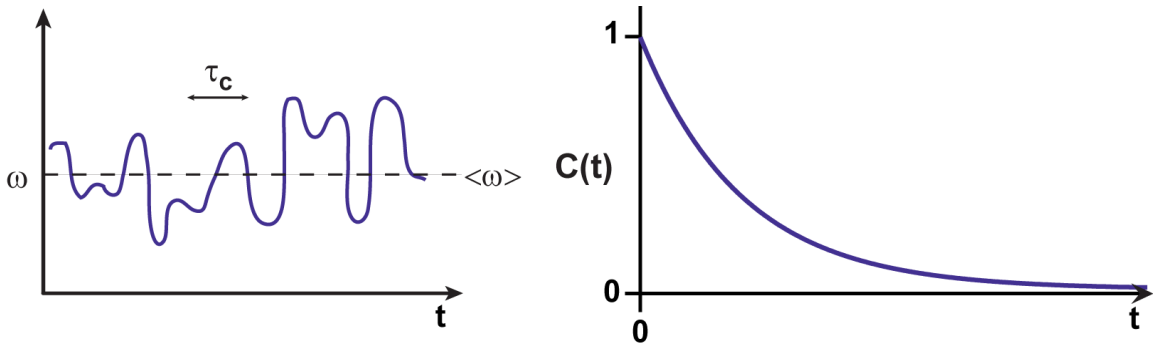

Figure 2.3 Deviation from average vibrational frequency $\langle\omega\rangle$ of an oscillator as a function of time and a frequency-frequency correlation function.

be caused by the change in the solute-solvent environment, changes in geometry, and energy distribution in the molecule under study. If we could map how the frequency changes over time we would have the information to build a movie of how the molecule interacts with the environment. The way in which we describe the change in the vibrational mode over time is through frequency-frequency correlations functions (FFCF) of the form of equation 2.2.

$$C(t) = \langle \delta\omega(t)\delta(0) \rangle \qquad 2.2$$

FFCFs show how well correlated the frequency at some time *t* is to the frequency at time zero. In other words, FFCFs tracks how well the mode remembers where it was at the beginning as time goes on. Figure 2.3 pictorially describes how the frequency of a mode changes in a random walk about the mean frequency $\langle\omega\rangle$ as a function of time with a corresponding correlation function that shows how after some correlation time τ_c the mode is no longer dependent on where it was at time zero. We measure FFCFs using 2D IR, where the x axis maps environment of the molecule at the beginning of the experiment and the y axis shows the environment at the end of the experiment. FFCFs are backed out from a 2D IR experiment by performing lineshape analysis. FFCFs obtained in all of the experiments presented in this work are of the form of

equation 2.2 . From the resulting FFCFs the ultimate goal is to tie the dephasing dynamics to underlying intermolecular interactions and environments.

$$C_{11}(t) = \sum_{n=1}^{2} \Delta_n^2 \exp\left(-\frac{t}{\tau_{cn}}\right) + \frac{\delta(t)}{T_2} \qquad 2.3$$

2.2 Calculating Nonlinear Response for 2D IR

In order analyze 2D IR spectra we will simulate 2D IR signals using nonlinear response formalism. We have drawn upon the nonlinear response formalism published by others and added (or while adding) simplifications for our system.[2-3] The quantum mechanical description of nonlinear spectroscopy begins with the Hamiltonian describing the matter (H_m), which describes the molecule, as well as the Hamiltonian describing the coupling that occurs from classical external fields (H_{int}) shown in equation 2.4.

$$H_s = H_m + H_{\text{int}} \qquad 2.4$$

The H_m term is composed of the Hamiltonians describing the system, the bath, and the system bath interaction.

$$H_{\text{int}} = \mu(Q) \cdot E(r,t) \qquad 2.5$$

$\mu(Q)$ is the dipole moment operator and $E(r, t)$ is the electric field of the external radiation (in our case always an ultrashort mid-IR pulse). The interaction results in a time-dependent material polarization $P(r, t)$. It is this polarization that we are able to measure during our 2D IR

experiments. Those wishing for further detail on derivation of the signal should refer to references 2 and 3.

The 2D IR experiment measures the third order polarization ($P^{(3)}$) of the sample resulting in the interaction of the sample with three time-ordered infrared fields. Using nonlinear response formalism we will build the molecular response from the interaction of the system. For the sake of this work we will focus on a three level system.

It is often more useful to describe the third-order nonlinear response in a conceptual way, so we will begin with a conceptual walk through the possible energy transitions that a single oscillator can undergo in a three level system. Figure 2.4 visually shows all of the transitions possible with three time ordered light-matter interactions on a three level system. The understanding given in the energy level diagrams is incomplete because it does not take into account phase matching in 2D experiments. The Feynman diagrams represented in Figure 2.5

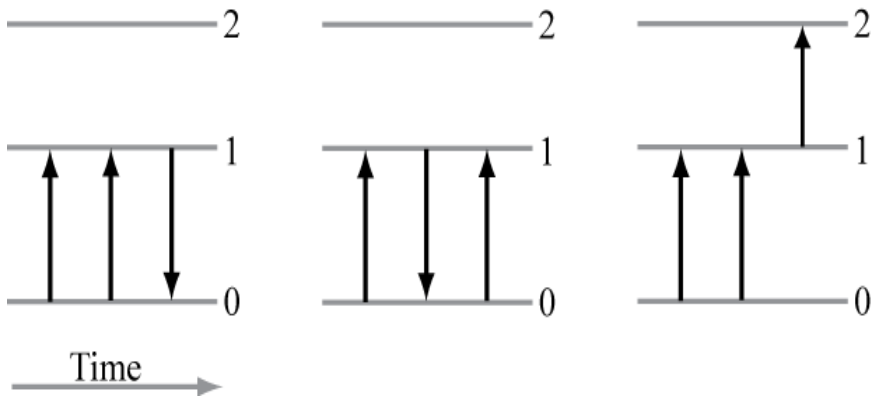

Figure 2.4 A simplified schematic of the possible transitions of a single oscillator in a three-level system.

describe all of the possible energy states that a three level system can go through in a 3rd order

nonlinear experiment in which the phase matching conditions include $k_s = -k_1 + k_2 + k_3$ and $k_s = k_1 - k_2 + k_3$ where subscripts describe the ordering of the pulse sequence.

As shown in the Feynman diagrams in Figure 2.5, in the 2D IR experiment the system starts out in the ground vibrational state. This is described as $\rho = |0\rangle\langle 0|$. We build the response functions by adding an interaction to the response function for each successive light-matter interaction. The beginning of the experiment is defined as $t = 0$ and time begins when the first light pulse interacts with the sample.

The first pulse puts the system into a coherence between the ground and first excited state, in effect labeling the initial frequency. This initial frequency will be displayed along the

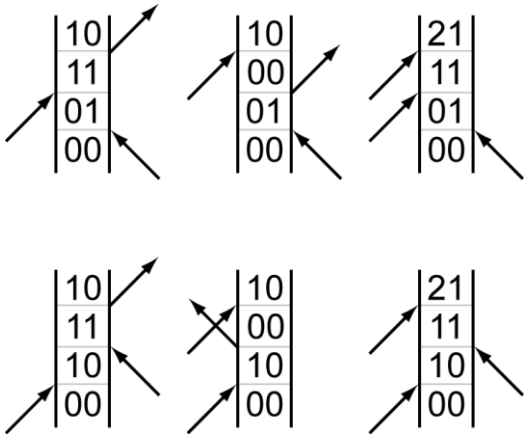

Figure 2.5 Feynman diagrams describing all of the possible transitions giving rise to signal in a 2D IR experiment. The top row represents the rephasing pathways and the bottom row represents the non-rephasing pathways which differ by a phase difference of $\pi / 2$.

ω_1 axis. The coherence oscillates at the frequency corresponding to the energy difference between the ground and first excited state:

$$\omega_{01} = \frac{E_1 - E_0}{\hbar} \tag{2.6}$$

The coherence evolves over the time period τ_1. The second pulse puts the system back into a population in either the ground or first excited state. This state is allowed to evolve over the time τ_2 after which the third pulse puts the system back into a coherence, labeling the state of the system at the time of the third pulse. The time delay τ_1 is scanned and Fourier transformed in order to obtain the ω_1 frequency axis. The vibrational echo emitted from the sample is over-lapped with a local oscillator field, and then dispersed onto an array detector allowing the ω_3 axis to be detected spectrally. Each 2D IR spectrum is collected with a set τ_2 time, which is

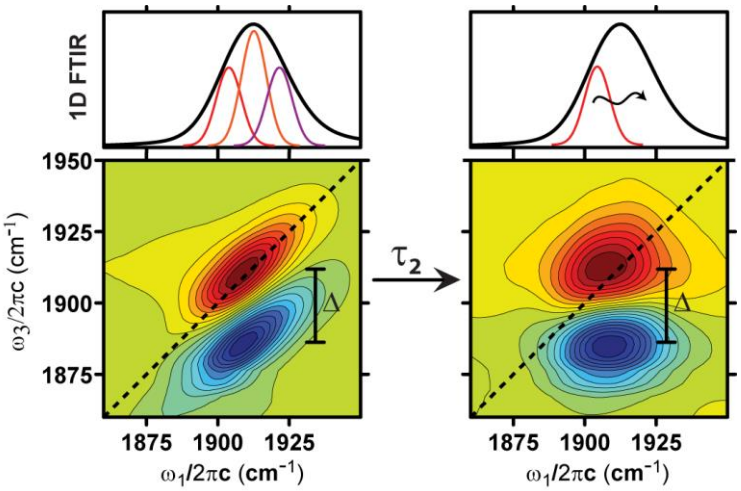

Figure 2.6 Underlying distributions giving rise to FTIR and 2D IR spectra at early time (on the left) and times greater than the correlation time (on the right). The rounding out of the 2D IR peaks is indicative of spectral diffusion

then varied over the course of the experiment. The distribution of frequencies evolves as a function of τ_2 through spectral diffusion. This is evident in 2D IR spectra as the turning and rounding out of the peak from elongated along the diagonal to a symmetric peak. The change in lineshape is caused by a change in distribution of the local environment of the reporting mode. By understanding how the lineshape changes we can understand how the local environment of the molecule changes. Figure 2.6 shows how the distributions change with increasing τ_2. The 2D IR represented in Figure 2.6 demonstrates how the same FTIR spectrum can be represented by different frequency distributions, a powerful testament to the limitation of using FTIR alone to understand distributions. Dephasing dynamics and relaxation mechanisms cause the line broadening which affects the FTIR and 2D IR lineshapes but are more easily observed in the later 2D IR spectra. Since 2D IR is a time-resolved technique we can watch the dynamics that give rise to the linewidths present in the FTIR.

2.3 Simulations of 2D IR Spectra

Methods for utilizing third order nonlinear response formalism in order to simulate 2D IR spectra have been published extensively. Rather than repeat all of equations used, I will highlight the assumptions and deviations that were utilized in later chapters.

- **Harmonic Scaling of Frequency – Frequency Correlation Functions**

  When assuming harmonic scaling between the correlation functions for 0, 1, and 2 vibrational states are

$$C_{22}(t) = 2C_{21}(t) = 2C_{12}(t) = 4C_{11}(t) \qquad 2.7$$

Our work with SNP revealed that harmonic scaling often does not correctly calculate the 2D IR spectra, particularly when the time scales of the $0 \rightarrow 1$ and $1 \rightarrow 2$ transitions are clearly different. When harmonic scaling cannot be used, such as with the nitrosyl stretch of SNP, an amplitude correction factor can be utilized. To correct for this deviation we included the scaling factor x resulting in the relationship between correlation functions shown in Equation 2.8.

$$C_{22}(t) = 2xC_{21}(t) = 2xC_{12}(t) = 4x^2C_{11}(t) \qquad 2.8$$

- **Harmonic Scaling of Dipole Moment**

  In harmonic scaling the relationship between the dipole moment for the $0-1$ and $1-2$ transitions, μ_{01} and μ_{12}, is

$$\mu_{12} = \sqrt{2}\mu_{01} \qquad 2.9$$

  If the absolute magnitude of the fundamental and overtone do not scale as one would expect as a result of this approximation, then the transition dipole μ_{01} is assumed to be 1 and the μ_{12} dipole is allowed to float with fitting parameters to correct for non-harmonic scaling.

- **Assumption of Gaussian Dynamics**

  It is useful to assume that the underlying dynamics of vibrational modes under study are Gaussian. This allows an analytical solution for the FFCFs, however this is not always the case. While this assumption was used in the studies shown in this work it is important to note that the underlying dynamics in many systems are clearly not Gaussian. Previous

work has shown that deviation from Gaussian dynamics can be seen in the wings of 2D IR peaks.[4] We do not include any correction to this in the work presented in this thesis, but the potential deviation from this approximation is seen in the experiments presented in Chapter 3.

- **Harmonic Approximation for Vibrational Lifetimes**

  Harmonic scaling of vibrational lifetimes has been utilized in all of the work presented.

2.4 Fitting of Experimental and Simulated 2D IR Spectra

In order to obtain the most accurate FFCFs for all of the correlation functions described in this work normalized simulated 2D IR spectra at all τ_2 times are fit to normalized experimental spectra while floating the correlation function parameters. Other parameters used to fit the spectra include the dipole moment (μ_{12}) and a correction factor for scaling of FFCFs. The resulting FFCFs obtained are in the form of Equation 3.2. While the time scales were on the same order of magnitude as those obtained by other lineshape analysis methods, the time scales obtained by the fitting described in section 2.3 provide a better match with experimental 2D IR. The scripts used to fit 2D IR experiments are shown in appendix A.

2.4 Other Methods of Lineshape Analysis

The analysis presented in this work has been developed in order to improve on the current standard of 2D IR analysis where many years of work have continued to improve the ability of spectroscopists to extract useful and meaningful information from 2D IR. The method of simultaneously fitting all experimental spectra was used in order to obtain correlation functions with more confidence than the current analysis techniques used by other groups.

Several methods of extracting FFCFs from 2D IR spectra have been developed since the development of 2D IR. Methods used previously to extract correlation functions include: nodal line slope, center line slope[5], index of inhomogeneity[6], ellipticity[7], slope of phase, and peak shift. Each method includes limitations. The nodal line slope measures the slope of the line at the node between the $0 \rightarrow 1$ and $1 \rightarrow 2$ peaks. An obvious limitation of the method is that the slope is dependent on the correlation functions giving rise to both peaks without a way to decouple them. This becomes a particularly large issue when it is clear in experimental data that both peaks do not turn at the same rate. The index of inhomogeneity utilizes the differing amplitudes of the rephasing and nonrephasing spectra.[8] At early times the rephasing spectrum has larger amplitude and as τ_2 increases they become more similar in amplitude. Often lineshape analysis methods are used to find time scales and then final amplitude values are found by fitting simulated FTIR spectra to experimental FTIR as demonstrated by Fayer et al.[5]

During the analysis of our 2D IR data sets described in great length in later chapters we found that this is not the most accurate way to obtain FFCFs from our systems. In this work all FFCFs have been determined by using the center line slope to obtain a first guess of FFCFs and then nonlinear response formalism is used to simulated 2D IR spectra which are fitted to experimental 2D IR spectra. The obtained FFCFs are then used to simulate the FTIR in order to check the goodness of the FFCF.

2.5 Lineshape Analysis in a Two Component System

Obtaining FFCFs by iterative fitting simulated to experimental 2D IR spectra at all τ_2 times for a three level system can easily be extended to more complex systems such as proteins

with multiple conformers. In the event of two non-interacting, non-interconverting modes, such as in the case of η_{NO} in the pH-dependent protein nitrophorin 4, you can simulate the 2D IR spectra using two sets of all of the response functions corresponding to the Feynman diagrams above. Each set of response functions is independent and FFCFs obtained correspond to those of each η_{NO} peak. It is important to note that all of the work presented within this dissertation represents non-interacting, non-interconverting modes. In the instance of modes coupling to other modes response functions for cross-peaks would need to be added to the model. In the case of interconverting conformers population transfer terms would need to be added.

REFERENCES

1. Brookes, J. F.; Slenkamp, K. M.; Lynch, M. S.; Khalil, M., Effect of Solvent Polarity on the Vibrational Dephasing Dynamics of the Nitrosyl Stretch in an Fe-Ii Complex Revealed by 2d Ir Spectroscopy. *J Phys Chem A* **2013,** *117* (29), 6234-6243.

2. Sung, J.; Silbey, R. J., Four Wave Mixing Spectroscopy for a Multilevel System. *The Journal of Chemical Physics 115* (20), 9266.

3. Mukamel, S., *Principles of Nonlinear Optical Spectroscopy*. Oxford University Press: New York, 1995.

4. Roy, S.; Pshenichnikov, M. S.; Jansen, T. L. C., Analysis of 2d Cs Spectra for Systems with Non-Gaussian Dynamics. *Journal of Physical Chemistry B* **2011,** *115* (18), 5431-5440.

5. Kwak, K.; Rosenfeld, D. E.; Fayer, M. D., Taking Apart the Two-Dimensional Infrared Vibrational Echo Spectra: More Information and Elimination of Distortions. *Journal of Chemical Physics* **2008,** *128* (20).

6. Roberts, S. T.; Loparo, J. J.; Tokmakoff, A., Characterization of Spectral Diffusion from Two-Dimensional Line Shapes. *Journal of Chemical Physics* **2006,** *125* (8).

7. Lazonder, K.; Pshenichnikov, M. S.; Wiersma, D. A., Easy Interpretation of Optical Two-Dimensional Correlation Spectra. *Opt Lett* **2006,** *31* (22), 3354-3356.

8. Khalil, M.; Tokmakoff, A., Signatures of Vibrational Interactions in Coherent Two-Dimensional Infrared Spectroscopy. *Chemical Physics 266* (2-3), 213-230.

CHAPTER 3

THE EFFECT OF SOLVENT POLARITY ON THE VIBRATIONAL DEPHASING DYNAMICS OF THE NITROSYL STRETCH IN AN Fe^{II} COMPLEX REVEALED BY 2D IR SPECTROSCOPY

The work presented in this chapter has been previously published in

Brookes, J. F.; Slenkamp, K. M.; Lynch, M. S.; Khalil, M. Effect of Solvent Polarity on the Vibrational Dephasing Dynamics of the Nitrosyl Stretch in an Fe Complex Revealed by 2D IR Spectroscopy. *J Phys Chem A* 2013,117 (29), pp 6234-66243.

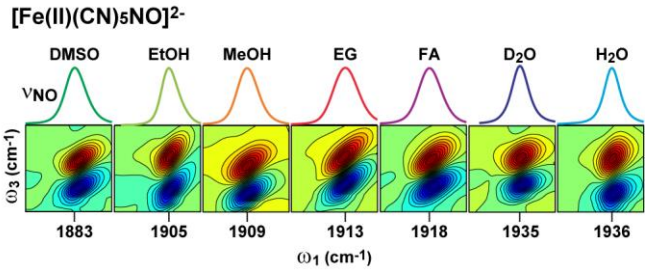

The vibrational dephasing dynamics of the nitrosyl stretching vibration (ν_{NO}) in sodium nitroprusside (SNP, $Na_2[Fe(CN)_5NO]\cdot 2H_2O$) are investigated using two-dimensional infrared (2D IR) spectroscopy. The ν_{NO} in SNP acts as a model system for the nitrosyl ligand found in metalloproteins which play an important role in the transportation and detection of nitric oxide (NO) in biological systems. We perform a 2D IR lineshape study of the ν_{NO} in the following solvents: water, deuterium oxide, methanol, ethanol, ethylene glycol, formamide, and dimethyl sulfoxide. The frequency of the ν_{NO} exhibits a large vibrational solvatochromic shift of 52 cm^{-1}, ranging from 1884 cm^{-1} in dimethyl sulfoxide to 1936 cm^{-1} in water. The vibrational anharmonicity of the ν_{NO} varies from 21 to 28 cm^{-1} in the solvents used in this study. The

frequency-frequency correlation functions (FFCFs) of the ν_{NO} in SNP in each of the seven solvents are obtained by fitting the experimentally obtained 2D IR spectra using nonlinear response theory. The fits to the 2D IR lineshape reveal that the spectral diffusion timescale of the ν_{NO} in SNP varies from 0.8 – 4 ps and is negatively correlated with the empirical solvent polarity scales. We compare our results with the experimentally determined FFCFs of other charged vibrational probes in polar solvents and in the active sites of heme proteins. Our results suggest that the vibrational dephasing dynamics of the ν_{NO} in SNP reflect the fluctuations of the non-homogeneous electric field created by the polar solvents around the nitrosyl and cyanide ligands. The solute solvent interactions occurring at the trans-CN ligand are sensed through the π-backbonding network along the Fe-NO bond in SNP.

3.1 INTRODUCTION

The spectral positions, amplitudes, and lineshapes of molecular vibrational absorption bands are extremely sensitive probes of a molecule's environment. There is a growing body of experimental and theoretical work aimed at understanding how heterogeneous fluctuating electric fields produced by polar solvents and/or biological molecules are measured by the vibrational frequency shifts and dephasing dynamics of small neutral and charged IR active probes.[1-6] Time-dependent vibrational frequency shifts of an IR active vibration (ω) are encoded in the frequency-frequency correlation function (FFCF, $\langle \omega(t)\omega(0) \rangle$). Nonlinear femtosecond IR techniques such as two-dimensional IR (2D IR) spectroscopy and three-pulse vibrational echo peak-shift experiments have successfully measured the FFCFs of amide I vibrations in proteins and peptides, OH(OD) vibrations of HOD in aqueous solutions, and the carbonyl (ν_{CO}), cyanide (ν_{CN}), azide and nitrosyl (ν_{NO}) stretching vibrations in ions, metal complexes, active site of

enzymes and non-natural amino acid side chains.[7-27] These studies explore how the amplitudes and timescales of vibrational frequency fluctuations report on the hydrogen bonding dynamics in neat polar liquids and on the functionally-relevant dynamics in the interior and exterior of proteins and peptides. Recently, there have been reports of measuring the FFCFs of the ν_{NO} in nitrosyl containing metalloproteins.[28-29] However, the 2D IR spectroscopy of the ν_{NO} has not been extensively studied. In this work, we use a model iron nitrosyl compound to systematically investigate the effect of the local polar solvent environment on the dephasing dynamics of the ν_{NO}.

Nitric oxide (NO) is a highly reactive messenger molecule which plays an important role in regulating the immune, nervous and cardiovascular systems of mammals. The frequency of the ν_{NO} has been studied extensively for probing Fe-NO bonding in several heme-NO proteins including myoglobin, soluble guanylyl cyclase (sGC) and nitrophorins (NPs).[30-32] Vibrational Stark effect spectroscopy has shown the nitrosyl stretch to be a very sensitive probe of the local electric field in proteins and model heme complexes.[33-34] Sodium nitroprusside (SNP) serves as an excellent model system for studying the effects of Fe-NO bonding and solvent polarity on the vibrational dynamics of a nitrosyl ligand. SNP is a six-coordinate complex containing five cyanide ligands and one nitrosyl ligand in an octahedral geometry as shown in Figure 3.1. The crystal structure of SNP reveals that both the Fe-N-O and Fe-C-N bonds are linear, the nitrosyl ligand coordinates only with iron, and water-SNP interactions take place mainly at the cyanide ligands.[35-36] Both the CN and NO ligands are capable of accepting electron density from the iron center in the form of π-backbonding though their π^* orbitals. Therefore, there is a natural competition between the trans-CN and NO ligands for electron density from the metal known as the trans-effect (Fig. 1). The trans-effect has been implicated in the vibrational solvatochromism

of the ν_{NO} in SNP when dissolved in polar solvents.[37-38] While in the electronic ground state, the NO in SNP coordinates to the iron through the N atom (GS, ν_{NO} = 1909 cm^{-1} in methanol). However, two photoinduced metastable metal-nitrosyl linkage isomers exist where the nitrosyl is either bound through the O atom (MS1, ν_{NO} = 1794 cm^{-1} in methanol) or with the nitrosyl perpendicular (MS2, ν_{NO} = 1652 cm^{-1} in methanol) to the original bonding axis.[39-41] We have recently shown the presence of the metastable linkage isomers at room temperature in a methanol.[42] The sensitivity of the ν_{NO} in SNP to the Fe-N bonding geometry, the trans-ligand and solvent polarity makes it an excellent model system for studying the nonlinear vibrational spectroscopy of NO bound to heme proteins.

In this work we use 2D IR spectroscopy to investigate the effect of the local solvent environment on the dephasing dynamics of the nitrosyl stretching vibration in SNP. We measure the FFCF of the ν_{NO} in seven polar solvents. Our results reveal a negative correlation between the timescale of frequency fluctuations and empirical parameters of solvent polarity. We discuss the role of local solute-solvent interactions and the collective reorganization of the solvent which results in the vastly different solvent-dependent dephasing dynamics of the ν_{NO} in SNP.

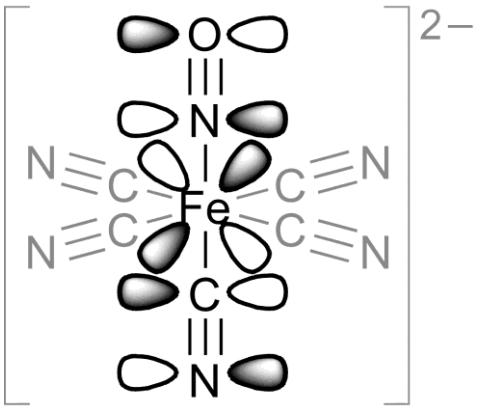

Figure 3.1 Structure of SNP highlighting the network of π-backbonding along the NO bond and the trans CN ligand.

3.2 EXPERIMENTAL METHODS

3.2.1 Materials. Sodium nitroprusside ($Na_2Fe(CN)_5NO{\cdot}2H_2O$, SNP) and solvents (> 99.9% pure, spectroscopic grade) were purchased from Sigma Aldrich Co. and used without further purification. Solutions of SNP dissolved in methanol (MeOH), water, deuterium oxide, ethylene glycol (EG), formamide (FA), and dimethyl sulfoxide (DMSO) were prepared to concentrations of 31, 41, 30, 37, 39, and 21 mM, respectively. A saturated solution of SNP in ethanol (EtOH) was prepared, filtered, and subsequently used for experiments. The FTIR spectra of the sample solutions were obtained using a JASCO FT/IR-4100 spectrometer with 2 cm^{-1} resolution. The sample was held in an FTIR sample cell with BaF_2 windows and a 100 μm thick Teflon spacer under ambient conditions.

3.2.2 2D IR experiments. The 2D IR experiment is performed with the 800 nm output of a commercial Spectra Physics Spitfire Pro-35F-XP regenerative amplifier operating at 1 kHz with 35 fs pulse duration and ~ 3 W average power. The mid-IR pulses are obtained by sending ~1 W of the 800 nm light to pump a two-pass optical parametric amplifier (OPA-800C, Newport). Near-IR signal and idler pulses from the OPA are spatially and temporally overlapped and undergo difference-frequency mixing in a 0.5 mm $AgGaS_2$ crystal to produce ~75 fs mid-IR pulses with spectral bandwidths greater than 200 cm^{-1} at center wavelengths of 5.3 μm.

The mid-IR pulse is sent into five-beam interferometer to generate three input pulses, a tracer beam and a local oscillator field. The interferometer has been described in detail previously.[43-44] The three input IR beams are arranged in a “boxcar” geometry, temporally

overlapped, and focused onto the sample with a spot-size of ~150 μm ($1/e^2$). The home-built sample cell is equipped with two 1 mm CaF_2 windows and a 100 μm Teflon spacer. The resulting background-free signal field is overlapped with the local oscillator field on a beamsplitter for heterodyne detection. Reflected and transmitted beam combinations are π out of phase with respect to each other and are vertically offset. The signal fields are detected at the focal plane of a spectrometer (Triax 190, Horiba Jobin Yvon, 150 mm^{-1} grating) using a 2 × 64 mercury cadmium telluride (MCT) array detector (IR0144, Infrared Systems Development). This experimental geometry allows us to subtract signals from the two linear arrays to perform "balanced detection" on a shot-to-shot basis which greatly improves our signal to noise by a factor of ~10. Further experimental details can be found in Ref. 44.

The 2D IR experiments are performed with each of the three input IR fields having pulse energies of 0.35 μJ and parallel polarizations. The IR coherence (τ_1) and waiting (τ_2) time delays are accurately controlled by Newport XMS50 linear stages. The τ_1 delay was scanned in 4 fs steps from 0 to 1.7–1.9 ps depending on the sample being studied. The τ_2 delay was scanned in unequal time steps from 0 to 6–70 ps, where the maximum time delay was dictated by the vibrational lifetime of the ν_{NO} in SNP dissolved in a particular solvent. Rephasing and non-rephasing experiments were performed at each τ_2 delay in order to construct absorptive 2D IR correlation spectra. The raw experimental data was zero padded to 32.8 ps and Fourier transformed along τ_1 to obtain the ω_1 axis. Each data point represents an average of 1500 laser shots and each τ_2 scan was collected twice and averaged to obtain the experimental 2D IR correlation spectra analyzed in this study. The final 2D IR spectrum is corrected for the phase ambiguities corresponding to drift of the relative timing between the local oscillator and signal fields. The correction is a phasing procedure which compares the projection of the 2D IR

spectrum along the ω_1 axis to a two-beam dispersed pump-probe spectrum collected for the same values of τ_2. The experimental spectral resolution in the ω_3 and ω_1 dimensions is 2 and 1 cm^{-1} respectively. The 2D IR spectra are smoothed in the ω_3 dimension by using a Savitzky-Golay FIR smoothing filter to remove narrow $H_2O_{(g)}$ absorptions of the signal from the air. The lineshapes before and after filtering were compared in order to ensure that smoothing did not affect the lineshape of the 2D spectrum.

3.2.3 2D IR spectral fitting. The experimental 2D IR spectra were fit by iteratively calculating the third-order nonlinear signal field as a function of τ_1 and τ_3 in the time domain and then Fourier transforming it to obtain theoretical spectra. 2D IR spectra of SNP in each solvent were simulated using a three-level system with a ground, first-excited and second-excited vibrational state (**0**, **1**, **2**) using the nonlinear response formalism detailed previously.[45-46] For our system, there are a total of 6 response functions for the rephasing and non-rephasing signals. We assume a separation of timescales for the vibrational and orientational dynamics for calculating the third-order nonlinear response functions. Our goal was to extract the underlying vibrational structural dynamics giving rise to the solvent-dependent 2D IR lineshapes of the ν_{NO} in SNP. We modeled the 2D lineshapes using the following form for the frequency-frequency correlation function (FFCF):

$$C_{\mathbf{11}}(t) = \sum_{n=1}^{2} \Delta_n^2 \exp\left(-\frac{t}{\tau_{cn}}\right) + \frac{\delta(t)}{T_2} \tag{3.1}$$

In the above expression, Δ_n and τ_{cn} describe the amplitude and timescales of the frequency fluctuations in the Kubo model, $\delta(t)$ is the Dirac delta function and T_2 represents the timescales of fast dynamics determining the homogenous linewidth of the ν_{NO} in SNP. Analytical expressions for the nonlinear dephasing functions in terms of the correlation functions

are obtained using the methodology described in Ref. 45. The rotational correlation functions were written assuming a symmetric diffuser with an orientational diffusion constant D_{or} using the values in Table 3.1. We accounted for the effects of vibrational population relaxation by introducing exponential relaxation rates into the vibrational response functions during all three time periods and assuming a harmonic approximation for our three-level system. For example, if the vibrational lifetime for the first excited state of ν_{NO} is T_1, then the vibrational lifetime of the second excited state is $1/2T_1$.[47-48] We found that the harmonic scaling relations could not be used for the energy gap fluctuations to describe the vibrational dynamics of our three level system. To account for the anharmonicity and keep the number of floating parameters in our model low, we assume the following relationships for our frequency-frequency correlation functions:

$$C_{22}(t) = 2xC_{21}(t) = 2xC_{12}(t) = 4x^2C_{11}(t) \tag{3.2}$$

In the above expression, *x* is the amplitude correction factor for the correlation functions. If we assumed harmonic scaling to relate the vibrational dynamics of the **0**, **1**, and **2** vibrational states of ν_{NO}, *x*=1. For each solvent, experimental 2D IR spectra for all τ_2 points were fit simultaneously by floating parameters from the correlation functions (Δ_n and τ_{cn} (n=1-2), *x* and T_2). Additionally, the magnitude of the transition dipole moment between the first and second excited states, $|\mu_{12}|$, is adjusted iteratively. The simulated and experimental spectra were fit using a nonlinear least squares fitting routine written in MATLAB. The simulated and experimental FTIR spectra are shown in Figure 3.2.

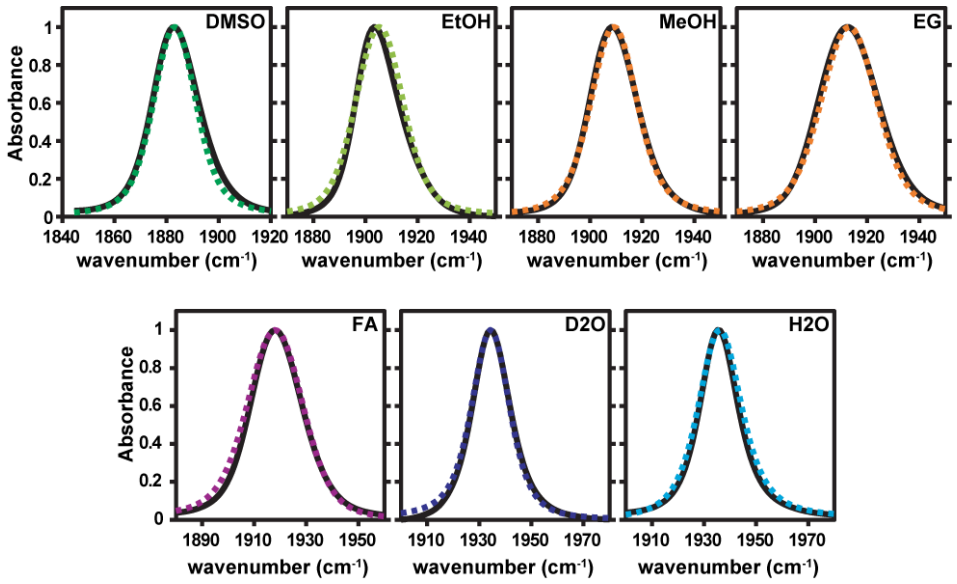

Figure 3.2 Solvent-subtracted normalized FTIR spectra of the ν_{NO} in SNP dissolved in various solvents and the corresponding simulated FTIR signal obtained by fitting .

3.3 RESULTS

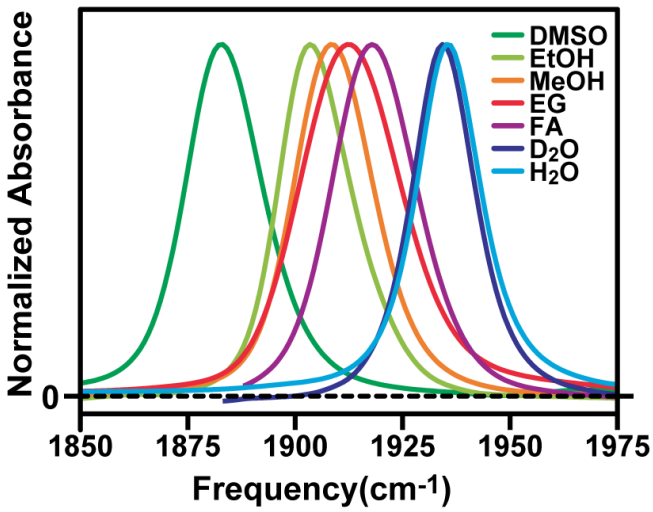

Figure 3.3 Solvent-subtracted normalized FTIR spectra of the ν_{NO} in SNP dissolved in various solvents.

3.3.1 FTIR spectra of the ν_{NO} in SNP dissolved in polar solvents. Figure 3.3 shows solvent-subtracted FTIR spectra of the non-degenerate ν_{NO} in SNP dissolved in the polar solvents used in this study. Table 1 lists the center frequency, spectral linewidth ($\Delta\nu_{FWHM}$), vibrational anharmonicity ($\Delta_{12} = 2\nu_{NO}^{1\leftarrow 0} - \nu_{NO}^{2\leftarrow 0}$), vibrational lifetime and anisotropy decays of the first excited state of the ν_{NO} (T_1,T_{or}),[38] and the integrated molar absorptivity ($\varepsilon = \int \varepsilon_\nu d\nu$). The table also lists empirical solvent parameters and the viscosity of the solvents used in this study.[49-51] The FTIR spectra illustrate a solvatochromic shift of the center frequency of the ν_{NO} as large as 52.3 cm^{-1}, ranging from 1883.5 cm^{-1} in DMSO to 1935.8 cm^{-1} in H_2O. The anharmonicity was accurately determined using the FTIR spectrometer, as we were able to measure the harmonically-disallowed transition to the second vibrationally excited state of the ν_{NO} (i.e., $\nu_{NO}^{2\leftarrow 0} \approx 3800\ cm^{-1}$) using saturated solutions of SNP in the solvents used in this study. The vibrational anharmonicity of the ν_{NO} is strongly solvent dependent and ranges from 21 cm^{-1} for H_2O to 28 cm^{-1} for EtOH. The variation in the Δ_{12} values shows how the potential energy surface for the ν_{NO} is modulated by specific solute-solvent interactions around the nitrosyl ligand. The integrated molar absorptivity for the ν_{NO} is similar in all solvents at ~ 3.6×10^4 M^{-1} cm^{-2}. The solvent-dependent vibrational lifetimes of the ν_{NO} in SNP have been measured and discussed extensively in Ref. 38. Along with the variation in frequency and anharmonicity, there is a large change in spectral linewidth of the ν_{NO} when SNP is dissolved in different solvents. The spectral linewidths listed in Table 3.1 are obtained by fitting a Voigt profile to each experimental lineshape. The FTIR linewidths of vibrations are governed by timescales of population relaxation, orientational diffusion and frequency fluctuations. For the ν_{NO} in SNP, the spectral linewidth (FWHM) ranges from 17 cm^{-1} in the aqueous solvents to 28 cm^{-1} in EG. While

some of the changes in linewidths can be accounted for by the differences in the vibrational lifetime and orientational diffusion times of the ν_{NO}, the spectral linewidths are far wider than the contribution from the vibrational population dynamics. For example, the contribution of the population and orientational diffusion time of the ν_{NO} in EG is respectively 6.8 and 6.6% of the total linewidth. Using 2D IR lineshape analysis we can measure the timescales of frequency fluctuations which dictate the linewidth of the ν_{NO} in SNP dissolved in various polar solvents.

Table 3.1 Spectroscopic observables of the nitrosyl stretching vibration in SNP dissolved in various solvents. The error bars correspond to a 95% confidence interval.

Solvent	ν_{NO} (cm^{-1})	$\Delta\nu_{FWHM}$ (cm^{-1})	Δ_{12} (cm^{-1})	T_1[a] (ps)	T_{or}[a] (ps)	ε ($M^{-1}cm^{-2}$)	$E_T^N(30)$[c]	A^N	Viscosity (mPa s)[f]
DMSO	1883.5±0.1	21.4±0.2	21.0±0.2	39	49	3.8×10^4	0.444	0.352	1.987
EtOH	1905.2±0.2	20.4±0.6	28.1±0.2	24[b]	-	-	0.654	0.677	1.074
MeOH	1909.0±0.1	21.8±0.2	24.8±0.2	29	46	3.6×10^4	0.762	0.754	0.544
EG	1913.0±0.1	27.3±0.6	22.6±0.2	28	>300	3.8×10^4	0.790	0.781[e]	16.1
FA	1918.4±0.3	24.1±0.8	25.8±0.3	25	62	3.3×10^4	0.775	0.708	3.343
D_2O	1934.6±0.1	16.9±0.1	23.8±0.3	22	20	3.2×10^4	0.991	-	-
H_2O	1935.8±0.1	17.7±0.2	20.8±0.2	7.3	16	3.7×10^4	1.000	1.000	0.890

[a] Ref. 38. [b] This work. [c] Ref. 49. [d] Ref. 49. [e] Ref. 50. [f] at 25 °C. Ref. 51.

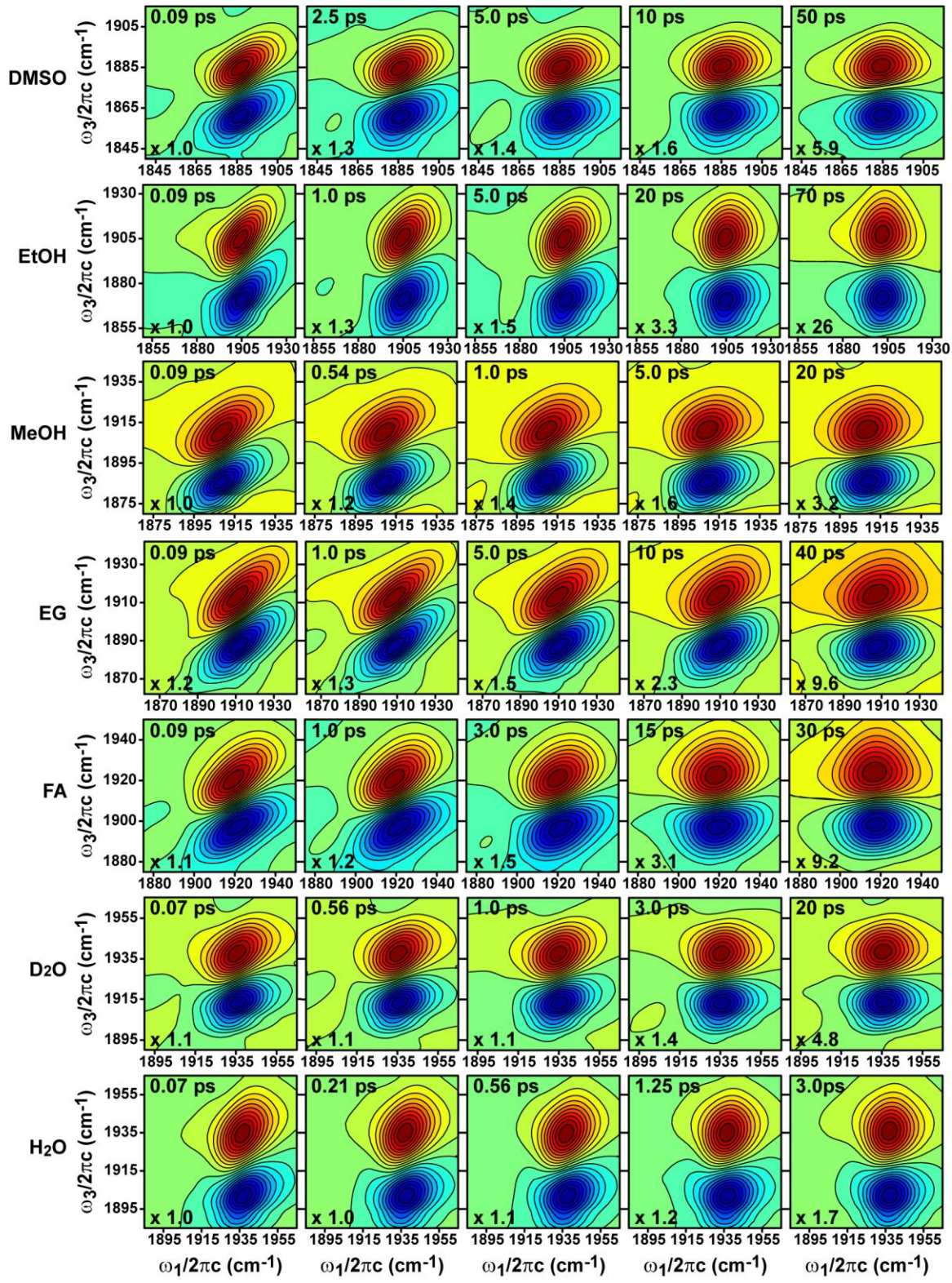

Figure 3.4 Experimental 2D IR spectra of the ν_{NO} in SNP dissolved in various solvents. Contour levels are drawn at 5% intervals. The τ_2 values and the normalization factors for each 2D plot are given in the top left and bottom left corners, respectively.

3.3.2 2D IR spectra of the ν_{NO} in SNP. Figure 3.4 displays the 2D IR spectra of the ν_{NO} in SNP dissolved in the solvents used in this study. The waiting time (τ_2) indicated in the top left corner of each 2D IR spectrum increases from left to right for each solvent. The 2D IR spectrum shows two peaks with opposite signs. The positive diagonal (i.e., when $\omega_1 = \omega_3$) peak displays transitions between the 0-1 vibrational states during both the evolution (τ_1) and detection time (τ_3) periods. The negative off-diagonal peak results from transitions between the 0-1 and 1-2 vibrational states during τ_1 and τ_3 respectively. The separation of the two peaks in the ω_3 dimension, directly measures the anharmonicity of the ν_{NO} and the values agree with those measured using FTIR spectroscopy (Table 3.1).

The 2D IR lineshape is a sensitive measure of the frequency-frequency correlation function (FFCF) which governs the spectral linewidth of the vibrational absorption band of the ν_{NO} in SNP. At small values of the waiting time, we see that the 2D IR lineshape is elongated along the diagonal reflecting a positive correlation between the frequencies excited during τ_1 and τ_3. As the waiting time increases, the 2D lineshape becomes more round, reflecting the loss of correlation among the system frequencies. This loss of correlation or spectral diffusion tracks the timescales of structural dynamics of the solute-solvent complex being studied. The ability to measure the timescales of solute-solvent structural dynamics with 2D IR experiments is limited by the vibrational lifetime of the chromophore under investigation.

It is evident from the 2D IR spectra in Figure 3.4 that the timescales for spectral diffusion for the ν_{NO} in SNP change drastically between the polar solvents. The timescales for frequency fluctuations seem to be the fastest in the aqueous solvents and slowest in ethylene glycol. It also appears that the timescales for the frequency fluctuations for the negative peak involving transitions to the second excited state of the ν_{NO} are different than those for the positive peak.

Figure 3.5 shows the effect of the non-harmonic scaling of FFCFs in the 2D spectrum of the nitrosyl stretching vibration in SNP dissolved in FA. To extract the parameters of the FFCF we fit the 2D IR spectra as described in the Methods section. We emphasize that in this paper we focus our efforts on understanding the 2D IR lineshape of the fundamental transition of the ν_{NO} in SNP.

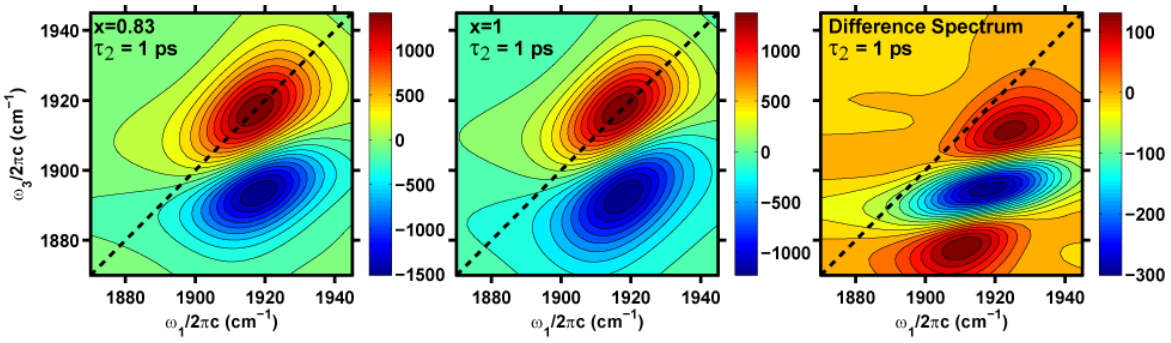

Figure 3.5 The effects of the non-harmonic scaling of the correlation function demonstrated for the simulated 2D spectra of the nitrosyl stretching vibration in SNP dissolved in FA. The only parameter changing in the two spectra is x in equation 3.2. All other parameters of the FFCF have been taken from table 2. The difference spectrum in the right panel depicts how the effect of the non-harmonic scaling are evident in the 2D spectrum.

3.3.3 Extraction of the FFCF parameters from fits of the 2D IR spectra of the ν_{NO} in SNP.

Figure 3.6 displays the 2D IR spectra resulting from the best fits of the experimental spectra assuming the form of the correlation functions given by Equations 1 and 2. The resulting parameters of the FFCF are listed in Table 3.2. We find that the homogenous dephasing time (T_2) for the ν_{NO} in SNP dissolved in all the solvents is on the order of 2 ps. The homogenous contribution to the IR linewidth is governed by fluctuations much faster than the experimental time window of a 2D IR experiment. We find that frequency fluctuations of the ν_{NO} in SNP can be described by a picosecond timescale (τ_{c1}) which ranges from 0.8-4.4 ps. The exception to this is ethylene glycol which shows longer dephasing dynamics on a ~13 ps timescale. As seen in

Figures 3.4 and 3.6, the 2D IR lineshape in EG is more elongated along the diagonal at early τ_2 time delays than the other solvents and it undergoes a process of slow spectral diffusion. The 2D IR spectra of the ν_{NO} in SNP dissolved in H_2O shows that the lineshape moves from being elongated along the diagonal to a rounded lineshape by 3 ps with a correlation time of 0.8 ps. The timescale of the FFCF of the ν_{NO} in D_2O is almost double that at 1.4 ps. The two alcohols used in the experiment, methanol and ethanol, have a τ_{c1} of 2.3 and 3.9 ps respectively. Both these solvents also exhibit frequency fluctuations on longer timescales of 25 and 29 ps, respectively. While also containing alcohol functional groups, EG has significantly different dephasing dynamics as discussed above. DMSO and FA are the only two solvents used in this study that do not contain –OH functional groups. Formamide, while not containing a hydroxyl group, is able to form hydrogen bond with the nitrosyl and cyanide ligands in SNP through the amide proton. The FFCF of the ν_{NO} in FA has a fast timescale of 2.2 ps. DMSO is the only aprotic solvent used in this study and it has a τ_{c1} timescale of 4.4 ps.

While the FFCF of the negative off-diagonal 2D peak is not analyzed in this study, the peak was fit floating both the dipole moment ($|\mu_{12}|$) and a factor accounting for the non-harmonic scaling of the lineshape functions (x) as discussed in the Methods section. We found this to be necessary to obtain quantitative agreement between the experimental and the simulated 2D spectra. The best-fit value of the $|\mu_{12}|$ of the ν_{NO} in SNP are listed in Table 3.2 for each solvent and we find that they are smaller than the value of $\sqrt{2}$ (except for EG), which would result from harmonic scaling. The amplitude correction factor for the lineshape functions was found to be less than 1 for all of the solvents used in this study, with the exception of ethanol. The amplitude correction parameters are shown in Table 3.3.

Table 3.2 Best fit parameters of the FFCF for the ν_{NO} in SNP extracted from fitting the 2D IR data. The error bars correspond to a 95% confidence interval.

Solvent	Δ_1 (ps^{-1})	τ_{c1} (ps)	Δ_2 (ps^{-1})	τ_{c2} (ps)	T_2 (ps)	$\lvert\mu_{12}\rvert$
DMSO	1.23±0.02	4.4±0.5			1.72±0.06	1.32
EtOH	1.40±0.06	3.8±0.5	0.50±0.02	29±9	2.1±0.1	1.36
MeOH	1.29±0.05	2.3±0.5	0.6±0.1	25±9	1.7±0.1	1.04
EG	1.69±0.01	12.7±0.4			1.60±0.02	1.49
FA	1.57±0.01	2.16±0.09	0.84±0.02	20±9	1.8±0.1	1.30
D_2O	1.22±0.03	1.4±0.1			2.0±0.1	1.40
H_2O	1.47±0.05	0.84±0.07			1.8±0.1	1.36

Table 3.3 Correction factor to account for non-harmonic scaling of the correlation function determined by 2D fitting for each solvent.

Solvent	***x***
DMSO	0.906
EtOH	1.058
MeOH	0.865
EG	0.978
FA	0.826
D_2O	0.858
H_2O	0.955

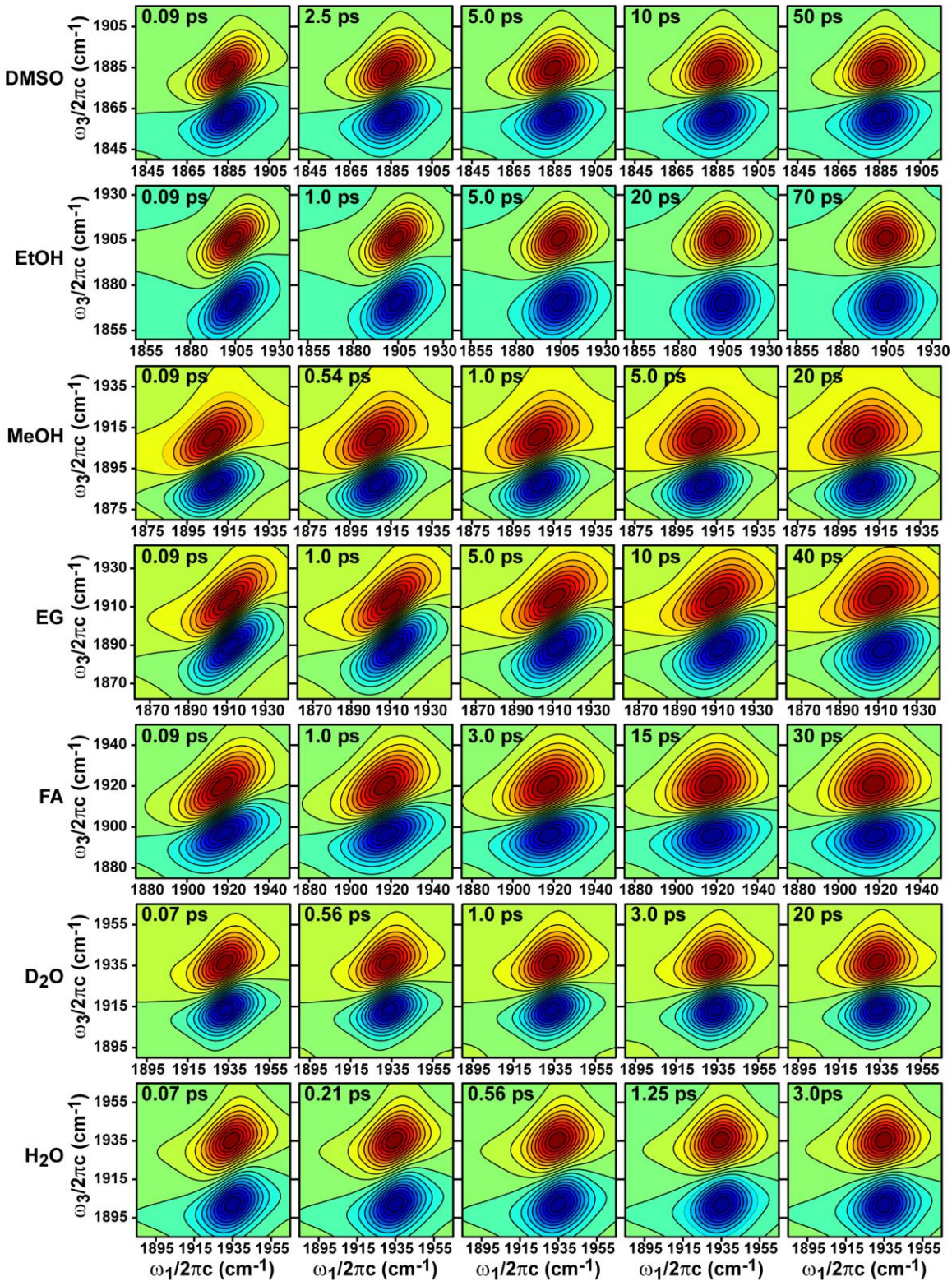

Figure 3.6 Fits of the 2D IR spectra of the ν_{NO} in SNP dissolved in various solvents. Contour levels are drawn at 5% intervals. The τ_2 values for each 2D plot are given in the top left corner.

3.4 DISCUSSION

Our results reveal a strong dependence of the solvent on the vibrational frequency fluctuations of the nitrosyl stretching vibration in SNP. In this section we discuss the microscopic origins for the vibrational solvatochromic shifts and the dephasing dynamics of the ν_{NO} in a series of polar solvents. We also compare our results with 2D IR studies measuring the FFCFs of other IR probe molecules in aqueous and polar solvents and in the interior of proteins.

3.4.1 Correlating 1D and 2D spectral parameters with empirical measures of solvent polarity. Chemists have developed several empirical scales for relating the effect of the medium (solvent) on chemical reactions.[49, 52-55] These empirical scales provide a way to define solvent polarity for a particular solvent, which cannot be quantitatively described by a single physical constant such as permanent dipole moment or dielectric constant. In this work we look for correlations of the ν_{NO} frequency and the timescales of frequency-fluctuation with two empirical parameters of solvent polarity: $E_T(30)$ and the acceptor number (AN). The parameter $E_T(30)$ is an empirical measure of solvent polarity based on the solvatochromism of the UV/vis spectrum of the pyridinium N-phenolate betaine dye developed by Reichardt. Values of $E_T(30)$ for commonly used solvents are often tabulated in units of kcal mol^{-1}. We use the unitless normalized $E_T^N(30)$ scale which has been normalized to the values of $E_T(30)$ in water and tetramethylsilane as the most polar and least polar solvents on the polarity scale.[49] The acceptor number (AN) is a dimensionless number based on the chemical shift of ^{31}P NMR of triethylphosphine oxide. The AN is a measure of the solvent's electrophilic properties and its ability to act as a Lewis acid.[56]

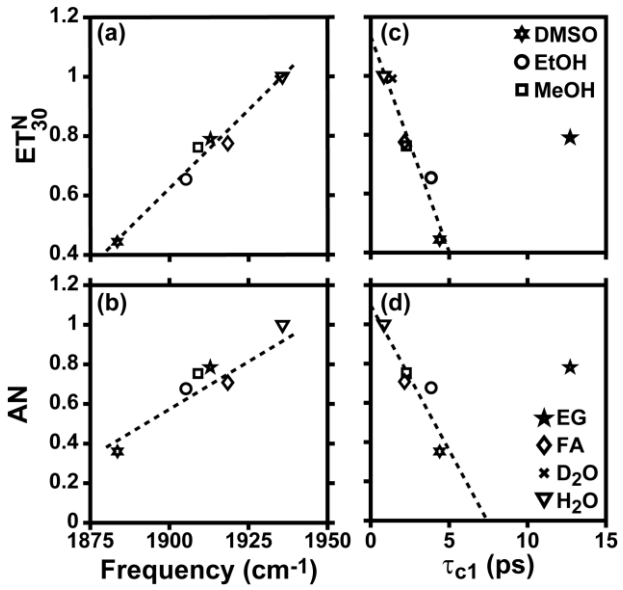

Figure 3.7 Correlation of the ν_{NO} frequency with (a) $E_T^N(30)$ and (b) AN polarity scales. The correlation of the vibrational dephasing timescale τ_{c1} with (c) $E_T^N(30)$ and (d) AN polarity scales. The values of $E_T^N(30)$ and AN for the solvents used in this study have been listed in Table 3.1.

Figure 3.7(a) and (b) show correlation plots of the frequency of the ν_{NO} in SNP with empirical solvent parameters. We note that $E_T^N(30)$ and AN have a positive correlation with the frequency shift with R^2 values of 0.98 and 0.92, respectively. Previous work from Estrin *et al.* has shown that the interaction of the solvent at the trans-cyanide ligand in SNP plays the most important role in the frequency shifts of the ν_{NO}.[37] They showed that the sensitivity of the metal-cyanide complex to the AN increased with an increasing number of CN ligands. In SNP, the cyanide ligands are negatively charged and able to donate electron density to the solvent through a π^* orbital. The transfer of electron density from the nitrogen atom of the cyanide ligand causes the cyanide to pull electron density from the iron center in the form of stronger π-backbonding. Consequently, the π-backbonding interaction of the Fe and nitrosyl ligand decreases resulting in an increase in the strength of the N-O bond and a higher frequency of the ν_{NO}. Recent work by

Huber et al, have measured a positive correlation of the ν_{CO} frequency and the AN in a dioxygen adduct of Vaska's complex and have attributed it to interactions of the trans O_2 ligand and the solvents which modulates the metal-CO π-backbonding interactions.[57] The parameter $E_T^N(30)$ has not been previously correlated with the frequency of the ν_{NO} in SNP, but it has been correlated with the ν_{NO} in ClNO by Bixby et al, where they see a similar positive correlation.[58] While there is a strong correlation with the frequency of the NO stretch and empirical measures of the solvent polarity, there is no correlation with the linewidth of the NO stretch or its vibrational lifetime.

The fits of the 2D IR spectra reveal that the homogenous dephasing time of the NO stretch is almost identical (~1.8 ps) in all the solvents studied here as seen from Table 3.2 and is not dependent on the solvent polarity. However, we notice a very interesting correlation between the shorter timescales of spectral diffusion (τ_{c1}) and the empirical solvent parameters as seen in Figures 3.7(c) and (d). The τ_{c1} values are negatively correlated with the $E_T^N(30)$ and AN parameters with R^2 values of 0.93 and 0.83, respectively. The fact that ethylene glycol is an outlier in Figure 3.7(c) is attributed to the large difference in viscosity of ethylene glycol in comparison with all the other polar solvents used in this study (see Table 3.1). Our results imply that the more polar and electrophilic the solvent, the faster the timescale for vibrational dephasing of the ν_{NO} in SNP. We note that even though we find a correlation between shorter timescales of spectral diffusion (τ_{c1}) and the empirical solvent parameters, this does not lead to a correlation of the linewidth of the NO stretch and solvent polarity. This is because the vibrational lifetimes and the longer timescales for spectral diffusion do not correlate with the empirical solvent parameters.

The correlation between dephasing times (τ_{c1}) and solvent polarity suggests that local electric field fluctuations may drive the vibrational dephasing dynamics of the ν_{NO} in SNP. Given the geometry of the molecule and the strong interactions between the CN ligands and the solvent, we do not expect a linear relationship between the ν_{NO} frequency and the local electric field. Based on our discussion of the π-backbonding network along the NO bond in SNP, we would expect that the frequency fluctuations of the ν_{CN} and the ν_{NO} to be anti-correlated. However, we do not observe a cross-peak in the 2D IR spectra between the ν_{CN} and the ν_{NO} at early waiting times suggesting that we can view the ν_{NO} as a local mode. We have also collected preliminary 2D IR spectra of the ν_{CN} in SNP dissolved in methanol and have measured timescales for spectral diffusion which are roughly half the value of τ_{c1} measured for the ν_{NO}. It has been previously observed that the ν_{CN} frequency in SNP is not very sensitive to solvent effects because of competing $\sigma-$ and π-backbonding interactions with the Fe atom.[37] Given that the frequency of the ν_{NO} is affected only by the π-backbonding interactions, we might expect differences in frequency fluctuations measured by the nitrosyl and cyanide ligands in SNP. We do not see any correlation between the anharmonicity of the ν_{NO} and the empirical solvent polarity scales of $E_T^N(30)$ and AN implying that there are specific solute-solvent H-bonding effects which are modifying the Fe-NO bonding geometry and affecting the vibrational dynamics of the ν_{NO}. All of the above observations suggest that the vibrational dephasing dynamics of the ν_{NO} are driven by the fluctuations of the electric field generated by the specific and non-specific interactions of the polar solvent molecules around the nitrosyl and cyanide ligands in SNP.

3.4.2 Vibrational dephasing dynamics of charged species in polar solvents. The role of electric field fluctuations in the dephasing dynamics of charged species dissolved in polar

solvents has been widely studied to understand the role of solvent fluctuations in chemistry and biology. There is growing experimental evidence that the collective dynamics of the solvent around small ionic solutes play the biggest role in determining the amplitudes and timescales of the vibrational frequency fluctuations of the solute.[2, 27, 59-62] Tominaga and co-workers have performed systematic studies of measuring the FFCFs of the cyanide, nitrosyl and azide stretching vibrations in ionic solutes dissolved in aqueous solvents.[2,26,55-58] Their studies find a common timescale ranging from 1-1.5 ps for the frequency fluctuations for various ions regardless of the vibration being studied. This similar timescale has been obtained in experimental studies of the OH(OD) stretch of HOD in $D_2O(H_2O)$.[12-13, 63-64] Molecular dynamics simulations have been used to obtain the FFCF of the azide stretch in D_2O and the OH(OD) stretch of HOD in $D_2O(H_2O)$.[5, 11, 65] The simulation studies have shown that the experimentally measured picosecond vibrational dephasing dynamics are driven by electric field fluctuations originating from collective reorganization of the hydrogen bonding network. In addition, molecular dynamic simulations have shown that the hydrogen bonding dynamics in methanol are three times slower than those in water.[66]

The role of collective hydrogen bonding dynamics driving electric field fluctuations which are measured by the vibrational FFCFs is borne out by our measurements of the ν_{NO} in SNP dissolved in protic solvents. Tominaga and co-workers have recently measured the FFCF of the ν_{NO} in SNP dissolved in aqueous solvents using three-pulse vibrational echo peak shift spectroscopy.[27] Their results reveal vibrational dephasing timescales of 1.1 ps for the ν_{NO} in SNP dissolved in H_2O and D_2O, homogenous dephasing times (denoted as T_2*) of 1.2 ps (1.7 ps) for H_2O (D_2O) and the presence of a static component to the FFCF for SNP dissolved in D_2O. In contrast, our experiments measure an isotopic effect in the τ_{c1} time scale which is 1.4 ps for D_2O

and 0.84 ps for H_2O and we do not observe any static inhomogeneity for SNP dissolved in D_2O. As noted previously, the homogenous dephasing time (T_2) is ~ 1.9 ps in the aqueous solvents, similar to the value reported for D_2O in Reference 27. We attribute the discrepancy in the FFCF parameters obtained in our study and those reported in Reference 27 to the use of two different experimental techniques and the use of different anharmonicities for the ν_{NO} (see Table 3.1). We note that the τ_{c1} timescale for the ν_{NO} is 0.8 ps and 1.4 ps in H_2O and D_2O respectively which is similar to that measured by the experiments of other ions in aqueous solvents. Additionally, the τ_{c1} for the ν_{NO} in SNP is ~3 times longer in MeOH than in H_2O. Based on the discussion above, and comparison to the reported FFCFs of ions in aqueous solutions, we propose that collective hydrogen bonding dynamics which modulate the electric field along the NO bond, govern the picosecond vibrational dephasing dynamics of the ν_{NO} in SNP dissolved in the protic solvents used in this study. Only three solvents, FA, MeOH and EtOH display vibrational dephasing dynamics of the ν_{NO} on timescales >20 ps. While these timescales roughly scale with the viscosity of the solvents, it is presently difficult to shed light on the microscopic origins of the 20 ps timescale without further experiments and/or molecular dynamics simulations.

3.4.3 Vibrational dephasing dynamics of the ν_{NO} in metalloproteins. Fe(II) and Fe(III) metalloproteins which bind nitric oxide are of great importance as both transporters and receptors of nitric oxide in biological systems. It has been noted by several researchers that the frequency of the ν_{NO} found in the active site is a sensitive reporter of the nature of the trans ligand and the environment of the distal pocket of the protein.[30] 2D IR studies utilizing the ν_{CO} as a vibrational probe have measured the functionally relevant dynamics in the active site of several heme proteins.[67-68] Molecular dynamics simulations have demonstrated that the experimentally measured timescales in the FFCF of the ν_{CO} in wild type and mutant myoglobin-CO are governed

by the dynamics of the distal histadine ligand, and protein-water interactions.[67, 69-71] 2D IR studies of the ν_{NO} in wild-type ferric myoglobin-NO and ferric cytochrome C-NO have measured vibrational dephasing timescales of 3.3 ps and 5.2 ps, respectively.[28-29] Our group has recently measured pH-dependent dephasing dynamics of the ν_{NO} in Nitrophorin-4 which is a pH-sensitive NO transporter protein.[72] Studying the binding ligand at the active site of metalloproteins instead of functionalized amino acids provides the distinct advantage of seeing the local protein environment without altering it. By measuring the FFCF of the ν_{NO} we can gain information about the role of the local environmental fluctuations at the active site on the overall protein activity. This study detailing the dephasing dynamics of the ν_{NO} in SNP dissolved in various polar solvents holds implications for measuring the polarity and the timescales for electric field fluctuations in the distal pocket of metalloproteins such as the Nitrophorins.

3.5 SUMMARY

We measure the vibrational dephasing dynamics of the ν_{NO} in SNP dissolved in a series of polar solvents. Our experiments reveal that the solvent polarity has a strong influence on the timescales of vibrational frequency fluctuations of the ν_{NO} in SNP varying from 0.8 ps in H_2O to 4.4 ps in DMSO. The timescales measured in our experiments are comparable to those measured for the vibrational dephasing of small charged ions in aqueous solutions. We find that the shorter timescales of spectral diffusion (τ_{c1}) are negatively correlated with empirical solvent parameters. The solvent-dependent frequency, dephasing dynamics, and anharmonicity of the ν_{NO} measured in this study suggests that both local and non-local fluctuating solvent environments around the nitrosyl and trans cyanide ligands drive the vibrational dephasing dynamics of the ν_{NO} in SNP. We believe that our study of solvation dynamics around SNP probed via the FFCF of the ν_{NO}

provides a foundation to better understand the local environment of nitric oxide binding sites in heme-NO metalloproteins and provides tests for molecular dynamics simulations of vibrational probes in polar solvents.

REFERENCES

1. Lee, H.; Lee, G.; Jeon, J.; Cho, M., Vibrational Spectroscopic Determination of Local Solvent Electric Field, Solute-Solvent Electrostatic Interaction Energy, and Their Fluctuation Amplitudes. *J. Phys. Chem. A* **2012,** *116* (Copyright (C) 2013 American Chemical Society (ACS). All Rights Reserved.), 347-357.

2. Ohta, K.; Tayama, J.; Saito, S.; Tominaga, K., Vibrational Frequency Fluctuation of Ions in Aqueous Solutions Studied by Three-Pulse Infrared Photon Echo Method. *Acc. Chem. Res.* **2012,** *45* (Copyright (C) 2012 American Chemical Society (ACS). All Rights Reserved.), 1982-1991.

3. Suydam, I. T.; Boxer, S. G., Vibrational Stark effects calibrate the sensitivity of vibrational probes for electric fields in proteins. *Biochemistry* **2003,** *42* (Copyright (C) 2013 American Chemical Society (ACS). All Rights Reserved.), 12050-12055.

4. Corcelli, S. A.; Lawrence, C. P.; Skinner, J. L., Combined electronic structure/molecular dynamics approach for ultrafast infrared spectroscopy of dilute HOD in liquid H2O and D2O. *Journal of Chemical Physics* **2004,** *120* (17), 8107-8117.

5. Eaves, J. D.; Tokmakoff, A.; Geissler, P. L., Electric field fluctuations drive vibrational dephasing in water. *Journal Of Physical Chemistry A* **2005,** *109* (42), 9424-9436.

6. Rey, R.; Hynes, J. T., Vibrational Phase and Energy relaxation of CN- in water. *J. Chem. Phys.* **1998,** *108*, 142.

7. Kim, Y. S.; Wang, J. P.; Hochstrasser, R. M., Two-dimensional infrared spectroscopy of the alanine dipeptide in aqueous solution. *Journal of Physical Chemistry B* **2005,** *109* (15), 7511-7521.

8. DeCamp, M. F.; DeFlores, L.; McCracken, J. M.; Tokmakoff, A.; Kwac, K.; Cho, M., Amide I vibrational dynamics of N-methylacetamide in polar solvents: The role of electrostatic interactions. *Journal of Physical Chemistry B* **2005,** *109* (21), 11016-11026.

9. Kwac, K.; Cho, M., Molecular dynamics simulation study of N-methylacetamide in water. I. Amide I mode frequency fluctuation. *J. Chem. Phys.* **2003,** *119* (Copyright (C) 2013 American Chemical Society (ACS). All Rights Reserved.), 2247-2255.

10. Schmidt, J. R.; Corcelli, S. A.; Skinner, J. L., Ultrafast vibrational spectroscopy of water and aqueous N-methylacetamide: comparison of different electronic structure/molecular dynamics approaches. *Journal of Chemical Physics* **2004,** *121* (18), 8887-8896.

11. Bakker, H. J.; Skinner, J. L., Vibrational Spectroscopy as a Probe of Structure and Dynamics in Liquid Water. *Chemical Reviews* **2009,** *110* (3), 1498-1517.

12. Asbury, J. B.; Steinel, T.; Stromberg, C.; Corcelli, S. A.; Lawrence, C. P.; Skinner, J. L.; Fayer, M. D., Water Dynamics: Vibrational Echo Correlation Spectroscopy and Comparison to Molecular Dynamics Simulations. *Journal of Physical Chemistry A* **2004,** *108* (7), 1107-1119.

13. Fecko, C. J.; Eaves, J. D.; Loparo, J. J.; Tokmakoff, A.; Geissler, P. L., Ultrafast hydrogen-bond dynamics in the infrared spectroscopy of water. *Science* **2003,** *301* (5640), 1698-1702.

14. Finkelstein, I. J.; Zheng, J. R.; Ishikawa, H.; Kim, S.; Kwak, K.; Fayer, M. D., Probing dynamics of complex molecular systems with ultrafast 2D IR vibrational echo spectroscopy. *Physical Chemistry Chemical Physics* **2007,** *9* (13), 1533-1549.

15. Jones, B. H.; Huber, C. J.; Massari, A. M., Solvation Dynamics of Vaska's Complex by 2D-IR Spectroscopy. *J. Phys. Chem. C* **2011,** *115* (Copyright (C) 2013 American Chemical Society (ACS). All Rights Reserved.), 24813-24822.

16. King, J. T.; Arthur, E. J.; Brooks, C. L.; Kubarych, K. J., Site-Specific Hydration Dynamics of Globular Proteins and the Role of Constrained Water in Solvent Exchange with Amphiphilic Cosolvents. *J. Phys. Chem. B* **2012,** *116* (Copyright (C) 2013 American Chemical Society (ACS). All Rights Reserved.), 5604-5611.

17. Bagchi, S.; Boxer, S. G.; Fayer, M. D., Ribonuclease S Dynamics Measured Using a Nitrile Label with 2D IR Vibrational Echo Spectroscopy. *J Phys Chem B* **2012,** *116* (Copyright (C) 2012 U.S. National Library of Medicine.), 4034-42.

18. Ohta, K.; Tayama, J.; Tominaga, K., Ultrafast vibrational dynamics of SCN- and N3- in polar solvents studied by nonlinear infrared spectroscopy. *Phys. Chem. Chem. Phys.* **2012,** *14* (Copyright (C) 2012 American Chemical Society (ACS). All Rights Reserved.), 10455-10465.

19. Oh, K.-I.; Choi, J.-H.; Lee, J.-H.; Han, J.-B.; Lee, H.; Cho, M., Nitrile and thiocyanate IR probes: molecular dynamics simulation studies. *The Journal of chemical physics* **2008,** *128*, 154504.

20. Li, S.; Schmidt, J. R.; Skinner, J. L., Vibrational energy relaxation of azide in water. *Journal of Chemical Physics* **2006,** *125* (24), 244507/1-244507/8.

21. Li, S.; Schmidt, J. R.; Corcelli, S. A.; Lawrence, C. P.; Skinner, J. L., Approaches for the calculation of vibrational frequencies in liquids: Comparison to benchmarks for azide/water clusters. *Journal of Chemical Physics* **2006,** *124* (20), 204110/1-204110/11.

22. Lim, M. H.; Hamm, P.; Hochstrasser, R. M., Protein fluctuations are sensed by stimulated infrared echoes of the vibrations of carbon monoxide and azide probes. *Proc. Natl. Acad Sci. USA* **1998,** *95*, 15315-15320.

23. Hamm, P.; Lim, M.; Hochstrasser, R. M., Non-Markovian dynamics of the vibrations of Ions in water from fs ir 3-pulse photon echoes. *Phys. Rev. Lett.* **1998,** *81*, 5326.

24. Bandaria, J. N.; Dutta, S.; Hill, S. E.; Kohen, A.; Cheatum, C. M., Fast Enzyme Dynamics at the Active Site of Formate Dehydrogenase. *J. Am. Chem. Soc.* **2008,** *130* (Copyright (C) 2012 American Chemical Society (ACS). All Rights Reserved.), 22-23.

25. Lindquist, B. A.; Furse, K. E.; Corcelli, S. A., Nitrile groups as vibrational probes of biomolecular structure and dynamics: an overview. *Physical chemistry chemical physics : PCCP* **2009,** *11* (37), 8119-8132.

26. Jansen, T. l. C.; Knoester, J., Waiting Time Dynamics in Two-Dimensional Infrared Spectroscopy. *Acc. Chem. Res.* **2009,** *42* (Copyright (C) 2013 American Chemical Society (ACS). All Rights Reserved.), 1405-1411.

27. Tayama, J.; Ohta, K.; Tominaga, K., Vibrational transition frequency fluctuation of the NO stretching mode of sodium nitroprusside in aqueous solutions. *Chem. Lett.* **2012,** *41* (Copyright (C) 2012 American Chemical Society (ACS). All Rights Reserved.), 366-368.

28. Hunt, N. T.; Greetham, G. M.; Towrie, M.; Parker, A. W.; Tucker, N. P., Relationship between protein structural fluctuations and rebinding dynamics in ferric haem nitrosyls. *Biochem. J.* **2011,** *433* (Copyright (C) 2012 American Chemical Society (ACS). All Rights Reserved.), 459-468.

29. Adamczyk, K.; Candelaresi, M.; Kania, R.; Robb, K.; Bellota-Anton, C.; Greetham, G. M.; Pollard, M. R.; Towrie, M.; Parker, A. W.; Hoskisson, P. A.; Tucker, N. P.; Hunt, N. T., The effect of point mutation on the equilibrium structural fluctuations of ferric Myoglobin. *Phys. Chem. Chem. Phys.* **2012,** *14* (Copyright (C) 2012 American Chemical Society (ACS). All Rights Reserved.), 7411-7419.

30. Spiro, T. G.; Soldatova, A. V.; Balakrishnan, G., CO, NO and O2 as vibrational probes of heme protein interactions. *Coordination Chemistry Reviews* **2013,** *257* (2), 511-527.

31. Soldatova, A. V.; Ibrahim, M.; Olson, J. S.; Czernuszewicz, R. S.; Spiro, T. G., New Light on NO Bonding in Fe(III) Heme Proteins from Resonance Raman Spectroscopy and DFT Modeling. *J. Am. Chem. Soc.* **2010,** *132* (13), 4614-4625.

32. Nienhaus, K.; Maes, E. M.; Weichsel, A.; Montfort, W. R.; Nienhaus, G. U., Structural Dynamics Controls Nitric Oxide Affinity in Nitrophorin 4. *J. Biol. Chem.* **2004,** *279* (38), 39401-39407.

33. Dalosto, S. D.; Vanderkooi, J. M.; Sharp, K. A., Vibrational Stark Effects on Carbonyl, Nitrile, and Nitrosyl Compounds Including Heme Ligands, CO, CN, and NO, Studied with Density Functional Theory. *J. Phys. Chem. B* **2004,** *108* (Copyright (C) 2013 American Chemical Society (ACS). All Rights Reserved.), 6450-6457.

34. Park, E. S.; Boxer, S. G., Origins of the sensitivity of molecular vibrations to electric fields: carbonyl and nitrosyl stretches in model compounds and proteins. *J. Phys. Chem. B* **2002,** *106* (Copyright (C) 2013 American Chemical Society (ACS). All Rights Reserved.), 5800-5806.

35. Manoharan, P. T.; Hamilton, W. C., The Crystal Structure of Sodium Nitroprusside. *Inorganic Chemistry* **1963,** *2* (5), 1043-1047.

36. Carducci, M. D.; Pressprich, M. R.; Coppens, P., Diffraction studies of photoexcited crystals: metastable nitrosyl-linkage isomers of sodium nitroprusside. *J. Am. Chem. Soc. FIELD Full Journal Title:Journal of the American Chemical Society* **1997,** *119* (11), 2669-2678.

37. Estrin, D. A.; Baraldo, L. M.; Slep, L. D.; Barja, B. C.; Olabe, J. A.; Paglieri, L.; Corongiu, G., Theoretical and Experimental Study of Medium Effects on the Structure and Spectroscopy of the [Fe(CN) 5NO] 2-Ion. *Inorg. Chem.* **1996,** *35* (13), 3897-3903.

38. Sando, G. M.; Zhong, Q.; Owrutsky, J. C., Vibrational and rotational dynamics of cyanoferrates in solution. *Journal of Chemical Physics* **2004,** *121* (5), 2158-2168.

39. Gutlich, P.; Garcia, Y.; Woike, T., Photoswitchable coordination compounds. *Coordination Chemistry Reviews* **2001,** *219-221*, 839-879.

40. Schaniel, D.; Woike, T., Necessary conditions for the photogeneration of nitrosyl linkage isomers. *Phys. Chem. Chem. Phys. FIELD Full Journal Title:Physical Chemistry Chemical Physics* **2009,** *11* (21), 4391-4395.

41. Coppens, P.; Novozhilova, I.; Kovalevsky, A., Photoinduced linkage isomers of transition metal nitrosyl compounds and related complexes. *Chem. Rev. (Washington, D. C.)* **2002,** *102* (4), 861-883.

42. Lynch, M. S.; Cheng, M.; Van Kuiken, B. E.; Khalil, M., Probing the Photoinduced Metal-Nitrosyl Linkage Isomerism of Sodium Nitroprusside in Solution Using Transient Infrared Spectroscopy. *J. Am. Chem. Soc.* **2011,** *133* (14), 5255-5262.

43. Khalil, M.; Demirdöven, N.; Tokmakoff, A., Coherent 2D IR spectroscopy: molecular structure and dynamics in solution. *J. Phys. Chem. A* **2003,** *107* (27), 5258-5279.

44. Lynch, M. S.; Slenkamp, K. M.; Cheng, M.; Khalil, M., Coherent Fifth-Order Visible–Infrared Spectroscopies: Ultrafast Nonequilibrium Vibrational Dynamics in Solution. *The Journal of Physical Chemistry A* **2012,** *116* (26), 7023-7032.

45. Sung, J.; Silbey, R. J., Four-wave mixing spectroscopy for a multi-level system. *J. Chem. Phys.* **2001,** *115*, 9266-9287.

46. Mukamel, S., *Principles of Nonlinear Optical Spectroscopy*. Oxford University Press: New York, 1995.

47. Khalil, M.; Tokmakoff, A., Signatures of vibrational interactions in coherent two-dimensional infrared spectroscopy. *Chem. Phys.* **2001,** *266* (2-3), 213-230.

48. Fourkas, J. T.; Kawashima, H.; Nelson, K. A., Theory of Nonlinear Optical Expts with Harmonic Oscillators. *J. Chem. Phys* **1995,** *103* (11), 4393-4407.

49. Reichardt, C., Solvatochromic dyes as solvent polarity indicators. *Chem. Rev* **1994,** *94* (8), 2319-2358.

50. Tanida, H.; Watanabe, I., Photoelectron emission spectroscopy applied to bromide ion in solvents. *Journal of Molecular Liquids* **1995,** *65–66* (0), 409-412.

51. CRC Handbook of Chemistry and Physics, 93rd Edition (Internet Version 2013). Haynes, W. M., Ed. CRC Press/Taylor and Francis: Boca Raton, FL.

52. Marcus, Y., The properties of organic liquids that are relevant to their use as solvating solvents. *Chem. Soc. Rev.* **1993,** *22* (6), 409-416.

53. Gutmann, V., Empirical parameters for donor and acceptor properties of solvents. *Electrochim. Acta* **1976,** *21* (Copyright (C) 2013 American Chemical Society (ACS). All Rights Reserved.), 661-70.

54. Kamlet, M. J.; Taft, R., The solvatochromic comparison method. I. The. beta.-scale of solvent hydrogen-bond acceptor (HBA) basicities. *Journal of the American Chemical Society* **1976,** *98* (2), 377-383.

55. Taft, R.; Kamlet, M. J., The solvatochromic comparison method. 2. The. alpha.-scale of solvent hydrogen-bond donor (HBD) acidities. *Journal of the American Chemical Society* **1976,** *98* (10), 2886-2894.

56. Mayer, U.; Gutmann, V.; Gerger, W., Acceptor number. Quantitative empirical parameter for the electrophilic properties of solvents. *Monatsh. Chem.* **1975,** *106* (Copyright (C) 2013 American Chemical Society (ACS). All Rights Reserved.), 1235-57.

57. Huber, C. J.; Anglin, T. C.; Jones, B. H.; Muthu, N.; Cramer, C. J.; Massari, A. M., Vibrational Solvatochromism in Vaska's Complex Adducts. *J. Phys. Chem. A* **2012,** *116* (Copyright (C) 2013 American Chemical Society (ACS). All Rights Reserved.), 9279-9286.

58. Bixby, T. J.; Patterson, J. D.; Reid, P. J., Femtosecond TRIR Studies of ClNO Photochemistry in Solution: Evidence for Photoisomerization and Geminate Recombination†. *The Journal of Physical Chemistry A* **2009,** *113* (16), 3886-3894.

59. Tayama, J.; Ishihara, A.; Banno, M.; Ohta, K.; Saito, S.; Tominaga, K., Temperature dependence of vibrational frequency fluctuation of N3- in D2O. *J. Chem. Phys.* **2010,** *133* (Copyright (C) 2013 American Chemical Society (ACS). All Rights Reserved.), 014505/1-014505/11.

60. Tayama, J.; Banno, M.; Ohta, K.; Tominaga, K., Vibrational dynamics of the CN stretching mode of [Ru(CN)6]4- in D2O studied by nonlinear infrared spectroscopy. *Sci. China: Phys., Mech. Astron.* **2010,** *53* (Copyright (C) 2013 American Chemical Society (ACS). All Rights Reserved.), 1013-1019.

61. Ohta, K.; Maekawa, H.; Tominaga, K., Vibrational population relaxation and dephasing dynamics of Fe(CN)64- in water: deuterium isotope effect of solvents. *Chem. Phys. Lett.* **2004,** *386* (Copyright (C) 2013 American Chemical Society (ACS). All Rights Reserved.), 32-37.

62. Ohta, K.; Maekawa, H.; Saito, S.; Tominaga, K., Probing the Spectral Diffusion of Vibrational Transitions of OCN- and SCN- in Methanol by Three-Pulse Infrared Photon Echo Spectroscopy. *J. Phys. Chem. A* **2003,** *107* (Copyright (C) 2013 American Chemical Society (ACS). All Rights Reserved.), 5643-5649.

63. Fecko, C. J.; Loparo, J. J.; Roberts, S. T.; Tokmakoff, A., Local hydrogen bonding dynamics and collective reorganization in water: Ultrafast infrared spectroscopy of HOD/D2O. *Journal of Chemical Physics* **2005,** *122* (5).

64. Asbury, J. B.; Steinel, T.; Kwak, K.; Corcelli, S. A.; Lawrence, C. P.; Skinner, J. L.; Fayer, M. D., Dynamics of water probed with vibrational echo correlation spectroscopy. *Journal of Chemical Physics* **2004,** *121* (24), 12431-12446.

65. Li, S.; Schmidt, J. R.; Piryatinski, A.; Lawrence, C. P.; Skinner, J. L., Vibrational Spectral Diffusion of Azide in Water. *Journal of Physical Chemistry B* **2006,** *110* (38), 18933-18938.

66. Ferrario, M.; Klein, M. L.; McDonald, I. R., Dynamic behavior of the azide ion in protic solvents. *Chem. Phys. Lett.* **1993,** *213* (Copyright (C) 2013 American Chemical Society (ACS). All Rights Reserved.), 537-40.

67. Bagchi, S.; Nebgen, B. T.; Loring, R. F.; Fayer, M. D., Dynamics of a myoglobin mutant enzyme: 2D IR vibrational echo experiments and simulations. *J Am Chem Soc* **2010,** *132* (Copyright (C) 2012 U.S. National Library of Medicine.), 18367-76.

68. Merchant, K. A.; Thompson, D. E.; Xu, Q.-H.; Williams, R. B.; Loring, R. F.; Fayer, M. D., Myoglobin-CO Conformational Substate Dynamics: 2D Vibrational Echoes and MD Simulations. *Biophys. J* **2002,** *82* (6), 3277-3288.

69. Massari, A. M.; Finkelstein, I. J.; McClain, B. L.; Goj, A.; Wen, X.; Bren, K. L.; Loring, R. F.; Fayer, M. D., The influence of aqueous versus glassy solvents on protein dynamics: Vibrational echo experiments and molecular dynamics simulations. *Journal of the American Chemical Society* **2005,** *127* (41), 14279-14289.

70. Merchant, K. A.; Noid, W. G.; Akiyama, R.; Finkelstein, I. J.; Goun, A.; McClain, B. L.; Loring, R. F.; Fayer, M. D., Myoglobin-CO Substate Structures and Dynamics: Multidimensional Vibrational Echoes and Molecular Dynamics Simulations. *J. Am. Chem. Soc.* **2003,** *125* (45), 13804-1381.

71. Williams, R. B.; Loring, R. F.; Fayer, M. D., Vibrational Dephasing of Carbonmonoxy Myoglobin. *J. Phys. Chem. B.* **2001,** *105* (19), 4068-4071.

72. Cheng, M.; Brookes, J. F.; Montfort, W. R.; Khalil, M., Using 2D IR spectroscopy to Characterize the pH-Dependent Structural Dynamics in Nitrophorins. *J Am Chem Soc* **2012**, in revision

CHAPTER 4

THE pH-DEPENDENT PICOSECOND STRUCTURAL DYNAMICS IN THE DISTAL POCKET OF NITROPHORIN 4 INVESTIGATED BY 2D IR SPECTROSCOPY

The work presented in this chapter has been previously published in

Cheng, M.*; Brookes, J. F.*; Montfort, W. R.; Khalil, M. pH Dependent Picosecond Structural Dynamics in the Distal Pocket of Nitrophorin 4 Investigated by 2D IR Spectroscopy. *J. Phys. Chem. B* 2013, 117, 15804−15811.
**Equal contribution*

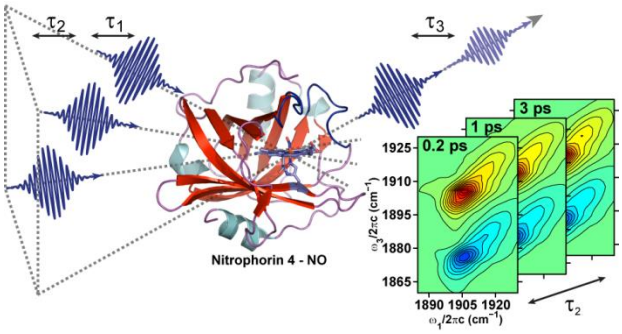

Nitrophorin 4 (NP4) belongs to a family of pH-sensitive, nitric oxide (NO) transporter proteins which undergo a large structural change from a closed to an open conformation at high pH to allow for NO delivery. Measuring the pH-dependent structural dynamics in NP4–NO around the ligand binding site is crucial for developing a mechanistic understanding of NO binding and release. In this study we use coherent two-dimensional infrared (2D IR) spectroscopy to measure picosecond structural dynamics sampled by the nitrosyl stretch in NP4–NO as a function of pH at room temperature. Our results show that both the closed and open conformers of the protein are present at low (pD 5.1) and high (pD 7.9) pH conditions. The closed and open conformers are characterized by two frequencies of the nitrosyl stretching vibration labeled A_0 and A_1, respectively. Analysis of the 2D IR lineshapes reveals that at pD 5.1, the closed

conformer experiences structural fluctuations arising from solvation dynamics on a ~3 ps timescale. At pD 7.9, both the open and closed conformers exhibit fluctuations on a ~1 ps timescale. At both pD conditions, the closed conformers maintain a static distribution of structures within the experimental time window of 100 ps. This is in contrast to the open conformer, which is able to interconvert among its sub-states on a ~100 ps timescale. Our results directly measure the timescales of solvation dynamics in the distal pocket, the flexibility of the open conformation at high pH, and the rigidity of the closed conformers at both pH conditions. We discuss how the pH dependent equilibrium structural fluctuations of the nitrosyl ligand measured in this study are related to the uptake and delivery of nitric oxide in Nitrophorin 4.

4.1 INTRODUCTION

Nitrophorins (NPs) are a particular class of nitrosyl binding heme proteins found naturally in the saliva of blood feeding insects. In these proteins, NO is stored in the low pH environment of the salivary gland (pH ~5) and is released in the higher pH environment of the host tissue (pH ~7.5) to induce vasodilation and prevent blood coagulation.[1-2] Nitric oxide is a reactive messenger molecule implicated in regulating the immune, nervous and cardiovascular systems of mammals.[3] Given the importance of NO in biology, the NPs serve as excellent models to probe the interplay of structure, dynamics and function for a naturally occurring NO delivery system. Nitrophorin 4 is a widely studied protein of the Nitrophorin family. Figure 4.1 shows a high-resolution crystal structure of the NP4-NO protein acquired at pH 5.6. The protein structure consists of an eight-stranded antiparallel β-barrel with a heme buried at one end. The protein is known to undergo a conformational change upon binding to NO, such that the A-B (residues 31-37) and the G-H (residues 125-132) loops pack tightly together to form a hydrophobic pocket preventing NO escape.[4-6] Crystal structures of NP4 reveal a distal pocket

with structurally distinct closed and open conformations.[6] The closed conformation is characterized by a dynamic hydrophobic cavity with a network of hydrogen bonds between the residues of the A-B and G-H loops. The hydrogen bond network is disrupted in the open conformation resulting in a more hydrophilic cavity with the presence of water molecules and flexible loop regions. The two conformations are found to exist at all pH conditions by X-ray crystallography, with the fraction of the open conformation increasing at higher pH.[6]

Kinetic studies of the binding and dissociation of NO using histamine displacement and laser photolysis have revealed multi-exponential pH-dependent NO release rates across a wide range of timescales.[7-10] The pH dependence of the NO release is completely eliminated for the double mutant D129A/L130A confirming that the conformational flexibility of the loop regions is responsible for the pH-dependent NO release in NP4.[7] However, the cause for the non-exponential NO release rates remains an open question. There have been several molecular dynamics simulations on the NO release dynamics of NP4.[11-15] These simulations have revealed the importance of the flexibility of the loop regions, the protonation state of Asp 30 and the equilibrium of the closed and open conformers to the pH dependent NO release mechanism in the NP4 protein.

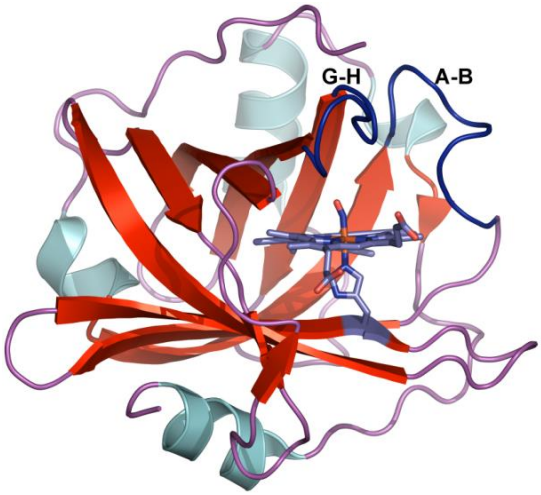

Figure 4.1 Cartoon showing the NP4-NO protein at pH 5.6 (PDB ID: 1X8O). The positions of the loops A-B and G-H are highlighted in dark blue.

While the structural flexibility of the A-B and G-H loops and the polarity of the distal pocket have been extensively discussed in experimental and theoretical studies of NP4-NO, there have been no measurements of the timescales of equilibrium structural fluctuations of the nitrosyl ligand. The time-dependent frequency fluctuations ($\delta\omega(t)$) of an IR active vibration (ω_0) are encoded in the frequency-frequency correlation function (FFCF, $\langle \delta\omega(t)\delta\omega(0)\rangle$). Two-dimensional (2D) IR spectroscopy has been used effectively to measure the FFCF of carbonyl and nitrosyl ligands in heme proteins to characterize the structural fluctuations around the ligand binding sites.[16-24] There is a growing body of literature on how the frequency shifts of the nitrosyl stretching vibration (ν_{NO}) in heme proteins are a sensitive reporter of the local electric field and Fe-NO bonding interactions.[25-27]. The goal of this study is to measure the equilibrium structural dynamics in the distal pocket of NP4–NO as a function of pH using 2D IR spectroscopy to measure the FFCF of the ν_{NO}. Our experiments sample the conformational heterogeneity and directly measure the timescales of equilibrium structural fluctuations in the

vicinity of the Fe–NO bond. We discuss how the spectroscopic data reveal a dynamic distal pocket environment that is crucial for the binding, release and regulation of NO in NP4.

4.2 EXPERIMENTAL METHODS

4.2.1 Sample preparation. Nitrophorin 4 was overexpressed from an *Escherichia coli* strain and refolded from inclusion bodies supplemented with heme, as described previously.[4] In order to resolve the weak mid-IR absorption band of the NO stretching vibration at ~1905 cm^{-1} from the absorbance of H_2O in the same spectral region, samples of purified ferric NP4 underwent a buffer exchange process to replace the 20 mM sodium phosphate buffer (at pH 7.0) with a deuterated buffer. Acidic (pD 5.1) and basic (pD 7.9) 20 mM potassium dideuterium phosphate (KD_2PO_4) buffer solutions were prepared in D_2O. Centrifugal filter devices (Amicon Ultra-0.5) were used to exchange the aqueous buffer as well as to concentrate the protein samples. In order to prepare the ferric NP4−NO complex, fresh NO gas was generated by mixing ascorbic acid (880 mg in 25 mL of water) and sodium nitrite (40-60 mg) after degassing each of them under Ar for at least 30 minutes. The sample was also degassed for at least 15 minutes prior to flushing with the generated NO gas using an airtight syringe. Linear FTIR (Jasco FT/IR-4100) and UV-Vis (Jasco V-630) spectra of the samples were obtained (sample path length = 50 μm) before and after each 2D IR scan to ensure that the protein had not degraded during the experiment. The final concentrations of the protein sample at the start of each scan were determined by the intensity of the alpha and beta bands in the UV-Vis spectra of ferric NP4-NO.[28] The final concentrations were 6.4 mM and 4.1 mM for the acidic and basic samples, respectively. These concentrations yield an OD of 0.046 and 0.037 for the ν_{NO} peak at 1905 cm^{-1}.

4.2.2 2D IR Experiment. Femtosecond pulses of mid-IR light were generated from a combination of commercial equipment, beginning with a regenerative amplifier (Spectra Physics

Spitfire Pro-35F-XP), which outputs 3 W, 800 nm, 35 fs pulses of light at 1 kHz. Approximately 1 W of the 800 nm output is sent to an optical parametric amplifier (OPA-800C) to produce the near-IR signal and idler pulses. The two near IR fields undergo difference frequency mixing in a 0.5 mm $AgGaS_2$ crystal to generate 80 fs mid-IR pulses with a spectral bandwidth of ~200 cm^{-1} at a center wavelength of 5.1 μm.

The mid-IR pulse is sent into a five-beam interferometer to generate three input pulses, a tracer beam and a local oscillator field as described previously.[29-30] The three input IR beams have parallel polarizations and are arranged in a "boxcar" geometry, temporally overlapped, and focused onto the sample with a spot-size of ~150 μm. Each of the input beams has 0.2 μJ of energy per pulse. The home-built sample cell is equipped with two 1 mm CaF_2 windows and a 50 μm Teflon spacer. The resulting background-free signal field is overlapped with the local oscillator field on a beamsplitter for heterodyne detection. The reflected and transmitted combined signal and local oscillator fields are π out of phase with respect to each other and are detected at the focal plane of a spectrometer (Triax 190, Horiba Jobin Yvon, 150 1ines/mm grating) using a 2 × 64 mercury cadmium telluride (MCT) array detector (IR0144, Infrared Systems Development). We subtract signals from the two linear MCT arrays to perform "balanced detection" on a shot-to-shot basis as explained in Ref. 30.

The evolution (τ_1) and waiting (τ_2) time delays between the consecutive pairs of pulses 1,2 and 2,3 are accurately controlled by Newport XMS50 linear stages. Rephasing and non-rephasing experiments were performed at each τ_2 delay in order to construct absorptive 2D IR correlation spectra. The τ_1 delay was scanned in 4 fs steps from 0 to 4(3) ps for the rephasing (non-rephasing) experiments. The τ_2 delay was scanned in unequal time steps from 0 to 70 ps in unequal time steps with each data point representing 2000 laser shots. The raw experimental data

was zero padded to 32.8 ps and Fourier transformed along τ_1 to obtain the ω_1 axis. The final 2D IR spectrum is corrected for the phase ambiguities corresponding to drift of the relative timing between the local oscillator and signal fields by comparing the projection of the 2D IR spectrum along the ω_1 axis to a two-beam dispersed pump-probe spectrum collected for the same values of τ_2.[31]

4.2.3 2D IR spectral fitting. The experimental 2D IR spectra were fit by iteratively calculating the third-order nonlinear signal field as a function of τ_1 and τ_3 in the time domain and then Fourier transforming it to obtain theoretical spectra as described previously.[29] 2D IR spectra of NP4 under both pH conditions were simulated using a six-level system for two non-interacting NP4-NO populations, each with a ground, first-excited and second-excited vibrational state (0, 1, 2) using the nonlinear response formalism detailed previously.[32-33] In our system, there are a total of 12 response functions for the rephasing and non-rephasing signals. We ignore any cross correlation terms between the two non-interacting NP4-NO populations since the experiment does not reveal the presence of any cross-peaks. We assume a separation of timescales for the vibrational and rotational dynamics for calculating the third-order nonlinear response functions. The goal of the spectral fitting procedure is to extract parameters of the FFCF of the ν_{NO} in NP4-NO as a function of pH. We modeled the 2D lineshapes using the following form for the FFCF:

$$C_{11}(t) = \sum_{n=1}^{2} \Delta_n^2 \exp\left(-\frac{t}{\tau_{cn}}\right) + \frac{\delta(t)}{T_2^*} \qquad (4.1)$$

In the above expression, Δ_n and τ_{cn} describe the amplitude and timescales of the frequency fluctuations in the Kubo model, $\delta(t)$ is the Dirac delta function and T_2^* represents the timescales of fast dynamics determining the homogenous linewidth of the ν_{NO} in NP4-NO. Analytical expressions for the nonlinear dephasing functions in terms of the correlation functions are

obtained using the methodology described in Ref. 33. The contribution of the rotational correlation functions to the 2D IR lineshape was not included because of the long time scales associated with orientational rearrangement of the protein. We accounted for the effects of vibrational population relaxation by introducing exponential relaxation rates into the vibrational response functions during all three time periods using harmonic scaling rules. For example, if the vibrational lifetime for the first excited state of ν_{NO} is T_1, then the vibrational lifetime of the second excited state is $1/2T_1$. The vibrational lifetime of the first excited state of ν_{NO} for both the sub-populations of NP4-NO was determined to be 30 ps using IR pump-probe experiments. Harmonic scaling was used for the energy gap fluctuations in our two separate 3-level systems to relate the FFCFs of the first (1) and second (2) vibrational states of our three level system, such that: $C_{22}(t) = 2C_{21}(t) = 2C_{12}(t) = 4C_{11}(t)$. For each pH condition, the experimental 2D IR spectra for all τ_2 points were fit simultaneously by floating the parameters in the FFCFs, the vibrational anharmonicity ($\Delta_{12} = 2\nu_{NO}^{1\leftarrow 0} - \nu_{NO}^{2\leftarrow 0}$), and the transition dipole moment between the first and second excited states ($|\mu_{12}|$) for each of the sub-populations of NP4-NO. The best-fit values are listed in Table 4.2. The simulated and experimental spectra were fit using a nonlinear least squares fitting routine written in MATLAB.

4.3 RESULTS and DISCUSSION

4.3.1 pH-Dependent FTIR Spectra and conformational sub-states of NP4-NO

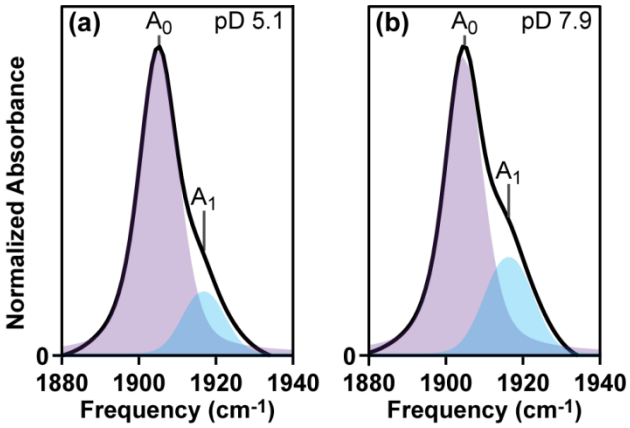

Figure 4.2 pH-dependent FTIR spectra of NP4-NO. The shaded areas represent the fits of the two peaks using a Voigt lineshape.

The FTIR spectrum of NP4–NO in the ν_{NO} region is shown in Figure 4.2 as a function of pH. The spectra show two peaks in the ν_{NO} region centered at ~1905 and ~1917 cm^{-1}. We see that the peak at 1917 cm^{-1} increases in amplitude under higher pH conditions. The shaded areas represent fits to the two peaks using Voigt lineshapes and the best-fit parameters are listed in Table 4.1. The two peaks in the ν_{NO} region indicate the presence of two conformational sub-states of the NP4-NO protein which exist under acidic and basic pH conditions. Previous FTIR and Raman studies of NP4-NO have assigned the peak centered at ~1905 cm^{-1} to the closed conformation where the NO ligand is in a hydrophobic environment and the peak at ~1917 cm^{-1} to the open conformation with a hydrophilic distal pocket.[8, 25, 34] The shift of the ν_{NO} vibration to higher frequencies in more hydrophilic/polar environments is also seen in other Fe–NO complexes like sodium nitroprusside.[29, 35] In this work, we label the peak at ~1905 cm^{-1} as A_0

and the peak at ~1917 cm^{-1} as A_1. The labeling scheme follows from the FTIR spectroscopy of ferric myoglobin-NO ($Mb^{III}NO$) under various pH conditions.[36-37]

Table 4.1 Spectral characteristics of the ν_{NO} region in NP4-NO. The error bars correspond to a 95% confidence interval.

Peak	Sample pD	ν_{NO} (cm^{-1})	$\Delta\nu_{FWHM}$ (cm^{-1})
A_0	5.1	1904.9±0.2	11.7±0.4
A_1	5.1	1917±1	14±2
A_0	7.9	1904.3±0.2	12.1±0.4
A_1	7.9	1916±1	12±1

High-resolution crystal structures of NP4-NO at pH 5.6 and 7.5 have revealed the presence of at least two major conformers and considerable loop disorder at higher pH.[6] Figures 4.3(a-b) display the distal pocket configuration for the closed and open conformational sub-states of NP4-NO at pH 5.6. We see that in the closed conformation the hydrogen bonding interaction between the residues of the A-B and G-H loops is preserved, the non-polar residues are packed into the binding pocket providing favorable non-polar interactions with the NO ligand. In contrast, the open conformation shows that Leu 130 has moved away from the distal pocket, providing room for several solvent molecules. The position of the electron density of Leu 130 in the open conformer matches closely with the NP4-NH_3 crystal structure at pH 7.4, which shows the presence of several (~5) water molecules in the distal pocket.[6] In the refined crystal structure of NP4-NO at pH 5.6, the open conformer was found to have an occupancy of 0.29. Based on the

crystal structures and the pH-dependent FTIR spectra, we assign the A_0 and A_1 peaks in Figure 4.2a to the closed and open conformational sub-states of NP4-NO at pH 5.6.

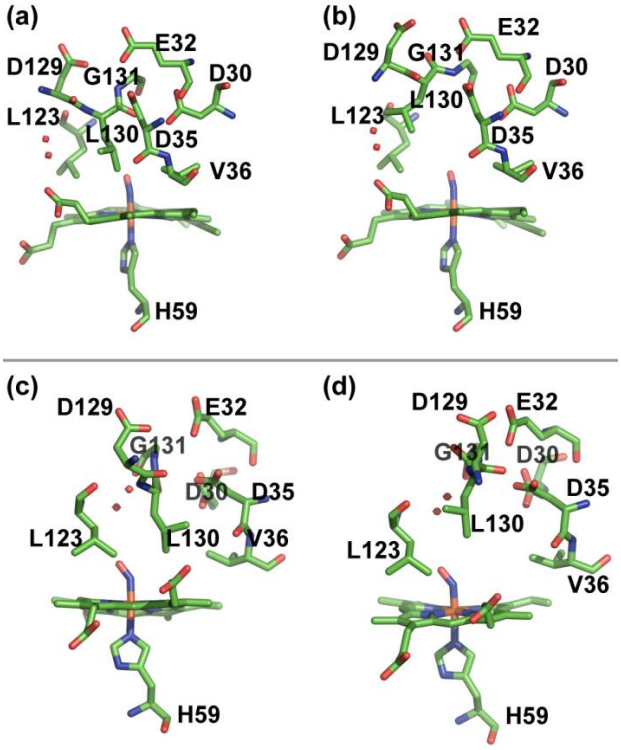

Figure 4.3 Multiple conformers of NP4-NO determined by X-ray crystallography. The top panel shows the closed (3a) and open (3b) conformers at pH 5.6 (PDB ID 1X8O). The bottom panel shows the closed (3c) and open (3d) conformers at pH 7.5 (PDB ID 1X8N).

The closed and open conformers of the high resolution crystal structure of NP4-NO at pH 7.5 are shown in Figures 4.3c-d. The x-ray study has noted the difficulty in modeling loops A-B and G-H because of considerable disorder. The structural distinction between the closed and open conformers is seen in the residues 129-131. Leucine 130 flips its position between the closed and open conformational sub-states in a manner similar to the crystal structure obtained at pH 5.6. Water molecules are seen in the distal pocket within ~3.8 Å of the nitrosyl ligand in the

crystal structure at higher pH. Given that the frequencies of the ν_{NO} peaks are very similar at both pH conditions, we assign the A_0 and A_1 peaks in Figure 4.2b to the closed and open conformational sub-states of NP4-NO at pH 7.5.

The ν_{NO} peak assignments described above agree with the studies on ferric Mb-NO and DFT calculations.[25, 36-37] In wild type $Mb^{III}NO$ at room temperature, a major peak at ~1927 cm^{-1} and a weak feature at ~1902 cm^{-1} are observed in the ν_{NO} region at neutral pH.[38] The mutant, H64L, of $Mb^{III}NO$ shows a single peak at 1904 cm^{-1}. The negative polar interaction of the nitrosyl ligand with a tautomeric form of the distal histidine has been proposed for the protein conformer giving rise to the peak at 1927 cm^{-1} in wild type $Mb^{III}NO$.[37] The absence of this interaction in the H64L mutant, results in the downshift of the ν_{NO} frequency to 1904 cm^{-1}, which is very similar to the frequency of the A_0 peak in NP4-NO. The DFT calculations have shown how the frequency of the ν_{NO} in ferric heme proteins reports on the polarity of the heme protein and interactions of the NO moiety with nearby Lewis base donors.[25] The same DFT study has assigned an increase in frequency of the ν_{NO} in open conformer of NP4-NO to lone pair interactions of the NO with a water molecule.

The fits of peaks in the ν_{NO} region reveal that the fraction of the A_1 peak is 16% and 26% at pD 5.1 and 7.9 respectively. Previous FTIR studies of NP4-NO had measured a ratio of 0.2 at cryogenic temperatures for NP4-NO at pH 7.5.[8] The linewidths of the peaks in the FTIR spectra range from 12-14 cm^{-1} and are governed by the frequency-frequency correlation function (FFCF) of the ν_{NO} vibration, which measures the timescales of structural dynamics around the NO binding site for the open and closed conformations. Using 2D IR lineshape analysis we can measure the timescales of frequency fluctuations, which dictate the linewidth of the ν_{NO} in NP4-NO as a function of pH.

4.3.2 pH-dependent 2D IR spectra and extraction of the FFCF parameters

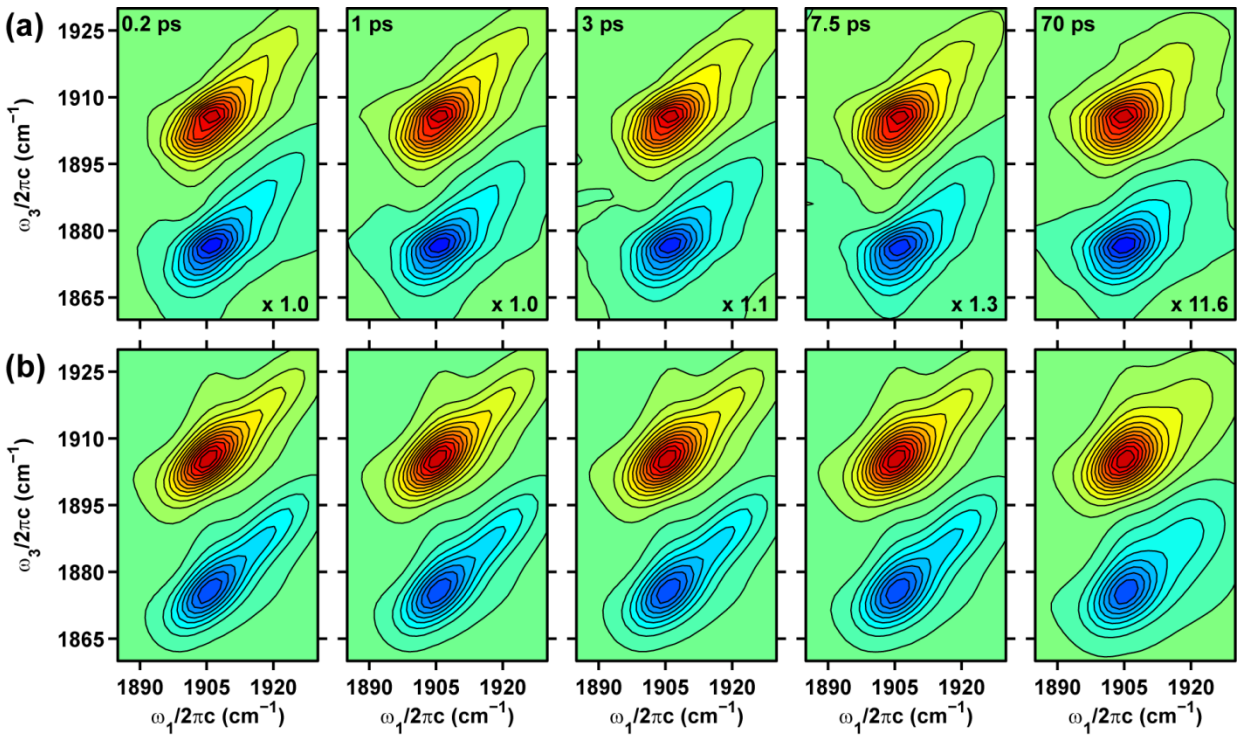

Figure 4.4 (a) Experimental 2D IR spectra of the ν_{NO} in NP4-NO at pD 5.1. (b) Best fits to the experimental 2D IR spectra. Contour levels are drawn at 5% intervals. The τ_2 values and the normalization factors for each 2D plot are given in the top left and bottom right corners, respectively.

The top panel of Figure 4.4 displays a series of experimental 2D IR spectra of the ν_{NO} in NP4–NO plotted as a function of τ_2 at pD 5.1. In each of the spectra, the positive diagonal peaks correspond to vibrational transitions between the ground and first excited state of the ν_{NO} ($\nu_{NO}^{0\rightarrow1}$). The off-diagonal negative peaks involve transitions between the first and second excited states of

the ν_{NO} ($\nu_{NO}^{1\rightarrow2}$). The separation of the two peaks in the ω_3 dimension of the 2D IR plots is a direct measure of the vibrational anharmonicity of the ν_{NO} in NP4–NO. Focusing on the strong positive 2D peaks in Figure 4.4a, we note that they are elongated along the diagonal axes at τ_2=0.2 ps representing a distribution of structures for the closed (A_0) and open (A_1) conformations of NP4-NO at low pH. As τ_2 increases, structural fluctuations cause the vibrational frequencies to lose correlation and results in the 2D lineshapes becoming more symmetric. It is important to note that the A_0 peak remains elongated along the diagonal even at τ_2 = 70 ps. A qualitative comparison between the A_0 and A_1 peaks at τ_2 = 70 ps suggests that the latter peak undergoes faster frequency fluctuations. The evolving 2D lineshape is a direct measure of the FFCF and provides information on the amplitude and timescales of the structural fluctuations in the open and closed conformations of NP4–NO.

We fit the 2D IR spectra to extract the parameters of the FFCF as described in the Methods section. In this paper we focus our efforts on understanding the 2D IR lineshape of the fundamental transition of the ν_{NO} in NP4–NO. The bottom panel in Figure 4.4 displays the 2D IR spectra resulting from the best fits of the experimental spectra assuming the form of the correlation functions given by Equation 1. The resulting parameters of the FFCF are listed in Table 4.2. We find that the homogenous dephasing time (T_2^*) for the A_0 and A_1 peaks of the ν_{NO} in NP4-NO at pD 5.1 is 7 ps. While the homogenous contribution to the spectral linewidth is similar for the A_0 and A_1 peaks, the timescales for structural diffusion (τ_{c1} and τ_{c2}) are very different. The ν_{NO} of the closed conformer exhibits fast structural fluctuations on a 3 ps timescale (τ_{c1}). Significant portions of the dynamics are too slow to be measured on our experimental timescale of ~100 ps. This is represented as τ_{c2}=∞ in Table 4.2. The ν_{NO} of the open conformer

exhibits structural fluctuations on a 0.9 ps and a 130 ps timescale. The ratio of the amplitudes of the structural fluctuations (Δ_2/Δ_1) is 1 and 3.5 for the A_0 and A_1 peaks.

Table 4.2 Best fit parameters of the FFCF for the ν_{NO} in NP4-NO extracted from fitting the 2D IR data.

	Δ_1 (ps^{-1})	τ_{c1} (ps)	Δ_2 (ps^{-1})	τ_{c2} (ps)	T_2^* (ps)	Δ_{12} (cm^{-1})
pD 5.1						
A_0	0.55±0.04	3±1	0.57±0.05	∞	7±2	30±2
A_1	0.40±0.06	0.9±0.4	1.4±0.1	130±30	7±2	29±2
pD 7.9						
A_0	0.3±0.1	1.4±0.7	0.36±0.04	∞	7±2	30±2
A_1	0.57±0.07	0.8±0.4	1.2±0.1	70±30	7±2	29±2

Figure 4.5 shows the experimental and best fit 2D IR spectra for the ν_{NO} in NP4-NO obtained at pD 7.9. At τ_2=0.2 ps, the A_0 and A_1 peaks are elongated along the diagonal indicating the presence of structural inhomogeneity in the two conformational sub-states. Similar to the 2D IR data taken at pD 5.1, the A_1 peak loses its frequency correlation faster than the A_0 peak as evidenced by their different 2D lineshapes at τ_2=25 ps. Our best fits to the 2D IR data (see Table 2) find that the vibrational anharmonicity is pH independent and is ~30 cm^{-1} for peaks A_0 and A_1 peaks. The ν_{NO} of the closed conformer exhibits fast structural fluctuations on a 1.4 ps timescale (τ_{c1}) and on timescales longer than our experimental time window of ~100 ps. This is represented

as $\tau_{c2}=\infty$ in Table 4.2. The ν_{NO} of the open conformer exhibits structural fluctuations on a 0.8 ps and a 70 ps timescale. The ratio of the amplitudes of the structural fluctuations (Δ_2/Δ_1) is 1 and 2 for the A_0 and A_1 peaks.

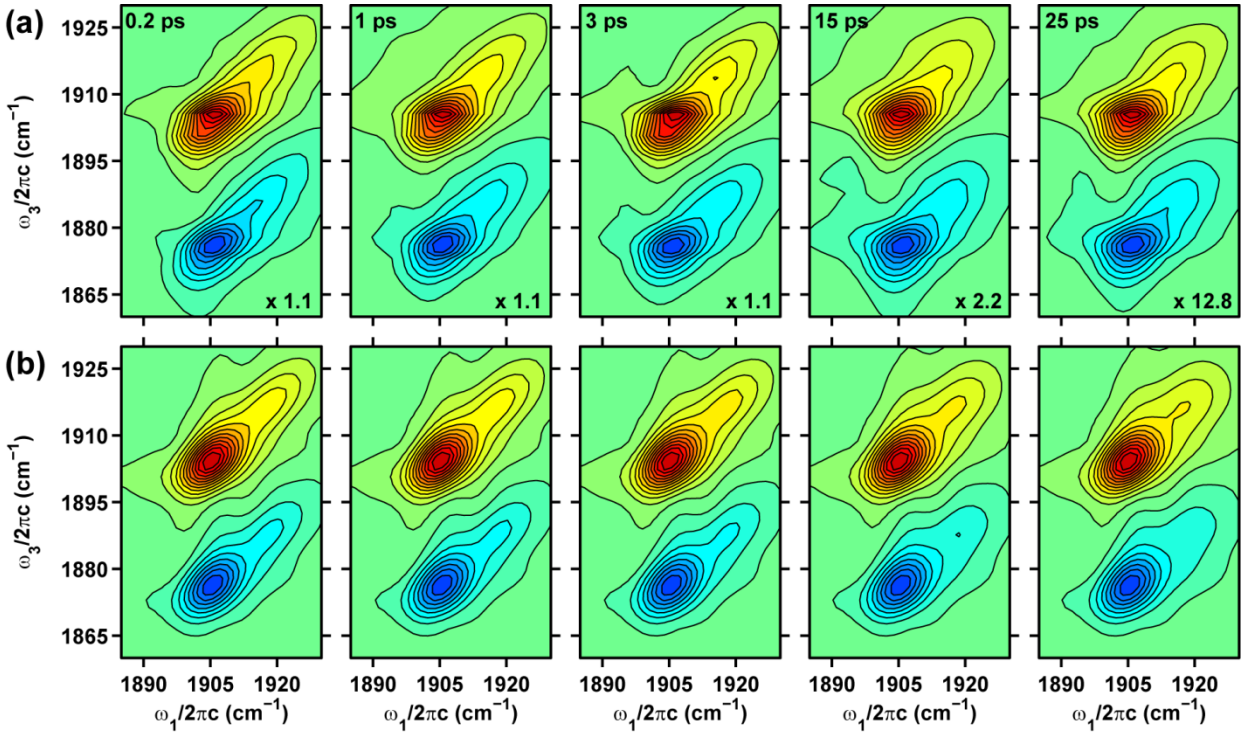

Figure 4.5 (a) Experimental 2D IR spectra of the ν_{NO} in NP4-NO at pD 7.9. (b) Best fits to the experimental 2D IR spectra. Contour levels are drawn at 5% intervals. The τ_2 values and the normalization factors for each 2D plot are given in the top left and bottom right corners, respectively.

The homogenous contribution to the IR linewidth is governed by protein and solvent fluctuations much faster than the experimental time window of a 2D IR experiment. The measured homogenous timescale (T_2^*), falls within the range of 5–12 ps for the ν_{CO} in

myoglobin-CO, neuroglobin-CO and for cyt-$P450_{cam}$-CO substrate complexes.[16, 20] In particular, the homogenous dephasing time for the H64V mutant of myoglobin-CO was measured to be 7.7 ps. In contrast, the homogenous dephasing time for the ν_{NO} of sodium nitroprusside ($Na_2Fe(CN)_5NO{\cdot}2H_2O$, SNP) dissolved in various polar solvents was measured to be ~2 ps.[29, 39] These comparisons suggest that the dephasing timescales are slower in non-polar environments such as the distal pocket of NP4-NO in contrast to the polar solvent environments experienced by the ν_{NO} of sodium nitroprusside. The vibrational anharmonicity value of ~29.5 cm^{-1} for the A_0 and A_1 peaks extracted from the fits of the 2D IR spectra is not affected by pH. This value is similar to the measured anharmonicity of 29 cm^{-1} for the ν_{NO} in wild-type $Mb^{III}NO$ and 28 cm^{-1} for the ν_{NO} in ferric cytochrome C-NO.[24]

The closed conformer at acidic pH is characterized by a well packed distal pocket where the NO is surrounded by non-polar residues held together by hydrogen bonding interaction between the A-B and G-H loops as seen in Figure 4.3a. In contrast, the open conformation at the acidic pH is characterized by greater disorder in the A-B and G-H loops and displays room for several water molecules in the distal pocket.[6] The FFCF of the A_0 and A_1 peaks exhibits spectral diffusion on 3 and 1.4 ps timescales, respectively. The crystal structures of the distal pocket at a higher pH are characterized by a greater degree of loop flexibility and the presence of several water molecules near the nitrosyl binding site. The FFCF of the A_0 and A_1 peaks in the pD 7.9 sample exhibits spectral diffusion on a 1.4 and 0.8 ps timescales, respectively. We assign the fast timescales to fluctuations of the local electric field around the nitrosyl ligand in NP4-NO for the closed and open protein conformers. Our previous work on characterization of the FFCF of the ν_{NO} in SNP found a negative correlation between the solvent polarity and the timescale for spectral diffusion.[29] The solvent polarity was defined by the empirical solvent parameters:

$E_T^N(30)$ and the acceptor number (AN).[40] It is interesting to note that the τ_{c1} timescale of the ν_{NO} in NP4-NO mentioned above are very similar to the measured τ_{c1} values of ν_{NO} in SNP dissolved in ethanol (3.2 ps), methanol (2.3 ps), D_2O (1.4 ps) and H_2O (0.84 ps). Based on the above comparison, we propose that the polarity of the protein distal pocket in the closed and open conformers at pD 5.1 can be characterized by a maximum $E_T^N(30)$ value corresponding to that of ethanol ($E_T^N(30) = 0.65$) and water ($E_T^N(30) = 1$), respectively. The timescale for spectral diffusion of the closed conformer changes from 3 to 1.4 ps on increasing the sample pH. This can be explained by the presence of water molecules reported in the crystal structure resulting in an increase in the polarity of the distal pocket upon increasing the sample pH.

The 2D IR lineshape study also reveals the presence of slow (τ_{c2}) frequency fluctuations of the closed and open conformers. The frequency fluctuations of the ν_{NO} in the closed conformer under all pH conditions are too slow to be measured on the timescale of our experiment and appear static. In contrast the ν_{NO} in the open conformer undergoes frequency fluctuations on the 130 ps and 70 ps timescale for the pD 5.1 and 7.9 samples respectively. We attribute these long timescale dynamics to the structural dynamics of the loop regions of NP4-NO. These dynamics appear to be frozen for the closed conformers on the 100 ps timescale. However, the loop dynamics are faster for the open conformers. Our finding is consistent with X-ray crystallography studies, where it has been found that the A-B and G-H loops are poorly modeled for the open conformers of the NP4-NO protein.[6]

The carbonyl ligand has been used extensively as a vibrational probe in 2D IR studies to measure structural dynamics in the active site of several heme proteins.[16-22] These studies have measured timescales for spectral diffusion on 1-10 ps timescales and also slower timescales ranging from 60-300 ps. The fast timescales can be characterized as local structural fluctuations

around the CO probe and the slower fluctuations have been attributed to global motions involving the entire protein. For example, molecular dynamics simulations have demonstrated that the experimentally measured timescales in the FFCF of the ν_{CO} in wild type and mutant myoglobin-CO are governed by the dynamics of the distal histadine ligand, and protein-water interactions.[18, 22, 41-42] 2D IR studies of the ν_{NO} in wild-type $Mb^{III}NO$ and ferric cytochrome C-NO have measured vibrational frequency fluctuation timescales of 3.3 ps and 5.2 ps, respectively.[23-24] The ν_{NO} in the H64Q-NO mutant of $Mb^{III}NO$ exhibits a slower timescale of ~10 ps in the measured FFCF.[24] A reduction in polar interactions with the nitrosyl ligand in the mutant without the distal histidine, results an increase in the timescale of frequency fluctuations which is in keeping with the trend seen in NP4-NO.

4.3.3 Relating structure, function and dynamics in Nitrophorin 4

The results and discussion of the 2D IR lineshape analysis reveals a picture of a dynamic distal pocket with structural fluctuations on a range of timescales. We next discuss how our measurement of the equilibrium structural fluctuations in the distal pocket of the open and closed conformers of NP4–NO at two different pH conditions shed light on the function of this NO transporter protein. The binding and release of NO from the heme has been described as the following two step process:[7]

$$\text{NP-NO} \underset{k_{on}}{\overset{k_{off1}/k_{off2}\,(\text{pH dep.})}{\rightleftarrows}} [\text{NP:NO}] \underset{k_{-1}}{\overset{k_1}{\rightleftarrows}} \text{NP} + \text{NO}$$

In this model, NO dissociation occurs with two pH-dependent rates ($k_{off1,2}$) involving a slow protein conformational change of the protein and a faster rate (k_1) representing release from the open conformation. It has been shown that the pH dependence of the slower off-rates can be

attributed to the flexibility and dynamics of the loop regions from various mutant studies which have destabilized the closed conformation and altered the pH dependence of the equilibrium populations of the open and closed conformers.[7, 10] Ultrafast rebinding studies following photodissociation of NO from ferric NP4-NO have measured a 10-25 ps and a >150 ps timescale for geminate recombination.[9] The faster timescale has been attributed to NO rebinding from a hydrophobic closed conformer and the longer timescale has been attributed to rebinding from the hydrophilic open conformer.

Our results demonstrate that there is a static distribution of the closed conformers at both pH conditions and a distribution of interconverting open conformers on the ~100 ps timescale. These heterogeneous structures arising from different interactions of the NO and its local environment in the distal pocket, would allow for slightly different rates of thermal bond cleavage resulting in a truly non-exponential ligand release process. The results in this study provide experimental verification for MD simulations which have suggested that the structural loops in NP4 should not be viewed as rigid cages that confine NO, but rather as a "dynamical oil droplet" that contains NO within the fluctuating nonpolar pocket.[6, 11] We directly measure timescales of 3 ps and ~1 ps for fast structural fluctuations in a hydrophobic and hydrophilic environment of the distal pocket.

We plan to perform 2D IR studies on mutants of NP4 where several key residues in the A-B and G-H loops have been replaced to affect the binding and release rates of NO, in the future. Measuring the FFCF of the ν_{NO} in these mutants will allow us to directly probe the correlation between equilibrium structural fluctuations in the distal cavity and the function of this NO transporter protein. The rates of NO binding/release to ferric myoglobin are 10/2000 fold faster than those for NP4, in addition to being described by a single phase.[43] A recent study has

measured the FFCF of the ν_{NO} in wild-type $Mb^{III}NO$ to have a timescale of 3 ps and significant portions of the dynamics were too slow to measure on the experimental timescale.[24] In comparison with the NP4-NO 2D IR results presented in this manuscript, the ν_{NO} in wild-type $Mb^{III}NO$ lacks equilibrium structural fluctuations on the 70-100 ps timescale. This suggests that the equilibrium frequency fluctuations arising from local electric field fluctuations in the distal pocket and the loop dynamics have a role to play in regulating the uptake and diffusion of the nitrosyl ligand in NP4.

4.4 SUMMARY

In summary, we use 2D IR spectroscopy to measure the picosecond structural dynamics in the distal pocket of NP4–NO. We assign the A_0 and A_1 peaks in the nitrosyl stretching region of the FTIR to the ν_{NO} of the closed and open conformers of NP4-NO present at pD 5.1 and 7.9. The assignment is in agreement with previous IR and Raman studies of NP4-NO and $Mb^{III}NO$ and DFT calculations. The measured timescales of the FFCF for the A_0 and A_1 peaks are a quantitative description of the structural heterogeneity and solvent dynamics in the vicinity of the heme. The ability of the open conformer to exchange among its sub-states in ~100 ps measures the structural flexibility of the loop regions. The spectroscopic data provides a microscopic explanation for the previously observed kinetic heterogeneity in the release rates of NO from the protein at all pH conditions. This study highlights how picosecond structural dynamics in the distal pocket of NP4-NO are linked to its function and could hold implications for ligand binding and release in other NO transport and receptor proteins.

REFERENCES

1. Walker, F. A.; Montfort, W. R., The nitric oxide-releasing heme proteins from the saliva of the blood-sucking insect Rhodnius prolixus. *Advances in Inorganic Chemistry* **2001,** *51* (Copyright (C) 2012 American Chemical Society (ACS). All Rights Reserved.), 295-358.

2. Ribeiro, J.; Hazzard, J.; Nussenzveig, R.; Champagne, D.; Walker, F., Reversible binding of nitric oxide by a salivary heme protein from a bloodsucking insect. *Science* **1993,** *260* (5107), 539-541.

3. Bredt, D. S.; Snyder, S. H., Nitric Oxide: A Physiologic Messenger Molecule. *Annual Review of Biochemistry* **1994,** *63* (1), 175-195.

4. Andersen, J. F.; Weichsel, A.; Balfour, C. A.; Champagne, D. E.; Montfort, W. R., The crystal structure of nitrophorin 4 at 1.5 .ANG. resolution: transport of nitric oxide by a lipocalin-based heme protein. *Structure (London)* **1998,** *6* (10), 1315-1327.

5. Weichsel, A.; Andersen, J. F.; Roberts, S. A.; Montfort, W. R., Nitric oxide binding to nitrophorin 4 induces complete distal pocket burial. *Nat. Struct. Biol.* **2000,** *7* (7), 551-554.

6. Kondrashov, D. A.; Roberts, S. A.; Weichsel, A.; Montfort, W. R., Protein Functional Cycle Viewed at Atomic Resolution: Conformational Change and Mobility in Nitrophorin 4 as a Function of pH and NO Binding†,‡. *Biochemistry* **2004,** *43* (43), 13637-13647.

7. Maes, E. M.; Weichsel, A.; Andersen, J. F.; Shepley, D.; Montfort, W. R., Role of Binding Site Loops in Controlling Nitric Oxide Release: Structure and Kinetics of Mutant Forms of Nitrophorin 4†,‡. *Biochemistry* **2004,** *43* (21), 6679-6690.

8. Nienhaus, K.; Maes, E. M.; Weichsel, A.; Montfort, W. R.; Nienhaus, G. U., Structural dynamics controls nitric oxide affinity in nitrophorin 4. *The Journal of biological chemistry* **2004,** *279* (38), 39401-7.

9. Benabbas, A.; Ye, X.; Kubo, M.; Zhang, Z.; Maes, E. M.; Montfort, W. R.; Champion, P. M., Ultrafast Dynamics of Diatomic Ligand Binding to Nitrophorin 4. *Journal of the American Chemical Society* **2010,** *132* (8), 2811-2820.

10. Abbruzzetti, S.; He, C.; Ogata, H.; Bruno, S.; Viappiani, C.; Knipp, M., Heterogeneous Kinetics of the Carbon Monoxide Association and Dissociation Reaction to Nitrophorin 4 and 7 Coincide with Structural Heterogeneity of the Gate-Loop. *Journal of the American Chemical Society* **2012,** *134* (24), 9986-9998.

11. Swails, J. M.; Meng, Y.; Walker, F. A.; Marti, M. A.; Estrin, D. A.; Roitberg, A. E., pH-Dependent Mechanism of Nitric Oxide Release in Nitrophorins 2 and 4. *J. Phys. Chem. B* **2009,** *113* (4), 1192-1201.

12. Marti, M. A.; Estrin, D. A.; Roitberg, A. E., Molecular Basis for the pH Dependent Structural Transition of Nitrophorin 4. *J. Phys. Chem. B* **2009,** *113* (7), 2135-2142.

13. Marti, M. A.; Gonzalez Lebrero, M. C.; Roitberg, A. E.; Estrin, D. A., Bond or Cage Effect: How Nitrophorins Transport and Release Nitric Oxide. *J. Am. Chem. Soc.* **2008,** *130* (5), 1611-1618.

14. Kondrashov, D. A.; Montfort, W. R., Nonequilibrium Dynamics Simulations of Nitric Oxide Release: Comparative Study of Nitrophorin and Myoglobin. *J. Phys. Chem. B* **2007,** *111* (31), 9244-9252.

15. Menyhard, D. K.; Keseru, G. M., Protonation state of Asp30 exerts crucial influence over surface loop rearrangements responsible for NO release in nitrophorin 4. *FEBS letters* **2005,** *579* (24), 5392-8.

16. Thielges, M. C.; Chung, J. K.; Fayer, M. D., Protein dynamics in cytochrome P450 molecular recognition and substrate specificity using 2D IR vibrational echo spectroscopy. *J Am Chem Soc* **2011,** *133* (11), 3995-4004.

17. Bagchi, S.; Thorpe, D. G.; Thorpe, I. F.; Voth, G. A.; Fayer, M. D., Conformational switching between protein substates studied with 2D IR vibrational echo spectroscopy and molecular dynamics simulations. *J Phys Chem B* **2010,** *114* (Copyright (C) 2012 U.S. National Library of Medicine.), 17187-93.

18. Bagchi, S.; Nebgen, B. T.; Loring, R. F.; Fayer, M. D., Dynamics of a myoglobin mutant enzyme: 2D IR vibrational echo experiments and simulations. *J Am Chem Soc* **2010,** *132* (Copyright (C) 2012 U.S. National Library of Medicine.), 18367-76.

19. Ishikawa, H.; Kim, S.; Kwak, K.; Wakasugi, K.; Fayer, M. D., Disulfide bond influence on protein structural dynamics probed with 2D-IR vibrational echo spectroscopy. *Proc Natl Acad Sci U S A* **2007,** *104* (49), 19309-14.

20. Ishikawa, H.; Finkelstein, I. J.; Kim, S.; Kwak, K.; Chung, J. K.; Wakasugi, K.; Massari, A. M.; Fayer, M. D., Neuroglobin dynamics observed with ultrafast 2D-IR vibrational echo spectroscopy. *Proc Natl Acad Sci U S A* **2007,** *104* (41), 16116-21.

21. Finkelstein, I. J.; Ishikawa, H.; Kim, S.; Massari, A. M.; Fayer, M. D., Substrate binding and protein conformational dynamics measured by 2D-IR vibrational echo spectroscopy. *Proceedings of the National Academy of Sciences of the United States of America* **2007,** *104* (8), 2637-2642.

22. Merchant, K. A.; Noid, W. G.; Akiyama, R.; Finkelstein, I. J.; Goun, A.; McClain, B. L.; Loring, R. F.; Fayer, M. D., Myoglobin-CO Substate Structures and Dynamics:

Multidimensional Vibrational Echoes and Molecular Dynamics Simulations. *J. Am. Chem. Soc.* **2003,** *125* (45), 13804-1381.

23. Hunt, N. T.; Greetham, G. M.; Towrie, M.; Parker, A. W.; Tucker, N. P., Relationship between protein structural fluctuations and rebinding dynamics in ferric haem nitrosyls. *Biochem. J.* **2011,** *433* (Copyright (C) 2012 American Chemical Society (ACS). All Rights Reserved.), 459-468.

24. Adamczyk, K.; Candelaresi, M.; Kania, R.; Robb, K.; Bellota-Anton, C.; Greetham, G. M.; Pollard, M. R.; Towrie, M.; Parker, A. W.; Hoskisson, P. A.; Tucker, N. P.; Hunt, N. T., The effect of point mutation on the equilibrium structural fluctuations of ferric Myoglobin. *Phys. Chem. Chem. Phys.* **2012,** *14* (Copyright (C) 2012 American Chemical Society (ACS). All Rights Reserved.), 7411-7419.

25. Soldatova, A. V.; Ibrahim, M.; Olson, J. S.; Czernuszewicz, R. S.; Spiro, T. G., New Light on NO Bonding in Fe(III) Heme Proteins from Resonance Raman Spectroscopy and DFT Modeling. *J. Am. Chem. Soc.* **2010,** *132* (13), 4614-4625.

26. Spiro, T. G.; Soldatova, A. V.; Balakrishnan, G., CO, NO and O2 as vibrational probes of heme protein interactions. *Coordination Chemistry Reviews* **2013,** *257* (2), 511-527.

27. Park, E. S.; Thomas, M. R.; Boxer, S. G., Vibrational Stark Spectroscopy of NO Bound to Heme: Effects of Protein Electrostatic Fields on the NO Stretch Frequency. *J. Am. Chem. Soc.* **2000,** *122* (Copyright (C) 2013 American Chemical Society (ACS). All Rights Reserved.), 12297-12303.

28. Maes, E. M.; Roberts, S. A.; Weichsel, A.; Montfort, W. R., Ultrahigh Resolution Structures of Nitrophorin 4: Heme Distortion in Ferrous CO and NO Complexes. *Biochemistry* **2005,** *44* (38), 12690-12699.

29. Brookes, J. F.; Slenkamp, K. M.; Lynch, M. S.; Khalil, M., Effect of Solvent Polarity on the Vibrational Dephasing Dynamics of the Nitrosyl Stretch in an Fe Complex Revealed by 2D IR Spectroscopy. *J Phys Chem A* **2013**, ASAP.

30. Lynch, M. S.; Slenkamp, K. M.; Cheng, M.; Khalil, M., Coherent Fifth-Order Visible–Infrared Spectroscopies: Ultrafast Nonequilibrium Vibrational Dynamics in Solution. *The Journal of Physical Chemistry A* **2012,** *116* (26), 7023-7032.

31. Khalil, M.; Demirdöven, N.; Tokmakoff, A., Coherent 2D IR Spectroscopy: Molecular Structure and Dynamics in Solution. *The Journal of Physical Chemistry A* **2003,** *107* (27), 5258-5279.

32. Mukamel, S., *Principles of Nonlinear Optical Spectroscopy*. Oxford University Press: New York, 1995.

33. Sung, J.; Silbey, R. J., Four wave mixing spectroscopy for a multilevel system. *The Journal of Chemical Physics* **2001,** *115* (20), 9266.

34. Ding, X. D.; Weichsel, A.; Andersen, J. F.; Shokhireva, T. K.; Balfour, C.; Pierik, A. J.; Averill, B. A.; Montfort, W. R.; Walker, F. A., Nitric oxide binding to the ferri- and ferroheme states of nitrophorin 1, a reversible no-binding heme protein from the saliva of the blood-sucking insect, Rhodnius prolixus. *J. Am. Chem. Soc.* **1999,** *121* (1), 128-138.

35. Sando, G. M.; Zhong, Q.; Owrutsky, J. C., Vibrational and rotational dynamics of cyanoferrates in solution. *J Chem Phys* **2004,** *121* (5), 2158-68.

36. Nienhaus, K.; Palladino, P.; Nienhaus, G. U., Structural Dynamics of Myoglobin: FTIR-TDS Study of NO Migration and Binding†. *Biochemistry* **2007,** *47* (3), 935-948.

37. Miller, L. M.; Pedraza, A. J.; Chance, M. R., Identification of Conformational Substates Involved in Nitric Oxide Binding to Ferric and Ferrous Myoglobin through Difference Fourier Transform Infrared Spectroscopy (FTIR)†. *Biochemistry* **1997,** *36* (40), 12199-12207.

38. Park, J.; Lee, T.; Park, J.; Lim, M., Photoexcitation dynamics of NO-bound ferric myoglobin investigated by femtosecond vibrational spectroscopy. *J. Phys. Chem. B* **2013,** *117* (10), 2850-2863.

39. Tayama, J.; Ohta, K.; Tominaga, K., Vibrational transition frequency fluctuation of the NO stretching mode of sodium nitroprusside in aqueous solutions. *Chem. Lett.* **2012,** *41* (Copyright (C) 2012 American Chemical Society (ACS). All Rights Reserved.), 366-368.

40. Reichardt, C., Solvatochromic dyes as solvent polarity indicators. *Chem. Rev* **1994,** *94* (8), 2319-2358.

41. Massari, A. M.; Finkelstein, I. J.; McClain, B. L.; Goj, A.; Wen, X.; Bren, K. L.; Loring, R. F.; Fayer, M. D., The influence of aqueous versus glassy solvents on protein dynamics: Vibrational echo experiments and molecular dynamics simulations. *Journal of the American Chemical Society* **2005,** *127* (41), 14279-14289.

42. Williams, R. B.; Loring, R. F.; Fayer, M. D., Vibrational Dephasing of Carbonmonoxy Myoglobin. *J. Phys. Chem. B.* **2001,** *105* (19), 4068-4071.

43. Sharma, V. S.; Traylor, T. G.; Gardiner, R.; Mizukami, H., Reaction of nitric oxide with heme proteins and model compounds of hemoglobin. *Biochemistry* **1987,** *26* (13), 3837-3843.

APPENDIX A

EXAMPLE MATLAB CODE FOR FITTING OF 2D IR SPECTRA OF THREE LEVEL SYSTEM

```
clear all
global A1 tc1 w103 amp delta12 T2star A2 tc2 w12 w21 mu12 tau1R w1 tau1NR w01 w10 Dor Tpop
thetaor c2w tau1 t1step mu01 ratio12 ratio21 rho00 Matfin_exp Tau_2_exp w1start w1end t21
triangleR triangleNR

% Input Variables
t1step=10;
tau1R=0:t1step:2700;
tau1NR=0:t1step:1800;
[t1mR, t1R]=size(tau1R);
t1R=tau1R;
t1NR=tau1NR;
tau2=0;
tau3=0:t1step:4000;
t3=tau3;
[t3m, t3n]=size(tau3);
c2w=2.0.*pi.*2.998.*10.^-5;
delta12=24.427354416541906.*c2w;%19.5.*c2w;
w01=434.60778081033.*c2w;
w10=-434.60778081033.*c2w;
w103=-0.081427077295031;
w12=w01-delta12;
w21=w10+delta12;
mu01=1;
mu10=1;
mu12=sqrt(2);
mu21=sqrt(2);
rho00=1;
% hbar=1.05457148E-19;

% Create Frequency Axis
diagonalx=1800:2000;
diagonaly=diagonalx;
newfeq=zeros(1,2048);

for p = 1:2048;
    newfreq(p)=p/(2048*t1step);
end

g=0:1:2048;
freq1=zeros(size(g));
freq2=newfreq(1:2048/2);
freq2=fliplr(freq2);
freq2=freq2.*(-1);
freq1(1:2048/2)=freq2;
```

```
freq1(2048/2+1)=0;
freq1(2048/2+2:end)=newfreq(1:2048/2);

w1start=round(350*2048*3*t1step/100000+2048/2+1);
w1end=round(525*2048*3*t1step/100000+2048/2+1);
w1=freq1(w1start:w1end)'./2.9979e-05;
w1=w1+1500;
w3=w1;
%Clear to save memory
clear freq1
clear freq2
clear newfreq


%Load Data for Fitting
load('Tau_2_exp.mat');
Tau_2_exp=Tau_2_exp;
load('Matfin_Tau2_D2O.mat')
Mat_exp=Matfin_Tau2_D2O(:,:,:);
load('w1exp.mat')
load('w3exp.mat')
load('triangleR_D2O.mat')
triangleR=triangleR_D2O;
load('triangleNR_D2O.mat')
triangleNR=triangleNR_D2O;
w3exp(23)=[];
%
% figure
% contourf(Mat_exp(:,:,2),40)
%
% figure
% contourf(Mat_exp(:,:,2),20)

%Normalize the matrices
[s3 s1]=size(w3exp);
% [t21 t22]=size(Tau_2_EG);

%%Number of tau2 points in data set
t21=18;

%Check Spectrum
% figure
% contourf(matfin_D2O_exp(:,:,2),40)

%Create zero mtrix so interp doesn't increase size of matrix each round
Mat_D2O_Tau2_interp1=zeros(63,121);

%interp experimental matrix to have equal points on x and y axis and same
%number of points as simulated spectrum

for m=1:t21;
for x=1:s3;
    Mat_exp_interp1(x,:,m)=interp1(w1exp,Mat_exp(x,:,m),w1);
```

```
end
end

[smat1 smat2 smat3]=size(Mat_exp_interp1);
for n=1:smat3;
for x=1:smat2;
    Matfin_exp1(:,x,n)=interp1(w3exp,Mat_exp_interp1(:,x,n),w3);
%     Matfin_exp1(:,x,n)=interp1(w3exp, Mat_D2O_Tau2_interp1(:,x,n),w3');
end
 Matfin_exp(:,:,n)=Matfin_exp1(:,:,n)./(max(max(Matfin_exp1(:,:,1))));
end

%Get rid of the NAN
Matfin_exp(96:109,:,:)=[];

% Matfin_exp(13,:,:)=[];
%
% figure
% contourf(Matfin_exp(:,:,2),40)


%Clear to save memeory
% clear Mat_D2O_Tau2_interp
clear Mat_exp_interp1
clear matfin_D2O_exp
clear Matfin_exp1

%%%Line Shape Functions
%%%Make sure that FFCFs have been intengrated twice
Tpop=22000;
thetaor=0;
Dor=8.3E-6;
```

FS^-1

```
%Starting from FTIR FITS
% A1=0.000956905307935752;
% tc1=35056.3651039564;   %15000;
% A2=0.00121116566083891;
% tc2=1854.67615469559;
% T2star=2233.25888520697;

%%Starting from 2D fits that look good
A1=0.001229213846698;
tc1=1.385150206426212e+03;
A2=0.000665859832646125;
tc2=5000000;
T2star=1.973156719554166e+03;
% delta12=18.880048466552.*c2w;%19.5.*c2w;
% w12=w01-delta12;
% w21=w10+delta12;
mu12=1.398287157635783;
```

```
amp=0.858049521703135;

%

% q0=[mu12,amp];
% lb=[1.1,0.8];
% ub=[1.6,1.6];
%Starting Parameters for this round of fit
q0=[A1,tc1,T2star,mu12,amp];
lb=[0.001,1380,1900,1.3,0.85];
ub=[0.0013,1390,2000,1.4,0.95];
% Comment the next three lines out if you do not want to actually perform
% fit
% options=optimset('MaxFunEvals', 100000, 'MaxIter', 100000,'TolFun',1E-10);
% [q, resnorm,
residual(:,:,:),exitflag,output,lambda,jacobian]=lsqnonlin('Fit_3D',q0,lb,ub,options);
% ci=nlparci(q,residual,'jacobian',jacobian,'alpha',0.05);

%%%Line Shape Functions
%%%Make sure that FFCFs have been intengrated twice

%Make sure the next lines are uncommented if you performed a fit inorder to
%see what your fit looks like
% A1=q(1);
% tc1=q(2);
% T2star=q(3);
% mu12=q(4);
% amp=q(5);

for h=1:t21;

tau2=Tau_2_exp(h);

% mu12=q(1);
% amp=q(2);

% w103=q(6);
% delta12=q(7).*c2w;
% w12=w01-delta12;
% w21=w10+delta12;
%%%Line shape functions

g11 = @(t) A1.*A1.*tc1.*tc1.*(exp(-abs(t)./tc1)+abs(t)./tc1-1);%+A2.*A2.*tc2.*tc2.*(exp(-
abs(t)./tc2)+abs(t)./tc2-1);
g12 = @(t) 2.*amp.*g11(t);
g22 = @(t) 4.*amp.*amp.*g11(t);
g21=g12;

%%%Orientational contribution
% Dor=q(2);%5.5E-7;%%% fs^-1
% thetaor=0; %%%The angle between 01 and 12 vectors

c1 = @(t) exp(-2.*Dor.*abs(t));
```

```
c2 = @(t) exp(-6.*Dor*abs(t));

%%%Nonrephasing


%Response functions

%%%%%%%%%%%%%%%%%%%%%%%%%%%%%%%%
%%%%%%%%%%%Rephasing%%%%%%%%%%%%
%%%%%%%%%%%%%%%%%%%%%%%%%%%%%%%%

%%%%Orientational Component
t1=tau1R;
tau1=tau1R;
t3=t1R;

[j t1n]=size(t1);
[j t3n]=size(t3);

Y_2_0101=(1./9).*c1(t1).*c1(t3).*(1+(4./5).*c2(tau2));
Y_3_0101=(1./9).*c1(t1).*c1(t3).*(1+(4./5).*c2(tau2));
Y_5_0121=(1./9).*c1(t1).*c1(t3).*(1+(4./5).*c2(tau2)).*cos(thetaor).^2+(1./15).*c1(t1).*c1(t3).*c
2(tau2).*sin(thetaor).^2;


R2_0101=zeros(t1n,t3n,1);

for l=1:t1n;
    t1=tau1(l);
    R2_0101(:,l,1)=Y_2_0101.*rho00.*(mu01).^4.*exp(1i.*w10.*t1-1i.*w103.*t3).*exp(-
(g11(t1+tau2)+g11(-tau2-t3)+g11(t1)-g11(t3+t1+tau2)-g11(-tau2)+g11(t3))).*exp(-
(t3+t1)./(2.*Tpop)).*exp(-tau2./Tpop).*(exp(-t1./T2star).*exp(-t3./T2star));
end

% figure
% contourf(tau1,tau3,R2_0101,10)

% w_R2=fftshift(fft2(R2_0101,2048,2048));
% w_R2=fliplr(w_R2);
%
% figure
% contourf(w1,w3,real(w_R2(w1start:w1end,w1start:w1end)),-1200:100:1200)
% axis square
% box on
% set(gca,'tickdir', 'out')
% set(gca, 'ticklength', [0.01,0.03])
% set(gca, 'fontsize', 16)
% set(gca, 'linewidth', 2)
% set(gca, 'fontname', 'arial')
% set(gca, 'fontweight', 'b')
% xlabel('\omega_1/2\pic (cm^-^1)')
% ylabel('\omega_3/2\pic (cm^-^1)')
% title('Rephasing: R_2^0^1^0^1 \tau_2=0')
```

```
R3_0101=zeros(t1n,t3n,1);

for l=1:t1n;
    t1=tau1(l);
    R3_0101(:,l,1)=Y_3_0101.*rho00.*(mu01).^4.*(exp(1i.*w10.*t1-1i.*w103.*t3).*exp(-conj((g11(-
t3)+g11(t1)-g11(t3+tau2+t1)+g11(t3+tau2)+g11(tau2+t1)-g11(tau2))))).*exp(-
(t3+t1)./(2.*Tpop)).*exp(-tau2./Tpop).*(exp(-t1./T2star).*exp(-t3./T2star));
end

% w_R3=fftshift(fft2(R3_0101,2048,2048));
% w_R3=fliplr(w_R3);
%
% figure
% contourf(w1,w3,real(w_R3(w1start:w1end,w1start:w1end)),-1200:100:1200)
% axis square
% box on
% set(gca,'tickdir', 'out')
% set(gca, 'ticklength', [0.01,0.03])
% set(gca, 'fontsize', 16)
% set(gca, 'linewidth', 2)
% set(gca, 'fontname', 'arial')
% set(gca, 'fontweight', 'b')
% xlabel('\omega_1/2\pic (cm^-^1)')
% ylabel('\omega_3/2\pic (cm^-^1)')
% title('Rephasing: R_3^0^1^0^1 \tau_2=0')


R5_0121=zeros(t1n,t3n,1);

for l=1:t1n;
    t1=tau1(l);
    R5_0121(:,l,1)=Y_5_0121.*rho00.*(mu01).^2.*(mu12).^2.*(exp(+1i.*w10.*t1+1i.*w12.*t3).*exp(-
conj(g22(t3)+g11(-tau2)+g11(t1+tau2+t3)+g12(-t3-tau2)-g12(-t3)-g12(-tau2)+g21(t1+tau2)-
g21(t1+tau2+t3)-g21(-t3)+g11(t1)-g11(-t3-tau2)-g11(t1+tau2)+g11(-t3)))).*exp(-
t3./((3./2).*Tpop)).*exp(-tau2./Tpop).*exp(-t1./(2.*Tpop)).*(exp(-t1./T2star).*exp(-t3./T2star));
end

% figure
% contourf(R5_0121)

% w_R5=fftshift(fft2(R5_0121,2048,2048));
% w_R5=fliplr(w_R5);
%
% figure
% contourf(w1,w3,real(w_R5(w1start:w1end,w1start:w1end)),20)
% axis square
% box on
% set(gca,'tickdir', 'out')
% set(gca, 'ticklength', [0.01,0.03])
% set(gca, 'fontsize', 16)
% set(gca, 'linewidth', 2)
% set(gca, 'fontname', 'arial')
```

```
% set(gca, 'fontweight', 'b')
% xlabel('\omega_1/2\pic (cm^-^1)')
% ylabel('\omega_3/2\pic (cm^-^1)')
% title('Rephasing: R_5^0^1^2^1 \tau_2=0')

% matnrf1=zeros(2048,301);
% matrf1=zeros(2048,2048);

timemat_R=R2_0101+R3_0101-R5_0121;

matrf2=timemat_R.*triangleR;

wmat_R(:,:,h)=fliplr(fftshift(fft2(matrf2(:,:),2048,2048)));

% % wmat_R=fliplr(fftshift(fft2(timemat_R,2048,2048)));
%
% figure
% contourf(real(wmat_R(w1start:w1end,w1start:w1end)),20)
% title('Rephasing frequeny \tau_2=0')

% figure
% contourf(tau1,tau3,timemat_R)
% axis square
% box on
% set(gca,'tickdir', 'out')
% set(gca, 'ticklength', [0.01,0.03])
% set(gca, 'fontsize', 16)
% set(gca, 'linewidth', 2)
% set(gca, 'fontname', 'arial')
% set(gca, 'fontweight', 'b')
% xlabel('\tau1_1 (fs)')
% ylabel('\tau3_3(fs)')
% title('Rephasing time domain \tau_2=0')


% figure
% contourf(w1,w3,wmat_R(w1start:w1end,w1start:w1end),20)


%%%%%%%%%%%%%%%%%%%%%%%%%%%%%%%%
%%%%%%%%%%Nonrephasing%%%%%%%%%%
%%%%%%%%%%%%%%%%%%%%%%%%%%%%%%%%

%%%Orientational Component

t1=tau1NR;
tau1=t1;
t3=t1;
[j t1n]=size(t1);
[j t3n]=size(t3);

Y_1_0101=(1./9).*c1(t1).*c1(t3).*(1+(4./5).*c2(tau2));
Y_4_0101=(1./9).*c1(t1).*c1(t3).*(1+(4./5).*c2(tau2));
```

```
Y_6_0121=(1./9).*c1(t1).*c1(t3).*(1+(4./5).*c2(tau2)).*cos(thetaor).^2+(1./9).*c1(t1).*c1(t3).*(1
-(2./5).*c2(tau2)).*sin(thetaor).^2;


NR1_0101=zeros(t1n,t3n,1);

for l=1:t1n;
    t1=tau1(l);
    NR1_0101(:,l,1)=Y_1_0101.*rho00.*abs(mu01).^4.*exp(-(1i.*w10*t1+1i.*w103.*t3)).*exp(-(g11(-
tau2)+g11(t1+tau2+t3)+g11(t1)-g11(-t3-tau2)-g11(t1+tau2)+g11(-t3))).*exp(-
(t3+t1)./(2.*Tpop)).*exp(-tau2./Tpop).*(exp(-t1./T2star).*exp(-t3./T2star));
end
%
% w_NR1=fftshift(fft2(NR1_0101,2048,2048));
%
% % figure
% % contourf(tau1,tau3,NR1_0101,10)
% % title( 'NR1')
%
% figure
% contourf(w1,w3,real(w_NR1(w1start:w1end,w1start:w1end)),20)
% axis square
% box on
% set(gca,'tickdir', 'out')
% set(gca, 'ticklength', [0.01,0.03])
% set(gca, 'fontsize', 16)
% set(gca, 'linewidth', 2)
% set(gca, 'fontname', 'arial')
% set(gca, 'fontweight', 'b')
% xlabel('\omega_1/2\pic (cm^-^1)')
% ylabel('\omega_3/2\pic (cm^-^1)')
% title('NR R_1^0^1^0^1 \tau_2=0')
% hold on
% plot(diagonalx,diagonaly,'k--','linewidth',3)

NR4_0101=zeros(t1n,t3n,1);
for l=1:t1n;
    t1=tau1(l);
    NR4_0101(:,l,1)=Y_4_0101.*rho00.*abs(mu01).^4.*exp(-1i.*w10.*t1-1i.*w103.*t3).*exp(-
(g11(t3)+g11(t1)+g11(t1+tau2+t3)-g11(t3+tau2)-g11(tau2+t1)+g11(tau2))).*exp(-
(t3+t1)./(2.*Tpop)).*exp(-tau2./Tpop).*(exp(-t1./T2star).*exp(-t3./T2star));
end


% w_NR4=fftshift(fft2(NR4_0101,2048,2048));
%
%
% figure
% contourf(w1,w3,real(w_NR4(w1start:w1end,w1start:w1end)),-1200:100:1200)
% axis square
% box on
% set(gca,'tickdir', 'out')
% set(gca, 'ticklength', [0.01,0.03])
```

```
% set(gca, 'fontsize', 16)
% set(gca, 'linewidth', 2)
% set(gca, 'fontname', 'arial')
% set(gca, 'fontweight', 'b')
% xlabel('\omega_1/2\pic (cm^-^1)')
% ylabel('\omega_3/2\pic (cm^-^1)')
% title('NR R_4^0^1^0^1 \tau_2=0')
% hold on
% plot(diagonalx,diagonaly,'k--','linewidth',3)


NR6_0121=zeros(t1n,t3n,1);
for l=1:t1n;
    t1=tau1(l);
    NR6_0121(:,l,1)=Y_6_0121.*rho00.*abs(mu01).^2.*abs(mu12).^2.*exp(-
1i.*w10*t1+1i.*(w12).*t3).*exp(-conj(g22(t3)+g11(t1+tau2)+g11(-tau2-t3)+g12(-tau2)-g12(t3)-g12(-
tau2-t3)+g21(t1+tau2+t3)-g21(t1+tau2)-g21(t3)+g11(t1)-g11(t3+t1+tau2)-g11(-tau2)+g11(t3))).*exp(-
t3./((3./2).*Tpop)).*exp(-tau2./Tpop).*exp(-t1./(2.*Tpop)).*(exp(-t1./T2star).*exp(-t3./T2star));
end
%
% w_NR6=fftshift(fft2(NR6_0121,2048,2048));

% figure
% contourf(w1,w3,real(w_NR6(w1start:w1end,w1start:w1end)),-1200:100:1200)
% axis square
% box on
% set(gca,'tickdir', 'out')
% set(gca, 'ticklength', [0.01,0.03])
% set(gca, 'fontsize', 16)
% set(gca, 'linewidth', 2)
% set(gca, 'fontname', 'arial')
% set(gca, 'fontweight', 'b')
% xlabel('\omega_1/2\pic (cm^-^1)')
% ylabel('\omega_3/2\pic (cm^-^1)')
% title('NR R_6^0^1^2^1 \tau_2=0')
% hold on
% plot(diagonalx,diagonaly,'k--','linewidth',3)

timemat_NR=NR1_0101+NR4_0101-NR6_0121;


matnrf2=timemat_NR(:,:).*triangleNR;

wmat_NR(:,:,h)=fftshift(fft2(matnrf2,2048,2048));

% % wmat_R=fliplr(fftshift(fft2(timemat_R,2048,2048)));
% figure
% contourf(w1,w3,real(wmat_NR(w1start:w1end,w1start:w1end)),20)
%
% figure
% contourf(real(wmat_R(w1start:w1end,w1start:w1end)),20)
% title('Rephasing frequeny \tau_2=0')
```

```
% wmat_NR=fftshift(fft2(timemat_NR,2048,2048));

% figure
% contourf(w1,w3,real(wmat_NR(w1start:w1end,w1start:w1end)),-1200:100:1200)
% axis square
% box on
% set(gca,'tickdir', 'out')
% set(gca, 'ticklength', [0.01,0.03])
% set(gca, 'fontsize', 16)
% set(gca, 'linewidth', 2)
% set(gca, 'fontname', 'arial')
% set(gca, 'fontweight', 'b')
% xlabel('\omega_1/2\pic (cm^-^1)')
% ylabel('\omega_3/2\pic (cm^-^1)')
% title('NR frequency')
% hold on
% plot(diagonalx,diagonaly,'k--','linewidth',3)
%
%
% figure
% contourf(tau1,tau3,timemat_NR)
% axis square
% box on
% set(gca,'tickdir', 'out')
% set(gca, 'ticklength', [0.01,0.03])
% set(gca, 'fontsize', 16)
% set(gca, 'linewidth', 2)
% set(gca, 'fontname', 'arial')
% set(gca, 'fontweight', 'b')
% xlabel('\tau1_1 (fs)')
% ylabel('\tau3_3(fs)')
% title('NR time \tau_2=0')




% Matfin(:,:,k)=real(wmat_R(:,:,k)+wmat_NR(:,:,k));
% max1=max(max(Matfin(:,:,1)));
Matfin(:,:,h)=real(wmat_R(:,:,h)+wmat_NR(:,:,h));

diagonalx=1850:1950;
diagonaly=diagonalx;

figure
contourf(w1(1:78),w3(1:78),(real(Matfin(w1start:(w1start+77),w1start:(w1start+77),h))./max(max(Ma
tfin(:,:,1)))),20);
axis square
axis([1885 1965 1885 1965])
box on
set(gca,'tickdir', 'out')
set(gca, 'ticklength', [0.03,0.01])
set(gca, 'fontsize', 16)
```

```
set(gca, 'linewidth', 3)

set(gca, 'fontname', 'arial')
set(gca, 'fontweight', 'b')
xlabel('\omega_1/2\pic (cm^-^1)')
ylabel('\omega_3/2\pic (cm^-^1)')
% title('Correlation Spectrum')
hold on
plot(diagonalx,diagonalx,'k--','linewidth',3)
plot(diagonalx,(diagonalx-delta12),'k--','linewidth',3)
hold off
end


for h=1:t21
figure
contourf(w1(1:78),w3(1:78),real(Matfin_exp(1:78,1:78,h)),20);
axis square
axis([1885 1965 1885 1965])
box on
set(gca,'tickdir', 'out')
set(gca, 'ticklength', [0.03,0.01])
set(gca, 'fontsize', 16)
set(gca, 'linewidth', 2)
set(gca, 'fontname', 'arial')
set(gca, 'fontweight', 'b')
xlabel('\omega_1/2\pic (cm^-^1)')
ylabel('\omega_3/2\pic (cm^-^1)')
% title('Correlation Spectrum')
hold on
plot(diagonalx,diagonalx,'k--','linewidth',3)
hold off
end

for k=1:t21
Matfin_norm(:,:,k)=Matfin(w1start:w1end,w1start:w1end,k)./max(max(Matfin(:,:,1)));
end

slice_fundamental=Matfin_norm(:,53,:);
slice_fundamental_exp=Matfin_exp(:,53,:);
slice_fundamental2=Matfin_norm(:,58,:);
slice_fundamental_exp2=Matfin_exp(:,58,:);
slice_fundamental3=Matfin_norm(:,48,:);
slice_fundamental_exp3=Matfin_exp(:,48,:);

slice_fundamental_3=Matfin_norm(53,:,:);
slice_fundamental_exp_3=Matfin_exp(53,:,:);
slice_fundamental2_3=Matfin_norm(58,:,:);
slice_fundamental_exp2_3=Matfin_exp(58,:,:);
slice_fundamental3_3=Matfin_norm(48,:,:);
slice_fundamental_exp3_3=Matfin_exp(48,:,:);
```

```
% %%%plot slices along w1
for k=1:t21
figure
plot(w3(1:95),slice_fundamental_exp(1:95,1,k),'k','linewidth',3)
axis([1885 1965 -1.2 1])
box on
set(gca,'tickdir', 'out')
set(gca, 'ticklength', [0.03,0.01])
set(gca, 'fontsize', 16)
set(gca, 'linewidth', 3)
set(gca, 'fontname', 'arial')
set(gca, 'fontweight', 'b')
title('plotted on /w3')
hold on
plot(w3(1:95),slice_fundamental(1:95,1,k),'r','linewidth',3)
plot(w3(1:95),slice_fundamental_exp2(1:95,1,k),'k--','linewidth',3)
plot(w3(1:95),slice_fundamental2(1:95,1,k),'r--','linewidth',3)
plot(w3(1:95),slice_fundamental_exp3(1:95,1,k),'k-.','linewidth',3)
plot(w3(1:95),slice_fundamental3(1:95,1,k),'r-.','linewidth',3)
hold off
end
% %%%plot slices along w3
for k=1:t21
figure
plot(w1(1:95),slice_fundamental_exp_3(1,1:95,k),'k','linewidth',3)
axis([1885 1965 -1.2 1])
box on
set(gca,'tickdir', 'out')
set(gca, 'ticklength', [0.03,0.01])
set(gca, 'fontsize', 16)
set(gca, 'linewidth', 3)
set(gca, 'fontname', 'arial')
set(gca, 'fontweight', 'b')
hold on
plot(w1(1:95),slice_fundamental_3(1,1:95,k),'r','linewidth',3)
plot(w1(1:95),slice_fundamental_exp2_3(1,1:95,k),'k--','linewidth',3)
plot(w1(1:95),slice_fundamental2_3(1,1:95,k),'r--','linewidth',3)
plot(w1(1:95),slice_fundamental_exp3_3(1,1:95,k),'k-.','linewidth',3)
plot(w1(1:95),slice_fundamental3_3(1,1:95,k),'r-.','linewidth',3)
hold off
end



%%%Simulate FTIR

load('SNP_32_7mg_D2O_beforescan_81911_sub.txt')
SNP_exp=SNP_32_7mg_D2O_beforescan_81911_sub(1555:1650,:);
SNP_exp(:,2)=SNP_exp(:,2)./max(SNP_exp(:,2));

t1step=3;
% c2w=2.0.*pi.*2.998.*10.^-5;
w01=-434.60778081033.*c2w;
```

```
% mu01=1;
t=1:3:8000;

% A1=q(1);
% A2=q(2);
% tc2=q(3);
% T2star=q(4);

% phi=2.089;
% theta=92;


for p = 1:8192;
    newfreq(p)=p/(8192*t1step);
end
g=0:1:8192;
freq1=zeros(size(g));
freq2=newfreq(1:8192/2);
freq2=fliplr(freq2);
freq2=freq2.*(-1);
freq1(1:8192/2)=freq2;
freq1(8192/2+1)=0;
freq1(8192/2+2:end)=newfreq(1:8192/2);

w1start=round(200*8192*3*t1step/100000+8192/2+1);
w1end=round(600*8192*3*t1step/100000+8192/2+1);
w1=freq1(w1start:w1end)'./2.9979e-05;
w1=w1+1500;

w3=w1;


Tor=46000;


g = @(t) A1.*A1.*tc1.*tc1.*(exp(-abs(t)./tc1)+abs(t)./tc1-1);%+A2.*A2.*tc2.*tc2.*(exp(-
abs(t)./tc2)+abs(t)./tc2-1);%
%%cos part -1./((1+theta.^2*tc13.^2).^2).*((theta.^3.*tc13.^3.*cos(phi).*abs(t)-
theta.^2.*tc13.^3.*exp(-abs(t)./tc13).*cos(theta.*abs(t)+phi)-
cos(phi).*abs(t).*theta.^2.*tc13.^2-2.*theta.*tc13.^2.*sin(phi)+2.*theta.*tc13.^2.*exp(-
abs(t)./tc13).*sin(theta.*abs(t)+phi)+tc13.*cos(phi)-tc13.*exp(-
abs(t)./tc13).*cos(theta.*abs(t)+phi)+theta.*tc13.*sin(phi).*abs(t)-
cos(phi).*abs(t)).*tc13.*A13.^2);

R1=abs(mu01).^2.*exp(-1i.*w01.*t).*exp(-g(t)).*exp(-abs(t)./T2star).*exp(-
abs(t)./(2.*Tpop)).*exp(-abs(t)./Tor);

[rR cR]=size(R1);
ar=1-((1./cR).*(1:1:cR));
freq=fftshift(fft(R1.*ar,8192));

% figure(1)
% plot(w1,real(freq(w1start:w1end)))
```

```
SIM_interp=interp1(w1,freq(w1start:w1end),SNP_exp(:,1));
SIM_interp=SIM_interp./max(SIM_interp);

figure
plot(SNP_exp(:,1),SNP_exp(:,2),'k',SNP_exp(:,1),real(SIM_interp),'r','linewidth',3)
axis square
axis([1890 1965 0 1])
box on
set(gca, 'ticklength', [0.03,0.01])
set(gca,'xTick',[1895:20:1955])
% set(gca,'yTick',[1895:20:1955])
set(gca,'tickdir', 'out')
set(gca, 'ticklength', [0.03,0.01])
set(gca, 'fontsize', 16)
set(gca, 'linewidth', 3)
set(gca, 'fontname', 'arial')
set(gca, 'fontweight', 'b')
title('FTIR')

% %%%Fit the FTIR with the new parameters
%
% global  tc2
% q0=[A1,A2,T2star];
% lb=[0.00001,0.0001,1000];
% ub=[.001,0.001,3000];
% options=optimset('MaxFunEvals', 1000000, 'MaxIter', 1000000,'TolFun',1E-15);
% [f, resnorm, residual,exitflag,output,lambda,jacobian]=lsqnonlin('FITFTIR',q0,lb,ub,options);
%
% A1=f(1);
% A2=f(2);
% T2star=f(3);
%
% h = @(t) A1.*A1.*tc1.*tc1.*(exp(-abs(t)./tc1)+abs(t)./tc1-1)+A2.*A2.*tc2.*tc2.*(exp(-
abs(t)./tc2)+abs(t)./tc2-1);%
%
% R1_fit=abs(mu01).^2.*exp(-1i.*w01.*t).*exp(-h(t)).*exp(-abs(t)./T2star).*exp(-
abs(t)./(2.*Tpop)).*exp(-abs(t)./Tor);
%
% [rR cR]=size(R1_fit);
% ar=1-((1./cR).*(1:1:cR));
% freq_fit=fftshift(fft(R1_fit.*ar,8192));
%
% % figure(1)
% % plot(w1,real(freq(w1start:w1end)))
%
%
% SIM_interp_fit=interp1(w1,freq_fit(w1start:w1end),SNP_exp(:,1));
% SIM_interp_fit=SIM_interp_fit./max(SIM_interp_fit);
%
% figure
% plot(SNP_exp(:,1),SNP_exp(:,2),'k',SNP_exp(:,1),real(SIM_interp_fit),'r','linewidth',3)
```

```
% axis([1870 1950 0 1])
% axis square
% set(gca, 'Tickdir', 'out');
% set(gca, 'FontWeight','bold')
% set(gca,'FontSize',20)
% set(gca, 'FontName','Arial')
% set(gca,'TickLength', [0.03, 0.01])
% set(gca,'LineWidth', 3)
% title('FTIR')



%%%%%% Saving it!

% save Mat_fit1 Mat_fit1
% save w1 w1
% save w3 w3
```

Published with MATLAB® R2013a

APPENDIX B

EXAMPLE MATLAB CODE FOR FITTING OF 2D IR SPECTRA OF SIX LEVEL SYSTEM

```
clear all
global  A1 tc1 amp w103 T2star A2 tc2 w12 w21 mu12 tau1R w1 tau1NR w01 w10 Dor Tpop thetaor c2w
tau1 t1step mu01 ratio12 ratio21 rho00 Matfin_exp Tau_2_exp w1start w1end t21 triangleR
triangleNR

%%Variables
t1step=10;
tau1R=0:t1step:5000;
tau1NR=0:t1step:5000;
[t1mR, t1R]=size(tau1R);
t1R=tau1R;
t1NR=tau1NR;
tau2=0;
tau3=0:t1step:4000;
t3=tau3;
[t3m, t3n]=size(tau3);
c2w=2.0.*pi.*2.998.*10.^-5;

rho00=1;
% hbar=1.05457148E-19;
```

```
diagonalx=1800:2000;
diagonaly=diagonalx;


newfeq=zeros(1,2048);

for p = 1:2048;
    newfreq(p)=p/(2048*t1step);
end

g=0:1:2048;
freq1=zeros(size(g));
freq2=newfreq(1:2048/2);
freq2=fliplr(freq2);
freq2=freq2.*(-1);
freq1(1:2048/2)=freq2;
freq1(2048/2+1)=0;
freq1(2048/2+2:end)=newfreq(1:2048/2);

w1start=round(350*2048*3*t1step/100000+2048/2+1);
w1end=round(525*2048*3*t1step/100000+2048/2+1);
```

```
w1=freq1(w1start:w1end)'./2.9979e-05;
w1=w1+1500;
w3=w1;

clear freq1
clear freq2
clear newfreq


%%%Load Data for Fitting
% load('Tau_2_MeOH.mat');
% Tau_2_exp=Tau_2_MeOH;
% load('matfin_MeOH_exp.mat')
% Mat_exp=matfin_MeOH_exp;
% load('w1exp.mat')
% load('w3exp.mat')
load('triangleR.mat')
% load('triangle.mat')
% triangleR=triangleR_MeOH;
load('triangleNR.mat')
% triangleNR=triangleNR_MeOH;
% w3exp(23)=[];
%
% figure
% contourf(Mat_exp(:,:,2),40)
%
% figure
% contourf(Mat_exp(:,:,2),20)

%%Normalize the matrices
% [s3 s1]=size(w3exp);
% [t21 t22]=size(Tau_2_EG);

t21=13;


% figure
% contourf(matfin_MeOH_exp(:,:,2),40)

% Mat_MeOH_Tau2_interp1=zeros(63,121);
%
% for m=1:t21;
% for x=1:s3;
%     Mat_exp_interp1(x,:,m)=interp1(w1exp,Mat_exp(x,:,m),w1);
% end
% end
%
% [smat1 smat2 smat3]=size(Mat_exp_interp1);
% for n=1:smat3;
% for x=1:smat2;
%     Matfin_exp1(:,x,n)=interp1(w3exp,Mat_exp_interp1(:,x,n),w3);
% %     Matfin_exp1(:,x,n)=interp1(w3exp, Mat_D2O_Tau2_interp1(:,x,n),w3');
% end
% Max=(max(max(Matfin_exp1(:,:,1))));
```

```
%  Matfin_exp(:,:,n)=Matfin_exp1(:,:,n)./(max(max(Matfin_exp1(:,:,1))));
% end

% Matfin_exp(79:109,:,:)=[];

% Matfin_exp(13,:,:)=[];
%
% figure
% contourf(Matfin_exp(:,:,2),40)


%%%clear for more memory
% clear Mat_D2O_Tau2_interp
% clear Mat_exp_interp1
% clear matfin_MeOH_exp
% clear Matfin_exp1

%%%Line Shape Functions
%%%Make sure that FFCFs have been intengrated twice
Tpop_a=28000;
Tpop_b=28000;
thetaor=0;
Dor=3.6E-6;
```

```
%Starting from FTIR FITS
% A1=0.000956905307935752;
% tc1=35056.3651039564;   %15000;
% A2=0.00121116566083891;
% tc2=1854.67615469559;
% T2star=2233.25888520697;

%%From Original NP4 Paper

%Open Conformation
w01_a=405*c2w;
w10_a=-405.*c2w;
delta12_a=29.*c2w;
w12_a=w01_a-delta12_a;
w21_a=w10_a+delta12_a;
mu01_a=1;
mu10_a=1;
mu12_a=sqrt(2);
mu21_a=sqrt(2);
A1_a=0.46./1000;
tc1_a=4.*1000;
A2_a=0.67./1000;
tc2_a=50000;
T2star_a=2030;



%Closed Conformation
w01_b=418.*c2w;
```

```
w10_b=-418.*c2w;
delta12_b=29.*c2w;
w12_b=w01_b-delta12_b;
w21_b=w10_b+delta12_b;
mu01_b=1;
mu10_b=1;
mu12_b=sqrt(2);
mu21_b=sqrt(2);
A1_b=0.65./1000;
tc1_b=1.3.*1000;
A2_b=1.3./1000;
tc2_b=100.*1000;
T2star_b=2000;


%
% q0=[A1,A2,tc2,T2star,mu12,tc1,w12];%,tc1,tc2,T2star,delta12];
% lb=[0.0001,0.0001,1000,1500,1.3,20000,22];
% ub=[0.001,0.002,3000,6000,1.5,30000,28];

% q0=[A1,T2star,tc1];%,tc1,tc2,T2star,delta12];
% lb=[0.0001,1000,5000];
% ub=[0.001,6000,30000];

% q0=[tc1];
% lb=[25243];
% ub=[25400];
%
% %
% options=optimset('MaxFunEvals', 100000, 'MaxIter', 100000,'TolFun',1E-10);
% [q, resnorm,
residual(:,:,:),exitflag,output,lambda,jacobian]=lsqnonlin('Fit_3D',q0,lb,ub,options);

% ci=nlparci(q,residual,'jacobian',jacobian,'alpha',0.05);

%%%Line Shape Functions
%%%Make sure that FFCFs have been intengrated twice

Tau_2=0:500:10000;

for h=1:21;

tau2=Tau_2(h);
% % % k=1;
% tc1=q(1);



%%%Line shape functions

g11 = @(t) A1_a.*A1_a.*tc1_a.*tc1_a.*(exp(-abs(t)./tc1_a)+abs(t)./tc1_a-
1)+A2_a.*A2_a.*tc2_a.*tc2_a.*(exp(-abs(t)./tc2_a)+abs(t)./tc2_a-1);
g12 = @(t) 2.*g11(t);
```

```
g22 = @(t) 4.*g11(t);
g21=g12;

h11 = @(t) A1_b.*A1_b.*tc1_b.*tc1_b.*(exp(-abs(t)./tc1_b)+abs(t)./tc1_b-
1)+A2_b.*A2_b.*tc2_b.*tc2_b.*(exp(-abs(t)./tc2_b)+abs(t)./tc2_b-1);
h12 = @(t) 2.*h11(t);
h22 = @(t) 4.*h11(t);
h21=h12;

%%%Orientational contribution
% Dor=q(2);%5.5E-7;%%% fs^-1
% thetaor=0; %%%The angle between 01 and 12 vectors

c1 = @(t) exp(-2.*Dor.*abs(t));
c2 = @(t) exp(-6.*Dor*abs(t));

%%%Nonrephasing


%Response functions

%%%%%%%%%%%%%%%%%%%%%%%%%%%%%%%%
%%%%%%%%%%%Rephasing%%%%%%%%%%%%
%%%%%%%%%%%%%%%%%%%%%%%%%%%%%%%%

%%%%Orientational Component
t1=tau1R;
tau1=tau1R;
t3=t1R;

[j t1n]=size(t1);
[j t3n]=size(t3);

Y_2_0101=(1./9).*c1(t1).*c1(t3).*(1+(4./5).*c2(tau2));
Y_3_0101=(1./9).*c1(t1).*c1(t3).*(1+(4./5).*c2(tau2));
Y_5_0121=(1./9).*c1(t1).*c1(t3).*(1+(4./5).*c2(tau2)).*cos(thetaor).^2+(1./15).*c1(t1).*c1(t3).*c
2(tau2).*sin(thetaor).^2;


R2_0101_a=zeros(t1n,t3n,1);

for l=1:t1n;
    t1=tau1(l);
    R2_0101_a(:,l,1)=Y_2_0101.*rho00.*(mu01_a).^4.*exp(1i.*w10_a.*t1-1i.*w10_a.*t3).*exp(-
(g11(t1+tau2)+g11(-tau2-t3)+g11(t1)-g11(t3+t1+tau2)-g11(-tau2)+g11(t3))).*exp(-
(t3+t1)./(2.*Tpop_a)).*exp(-tau2./Tpop_a).*(exp(-t1./T2star_a).*exp(-t3./T2star_a));
end

R2_0101_b=zeros(t1n,t3n,1);

for l=1:t1n;
    t1=tau1(l);
    R2_0101_b(:,l,1)=Y_2_0101.*rho00.*(mu01_b).^4.*exp(1i.*w10_b.*t1-1i.*w10_b.*t3).*exp(-
```

```
(h11(t1+tau2)+h11(-tau2-t3)+h11(t1)-h11(t3+t1+tau2)-h11(-tau2)+h11(t3))).*exp(-
(t3+t1)./(2.*Tpop_b)).*exp(-tau2./Tpop_b).*(exp(-t1./T2star_b).*exp(-t3./T2star_b));
end

% figure
% contourf(R2_0101_b,10)

% w_R2=fftshift(fft2(R2_0101,2048,2048));
% w_R2=fliplr(w_R2);
%
% figure
% contourf(w1,w3,real(w_R2(w1start:w1end,w1start:w1end)),-1200:100:1200)
% axis square
% box on
% set(gca,'tickdir', 'out')
% set(gca, 'ticklength', [0.01,0.03])
% set(gca, 'fontsize', 16)
% set(gca, 'linewidth', 2)
% set(gca, 'fontname', 'arial')
% set(gca, 'fontweight', 'b')
% xlabel('\omega_1/2\pic (cm^-^1)')
% ylabel('\omega_3/2\pic (cm^-^1)')
% title('Rephasing: R_2^0^1^0^1 \tau_2=0')

R3_0101_a=zeros(t1n,t3n,1);

for l=1:t1n;
    t1=tau1(l);
    R3_0101_a(:,l,1)=Y_3_0101.*rho00.*(mu01_a).^4.*(exp(1i.*w10_a.*t1-1i.*w10_a.*t3).*exp(-
conj((g11(-t3)+g11(t1)-g11(t3+tau2+t1)+g11(t3+tau2)+g11(tau2+t1)-g11(tau2))))).*exp(-
(t3+t1)./(2.*Tpop_a)).*exp(-tau2./Tpop_a).*(exp(-t1./T2star_a).*exp(-t3./T2star_a));
end

R3_0101_b=zeros(t1n,t3n,1);

for l=1:t1n;
    t1=tau1(l);
    R3_0101_b(:,l,1)=Y_3_0101.*rho00.*(mu01_b).^4.*(exp(1i.*w10_b.*t1-1i.*w10_b.*t3).*exp(-
conj((h11(-t3)+h11(t1)-h11(t3+tau2+t1)+h11(t3+tau2)+h11(tau2+t1)-h11(tau2))))).*exp(-
(t3+t1)./(2.*Tpop_b)).*exp(-tau2./Tpop_b).*(exp(-t1./T2star_b).*exp(-t3./T2star_b));
end


% w_R3=fftshift(fft2(R3_0101,2048,2048));
% w_R3=fliplr(w_R3);
%
% figure
% contourf(w1,w3,real(w_R3(w1start:w1end,w1start:w1end)),-1200:100:1200)
% axis square
% box on
% set(gca,'tickdir', 'out')
% set(gca, 'ticklength', [0.01,0.03])
% set(gca, 'fontsize', 16)
```

```
% set(gca, 'linewidth', 2)
% set(gca, 'fontname', 'arial')
% set(gca, 'fontweight', 'b')
% xlabel('\omega_1/2\pic (cm^-^1)')
% ylabel('\omega_3/2\pic (cm^-^1)')
% title('Rephasing: R_3^0^1^0^1 \tau_2=0')


R5_0121_a=zeros(t1n,t3n,1);

for l=1:t1n;
    t1=tau1(l);

R5_0121_a(:,l,1)=Y_5_0121.*rho00.*(mu01_a).^2.*(mu12_a).^2.*(exp(+1i.*w10_a.*t1+1i.*w12_a.*t3).*e
xp(-conj(g22(t3)+g11(-tau2)+g11(t1+tau2+t3)+g12(-t3-tau2)-g12(-t3)-g12(-tau2)+g21(t1+tau2)-
g21(t1+tau2+t3)-g21(-t3)+g11(t1)-g11(-t3-tau2)-g11(t1+tau2)+g11(-t3)))).*exp(-
t3./((3./2).*Tpop_a)).*exp(-tau2./Tpop_a).*exp(-t1./(2.*Tpop_a)).*(exp(-t1./T2star_a).*exp(-
t3./(T2star_a)));
end

R5_0121_b=zeros(t1n,t3n,1);

for l=1:t1n;
    t1=tau1(l);

R5_0121_b(:,l,1)=Y_5_0121.*rho00.*(mu01_b).^2.*(mu12_b).^2.*(exp(+1i.*w10_b.*t1+1i.*w12_b.*t3).*e
xp(-conj(h22(t3)+h11(-tau2)+h11(t1+tau2+t3)+h12(-t3-tau2)-h12(-t3)-h12(-tau2)+h21(t1+tau2)-
h21(t1+tau2+t3)-h21(-t3)+h11(t1)-h11(-t3-tau2)-h11(t1+tau2)+h11(-t3)))).*exp(-
t3./((3./2).*Tpop_b)).*exp(-tau2./Tpop_b).*exp(-t1./(2.*Tpop_b)).*(exp(-t1./T2star_b).*exp(-
t3./(T2star_b)));
end

% figure
% contourf(R5_0121)

% w_R5=fftshift(fft2(R5_0121,2048,2048));
% w_R5=fliplr(w_R5);
%
% figure
% contourf(w1,w3,real(w_R5(w1start:w1end,w1start:w1end)),20)
% axis square
% box on
% set(gca,'tickdir', 'out')
% set(gca, 'ticklength', [0.01,0.03])
% set(gca, 'fontsize', 16)
% set(gca, 'linewidth', 2)
% set(gca, 'fontname', 'arial')
% set(gca, 'fontweight', 'b')
% xlabel('\omega_1/2\pic (cm^-^1)')
% ylabel('\omega_3/2\pic (cm^-^1)')
% title('Rephasing: R_5^0^1^2^1 \tau_2=0')

% matnrf1=zeros(2048,301);
```

```
% matrf1=zeros(2048,2048);

timemat_R=R2_0101_a+R3_0101_a-R5_0121_a+R2_0101_b+R3_0101_b-R5_0121_b;

matrf2=timemat_R.*triangleR;

wmat_R(:,:,h)=fliplr(fftshift(fft2(matrf2(:,:),2048,2048)));

% wmat_R=fliplr(fftshift(fft2(timemat_R,2048,2048)));

% figure
% contourf(real(wmat_R(w1start:w1end,w1start:w1end)),20)
% title('Rephasing frequeny \tau_2=0')

% figure
% contourf(tau1,tau3,timemat_R)
% axis square
% box on
% set(gca,'tickdir', 'out')
% set(gca, 'ticklength', [0.01,0.03])
% set(gca, 'fontsize', 16)
% set(gca, 'linewidth', 2)
% set(gca, 'fontname', 'arial')
% set(gca, 'fontweight', 'b')
% xlabel('\tau1_1 (fs)')
% ylabel('\tau3_3(fs)')
% title('Rephasing time domain \tau_2=0')


% figure
% contourf(w1,w3,wmat_R(w1start:w1end,w1start:w1end),20)


%%%%%%%%%%%%%%%%%%%%%%%%%%%%%%%%
%%%%%%%%%%Nonrephasing%%%%%%%%%%
%%%%%%%%%%%%%%%%%%%%%%%%%%%%%%%%

%%%Orientational Component

t1=tau1NR;
tau1=t1;
t3=t1;
[j t1n]=size(t1);
[j t3n]=size(t3);

Y_1_0101=(1./9).*c1(t1).*c1(t3).*(1+(4./5).*c2(tau2));
Y_4_0101=(1./9).*c1(t1).*c1(t3).*(1+(4./5).*c2(tau2));
Y_6_0121=(1./9).*c1(t1).*c1(t3).*(1+(4./5).*c2(tau2)).*cos(thetaor).^2+(1./9).*c1(t1).*c1(t3).*(1
-(2./5).*c2(tau2)).*sin(thetaor).^2;


NR1_0101_a=zeros(t1n,t3n,1);
```

```
for l=1:t1n;
    t1=tau1(l);
    NR1_0101_a(:,l,1)=Y_1_0101.*rho00.*abs(mu01_a).^4.*exp(-(1i.*w10_a*t1+1i.*w10_a.*t3)).*exp(-
(g11(-tau2)+g11(t1+tau2+t3)+g11(t1)-g11(-t3-tau2)-g11(t1+tau2)+g11(-t3))).*exp(-
(t3+t1)./(2.*Tpop_a)).*exp(-tau2./Tpop_a).*(exp(-t1./T2star_a).*exp(-t3./T2star_a));
end

NR1_0101_b=zeros(t1n,t3n,1);

for l=1:t1n;
    t1=tau1(l);
    NR1_0101_b(:,l,1)=Y_1_0101.*rho00.*abs(mu01_b).^4.*exp(-(1i.*w10_b*t1+1i.*w10_b.*t3)).*exp(-
(h11(-tau2)+h11(t1+tau2+t3)+h11(t1)-h11(-t3-tau2)-h11(t1+tau2)+h11(-t3))).*exp(-
(t3+t1)./(2.*Tpop_b)).*exp(-tau2./Tpop_b).*(exp(-t1./T2star_b).*exp(-t3./T2star_b));
end
%
% w_NR1=fftshift(fft2(NR1_0101,2048,2048));
%
% % figure
% % contourf(tau1,tau3,NR1_0101,10)
% % title( 'NR1')
%
% figure
% contourf(w1,w3,real(w_NR1(w1start:w1end,w1start:w1end)),20)
% axis square
% box on
% set(gca,'tickdir', 'out')
% set(gca, 'ticklength', [0.01,0.03])
% set(gca, 'fontsize', 16)
% set(gca, 'linewidth', 2)
% set(gca, 'fontname', 'arial')
% set(gca, 'fontweight', 'b')
% xlabel('\omega_1/2\pic (cm^-^1)')
% ylabel('\omega_3/2\pic (cm^-^1)')
% title('NR R_1^0^1^0^1 \tau_2=0')
% hold on
% plot(diagonalx,diagonaly,'k--','linewidth',3)

NR4_0101_a=zeros(t1n,t3n,1);
for l=1:t1n;
    t1=tau1(l);
    NR4_0101_a(:,l,1)=Y_4_0101.*rho00.*abs(mu01_a).^4.*exp(-1i.*w10_a.*t1-1i.*w10_a.*t3).*exp(-
(g11(t3)+g11(t1)+g11(t1+tau2+t3)-g11(t3+tau2)-g11(tau2+t1)+g11(tau2))).*exp(-
(t3+t1)./(2.*Tpop_a)).*exp(-tau2./Tpop_a).*(exp(-t1./T2star_a).*exp(-t3./T2star_a));
end

NR4_0101_b=zeros(t1n,t3n,1);
for l=1:t1n;
    t1=tau1(l);
    NR4_0101_b(:,l,1)=Y_4_0101.*rho00.*abs(mu01_b).^4.*exp(-1i.*w10_b.*t1-1i.*w10_b.*t3).*exp(-
(h11(t3)+h11(t1)+h11(t1+tau2+t3)-h11(t3+tau2)-h11(tau2+t1)+h11(tau2))).*exp(-
(t3+t1)./(2.*Tpop_b)).*exp(-tau2./Tpop_b).*(exp(-t1./T2star_b).*exp(-t3./T2star_b));
end
```

```
% w_NR4=fftshift(fft2(NR4_0101,2048,2048));
%
%
% figure
% contourf(w1,w3,real(w_NR4(w1start:w1end,w1start:w1end)),-1200:100:1200)
% axis square
% box on
% set(gca,'tickdir', 'out')
% set(gca, 'ticklength', [0.01,0.03])
% set(gca, 'fontsize', 16)
% set(gca, 'linewidth', 2)
% set(gca, 'fontname', 'arial')
% set(gca, 'fontweight', 'b')
% xlabel('\omega_1/2\pic (cm^-^1)')
% ylabel('\omega_3/2\pic (cm^-^1)')
% title('NR R_4^0^1^0^1 \tau_2=0')
% hold on
% plot(diagonalx,diagonaly,'k--','linewidth',3)


NR6_0121_a=zeros(t1n,t3n,1);
for l=1:t1n;
    t1=tau1(l);
    NR6_0121_a(:,l,1)=Y_6_0121.*rho00.*abs(mu01_a).^2.*abs(mu12_a).^2.*exp(-
1i.*w10_a*t1+1i.*(w12_a).*t3).*exp(-conj(g22(t3)+g11(t1+tau2)+g11(-tau2-t3)+g12(-tau2)-g12(t3)-
g12(-tau2-t3)+g21(t1+tau2+t3)-g21(t1+tau2)-g21(t3)+g11(t1)-g11(t3+t1+tau2)-g11(-
tau2)+g11(t3))).*exp(-t3./((3./2).*Tpop_a)).*exp(-tau2./Tpop_a).*exp(-t1./(2.*Tpop_a)).*(exp(-
t1./T2star_a).*exp(-t3./T2star_a));
end

NR6_0121_b=zeros(t1n,t3n,1);
for l=1:t1n;
    t1=tau1(l);
    NR6_0121_b(:,l,1)=Y_6_0121.*rho00.*abs(mu01_b).^2.*abs(mu12_b).^2.*exp(-
1i.*w10_b*t1+1i.*(w12_b).*t3).*exp(-conj(h22(t3)+h11(t1+tau2)+h11(-tau2-t3)+h12(-tau2)-h12(t3)-
h12(-tau2-t3)+h21(t1+tau2+t3)-h21(t1+tau2)-h21(t3)+h11(t1)-h11(t3+t1+tau2)-h11(-
tau2)+h11(t3))).*exp(-t3./((3./2).*Tpop_b)).*exp(-tau2./Tpop_b).*exp(-t1./(2.*Tpop_b)).*(exp(-
t1./T2star_b).*exp(-t3./T2star_b));
end



% w_NR6=fftshift(fft2(NR6_0121,2048,2048));

% figure
% contourf(w1,w3,real(w_NR6(w1start:w1end,w1start:w1end)),-1200:100:1200)
% axis square
% box on
% set(gca,'tickdir', 'out')
% set(gca, 'ticklength', [0.01,0.03])
% set(gca, 'fontsize', 16)
```

```
% set(gca, 'linewidth', 2)
% set(gca, 'fontname', 'arial')
% set(gca, 'fontweight', 'b')
% xlabel('\omega_1/2\pic (cm^-^1)')
% ylabel('\omega_3/2\pic (cm^-^1)')
% title('NR R_6^0^1^2^1 \tau_2=0')
% hold on
% plot(diagonalx,diagonaly,'k--','linewidth',3)

timemat_NR=NR1_0101_a+NR4_0101_a-NR6_0121_a+NR1_0101_b+NR4_0101_b-NR6_0121_b;

matnrf2=timemat_NR(:,:).*triangleNR;

wmat_NR(:,:,h)=fftshift(fft2(matnrf2,2048,2048));

% % wmat_R=fliplr(fftshift(fft2(timemat_R,2048,2048)));
% figure
% contourf(w1,w3,real(wmat_NR(w1start:w1end,w1start:w1end)),20)
%
% figure
% contourf(real(wmat_R(w1start:w1end,w1start:w1end)),20)
% title('Rephasing frequeny \tau_2=0')


% wmat_NR=fftshift(fft2(timemat_NR,2048,2048));

% figure
% contourf(w1,w3,real(wmat_NR(w1start:w1end,w1start:w1end)),-1200:100:1200)
% axis square
% box on
% set(gca,'tickdir', 'out')
% set(gca, 'ticklength', [0.01,0.03])
% set(gca, 'fontsize', 16)
% set(gca, 'linewidth', 2)
% set(gca, 'fontname', 'arial')
% set(gca, 'fontweight', 'b')
% xlabel('\omega_1/2\pic (cm^-^1)')
% ylabel('\omega_3/2\pic (cm^-^1)')
% title('NR frequency')
% hold on
% plot(diagonalx,diagonaly,'k--','linewidth',3)
%
%
% figure
% contourf(tau1,tau3,timemat_NR)
% axis square
% box on
% set(gca,'tickdir', 'out')
% set(gca, 'ticklength', [0.01,0.03])
% set(gca, 'fontsize', 16)
% set(gca, 'linewidth', 2)
% set(gca, 'fontname', 'arial')
% set(gca, 'fontweight', 'b')
```

```
% xlabel('\tau1_1 (fs)')
% ylabel('\tau3_3(fs)')
% title('NR time \tau_2=0')



% Matfin(:,:,k)=real(wmat_R(:,:,k)+wmat_NR(:,:,k));
% max1=max(max(Matfin(:,:,1)));
Matfin(:,:,h)=real(wmat_R(:,:,h)+wmat_NR(:,:,h));

diagonalx=1850:1950;
diagonaly=diagonalx;

figure
contourf(w1,w3,real(Matfin(w1start:w1end,w1start:w1end,h)),20);
axis square
axis([1850 1950 1850 1950])
box on
set(gca,'tickdir', 'out')
set(gca, 'ticklength', [0.03,0.01])
set(gca, 'fontsize', 16)
set(gca, 'linewidth', 3)
set(gca, 'fontname', 'arial')
set(gca, 'fontweight', 'b')
xlabel('\omega_1/2\pic (cm^-^1)')
ylabel('\omega_3/2\pic (cm^-^1)')
% title('Correlation Spectrum')
hold on
% plot(diagonalx,diagonalx,'k--','linewidth',3)
hold off
end

%
% for h=1:t21
% figure
% contourf(w1(1:78),w3(1:78),real(Matfin_exp(1:78,1:78,h)),20);
% axis square
% axis([1870 1945 1870 1945])
% box on
% set(gca,'tickdir', 'out')
% set(gca, 'ticklength', [0.03,0.01])
% set(gca, 'fontsize', 16)
% set(gca, 'linewidth', 2)
% set(gca, 'fontname', 'arial')
% set(gca, 'fontweight', 'b')
% xlabel('\omega_1/2\pic (cm^-^1)')
% ylabel('\omega_3/2\pic (cm^-^1)')
% % title('Correlation Spectrum')
% hold on
% plot(diagonalx,diagonalx,'k--','linewidth',3)
% hold off
% end
```

```
%
% for k=1:t21
% Matfin_norm(:,:,k)=Matfin(w1start:w1end,w1start:w1end,k)./max(max(Matfin(:,:,1)));
% end
%
% slice_fundamental=Matfin_norm(:,37,:);
% slice_fundamental_exp=Matfin_exp(:,37,:);
% slice_fundamental2=Matfin_norm(:,25,:);
% slice_fundamental_exp2=Matfin_exp(:,25,:);
% slice_fundamental3=Matfin_norm(:,53,:);
% slice_fundamental_exp3=Matfin_exp(:,53,:);
%
% slice_fundamental_3=Matfin_norm(37,:,:);
% slice_fundamental_exp_3=Matfin_exp(37,:,:);
% slice_fundamental2_3=Matfin_norm(25,:,:);
% slice_fundamental_exp2_3=Matfin_exp(25,:,:);
% slice_fundamental3_3=Matfin_norm(53,:,:);
% slice_fundamental_exp3_3=Matfin_exp(53,:,:);
%
%
% % %%%plot slices along w1
% for k=1:t21
% figure
% plot(w3(1:78),slice_fundamental_exp(1:78,1,k),'k','linewidth',3)
% axis([1870 1945 -1.2 1])
% box on
% set(gca,'tickdir', 'out')
% set(gca, 'ticklength', [0.03,0.01])
% set(gca, 'fontsize', 16)
% set(gca, 'linewidth', 3)
% set(gca, 'fontname', 'arial')
% set(gca, 'fontweight', 'b')
% title('plotted on /w3')
% hold on
% plot(w3(1:78),slice_fundamental(1:78,1,k),'r','linewidth',3)
% plot(w3(1:78),slice_fundamental_exp2(1:78,1,k),'k--','linewidth',3)
% plot(w3(1:78),slice_fundamental2(1:78,1,k),'r--','linewidth',3)
% plot(w3(1:78),slice_fundamental_exp3(1:78,1,k),'k-.','linewidth',3)
% plot(w3(1:78),slice_fundamental3(1:78,1,k),'r-.','linewidth',3)
% hold off
% end
% % %%%plot slices along w3
% for k=1:t21
% figure
% plot(w1(1:78),slice_fundamental_exp_3(1,1:78,k),'k','linewidth',3)
% axis([1870 1945 -1.2 1])
% box on
% set(gca,'tickdir', 'out')
% set(gca, 'ticklength', [0.03,0.01])
% set(gca, 'fontsize', 16)
% set(gca, 'linewidth', 3)
% set(gca, 'fontname', 'arial')
% set(gca, 'fontweight', 'b')
```

```
% hold on
% plot(w1(1:78),slice_fundamental_3(1,1:78,k),'r','linewidth',3)
% plot(w1(1:78),slice_fundamental_exp2_3(1,1:78,k),'k--','linewidth',3)
% plot(w1(1:78),slice_fundamental2_3(1,1:78,k),'r--','linewidth',3)
% plot(w1(1:78),slice_fundamental_exp3_3(1,1:78,k),'k-.','linewidth',3)
% plot(w1(1:78),slice_fundamental3_3(1,1:78,k),'r-.','linewidth',3)
% hold off
% end
%
%
%
% %%%Simulate FTIR
%
% load('SNP_MeOH_14_8mM_100um_4_5_11_sub.txt')
% SNP_exp=SNP_MeOH_14_8mM_100um_4_5_11_sub(1525:1610,:);
% SNP_exp(:,2)=SNP_exp(:,2)./max(SNP_exp(:,2));
%
% t1step=3;
% % c2w=2.0.*pi.*2.998.*10.^-5;
% w01=-409.02763515864.*c2w;
% % mu01=1;
% t=1:3:8000;
%
% % A1=q(1);
% % A2=q(2);
% % tc2=q(3);
% % T2star=q(4);
%
% % phi=2.089;
% % theta=92;
%
%
% for p = 1:8192;
%     newfreq(p)=p/(8192*t1step);
% end
% g=0:1:8192;
% freq1=zeros(size(g));
% freq2=newfreq(1:8192/2);
% freq2=fliplr(freq2);
% freq2=freq2.*(-1);
% freq1(1:8192/2)=freq2;
% freq1(8192/2+1)=0;
% freq1(8192/2+2:end)=newfreq(1:8192/2);
%
% w1start=round(200*8192*3*t1step/100000+8192/2+1);
% w1end=round(600*8192*3*t1step/100000+8192/2+1);
% w1=freq1(w1start:w1end)'./2.9979e-05;
% w1=w1+1500;
%
% w3=w1;
%
%
% Tor=46000;
```

```
%
%
% g = @(t) A1.*A1.*tc1.*tc1.*(exp(-abs(t)./tc1)+abs(t)./tc1-1)+A2.*A2.*tc2.*tc2.*(exp(-
abs(t)./tc2)+abs(t)./tc2-1);%
% %%cos part -1./((1+theta.^2*tc13.^2).^2).*((theta.^3.*tc13.^3.*cos(phi).*abs(t)-
theta.^2.*tc13.^3.*exp(-abs(t)./tc13).*cos(theta.*abs(t)+phi)-
cos(phi).*abs(t).*theta.^2.*tc13.^2-2.*theta.*tc13.^2.*sin(phi)+2.*theta.*tc13.^2.*exp(-
abs(t)./tc13).*sin(theta.*abs(t)+phi)+tc13.*cos(phi)-tc13.*exp(-
abs(t)./tc13).*cos(theta.*abs(t)+phi)+theta.*tc13.*sin(phi).*abs(t)-
cos(phi).*abs(t)).*tc13.*A13.^2);
%
% R1=abs(mu01).^2.*exp(-1i.*w01.*t).*exp(-g(t)).*exp(-abs(t)./T2star).*exp(-
abs(t)./(2.*Tpop)).*exp(-abs(t)./Tor);
%
% [rR cR]=size(R1);
% ar=1-((1./cR).*(1:1:cR));
% freq=fftshift(fft(R1.*ar,8192));
%
% % figure(1)
% % plot(w1,real(freq(w1start:w1end)))
%
%
% SIM_interp=interp1(w1,freq(w1start:w1end),SNP_exp(:,1));
% SIM_interp=SIM_interp./max(SIM_interp);
%
% figure
% plot(SNP_exp(:,1),SNP_exp(:,2),'k',SNP_exp(:,1),real(SIM_interp),'r','linewidth',3)
% axis square
% axis([1870 1945 0 1])
% box on
% set(gca,'YTick',[1875:20:1935])
% set(gca,'XTick',[1875:20:1935])
% set(gca,'tickdir', 'out')
% set(gca, 'ticklength', [0.03,0.01])
% set(gca, 'fontsize', 16)
% set(gca, 'linewidth', 3)
% set(gca, 'fontname', 'arial')
% set(gca, 'fontweight', 'b')
% title('FTIR')
%
% % %%%Fit the FTIR with the new parameters
% %
% % global  tc2
% % q0=[A1,A2,T2star];
% % lb=[0.00001,0.0001,1000];
% % ub=[.001,0.001,3000];
% % options=optimset('MaxFunEvals', 1000000, 'MaxIter', 1000000,'TolFun',1E-15);
% % [f, resnorm, residual,exitflag,output,lambda,jacobian]=lsqnonlin('FITFTIR',q0,lb,ub,options);
% %
% % A1=f(1);
% % A2=f(2);
% % T2star=f(3);
% %
```

```
% % h = @(t) A1.*A1.*tc1.*tc1.*(exp(-abs(t)./tc1)+abs(t)./tc1-1)+A2.*A2.*tc2.*tc2.*(exp(-
abs(t)./tc2)+abs(t)./tc2-1);%
% %
% % R1_fit=abs(mu01).^2.*exp(-1i.*w01.*t).*exp(-h(t)).*exp(-abs(t)./T2star).*exp(-
abs(t)./(2.*Tpop)).*exp(-abs(t)./Tor);
% %
% % [rR cR]=size(R1_fit);
% % ar=1-((1./cR).*(1:1:cR));
% % freq_fit=fftshift(fft(R1_fit.*ar,8192));
% %
% % % figure(1)
% % % plot(w1,real(freq(w1start:w1end)))
% %
% %
% % SIM_interp_fit=interp1(w1,freq_fit(w1start:w1end),SNP_exp(:,1));
% % SIM_interp_fit=SIM_interp_fit./max(SIM_interp_fit);
% %
% % figure
% % plot(SNP_exp(:,1),SNP_exp(:,2),'k',SNP_exp(:,1),real(SIM_interp_fit),'r','linewidth',3)
% % axis([1870 1950 0 1])
% % axis square
% % set(gca, 'Tickdir', 'out');
% % set(gca, 'FontWeight','bold')
% % set(gca,'FontSize',20)
% % set(gca, 'FontName','Arial')
% % set(gca,'TickLength', [0.03, 0.01])
% % set(gca,'LineWidth', 3)
% % title('FTIR')
%
%
%
% %%%%%% Saving it!
%
% % save Mat_fit1 Mat_fit1
% % save w1 w1
% % save w3 w3
```

Published with MATLAB® R2013a

VITA

Jennifer F. Brookes is originally from Coos Bay, Oregon where she graduated valedictorian from Marshfield High School in 2005. She went on to attend college at the University of Portland in Portland, Oregon. She graduated *cum laude* with a Bachelor of Science in Chemistry and Biology in 2009. Jennifer attended graduate school at the University of Washington in Seattle, Washington, working under the direction of Dr. Munira Khalil. She earned her Ph.D. in Chemistry in 2015.